

**EXPERIMENTAL AND THEORETICAL INVESTIGATION
OF ROUGHNESS EFFECTS
ON THIN LAMINAR FLUID FILMS**

by

Jin Hu

A thesis submitted in conformity with the requirements
for the degree of Doctor of Philosophy
Graduate Department of Mechanical and Industrial Engineering
University of Toronto



National Library
of Canada

Acquisitions and
Bibliographic Services

395 Wellington Street
Ottawa ON K1A 0N4
Canada

Bibliothèque nationale
du Canada

Acquisitions et
services bibliographiques

395, rue Wellington
Ottawa ON K1A 0N4
Canada

Your file Votre référence

Our file Notre référence

The author has granted a non-exclusive licence allowing the National Library of Canada to reproduce, loan, distribute or sell copies of this thesis in microform, paper or electronic formats.

The author retains ownership of the copyright in this thesis. Neither the thesis nor substantial extracts from it may be printed or otherwise reproduced without the author's permission.

L'auteur a accordé une licence non exclusive permettant à la Bibliothèque nationale du Canada de reproduire, prêter, distribuer ou vendre des copies de cette thèse sous la forme de microfiche/film, de reproduction sur papier ou sur format électronique.

L'auteur conserve la propriété du droit d'auteur qui protège cette thèse. Ni la thèse ni des extraits substantiels de celle-ci ne doivent être imprimés ou autrement reproduits sans son autorisation.

0-612-27957-X

Canada

Abstract

The thesis provides an insight into the complex physical phenomena of thin laminar lubricant films between rough surfaces in relative motion.

Micro-inertia effects of two-dimensional surface roughness on hydrodynamic lubrication are analyzed in the light of similitude principles involving a newly conceived reduced Reynolds number, the length parameter of surface steepness, and the classical parameter of relative roughness. Experiments described are performed in a specially designed, essentially two-dimensional, laminar-flow wind tunnel of adjustable depth. Tests on large-scale magnified reproductions of both idealized and real surface elements of bearings are carried out in the wind tunnel with the aid of hot-wire anemometry and flow visualization by the smoke-wire technique. Finite-element-method solutions of the Navier-Stokes equation for the case of an idealized rough surface, i.e., a sinusoidally wavy wall, are compared with corresponding experimental findings. Comprehensive quantitative analysis of the results leads to a proposal for the threshold of applicability of the classical Reynolds equation in the case of surface roughness. The generalization of the concept of micro-inertia to randomly rough surfaces underlines the practical utility of the work.

Acknowledgements

I wish to express my sincere gratitude to my supervisor, Professor Hans J. Leutheusser, for his constant advice, encouragement and support during my graduate study at the University of Toronto.

I greatfully acknowledge Professor Zhiming Zhang, Shanghai University, for his advisable suggestion and discussion.

I thank all technical staff at the Department of Mechanical and Industrial Engineering for helping with instrumentation and sample processing. Special thanks to Dr. Mauricio Dziedzic for helping with hot-wire anemometry calibration software and photograph development details.

I wish to thank my wife Ning Lin for creating enjoyable family life with our lovely daughter Yifan. I greatly thank my parents for their fully understanding and support for my education.

I appreciate the financial support for this work by the Natural Science and Engineering Research Council of Canada and the University of Toronto Open Fellowship.

Contents

Abstract	ii
Acknowledgements	iii
List of Figures	vi
List of Tables	xiii
List of Symbols	xv
1 Introduction	1
1.1 Fundamental concepts	1
1.2 Scope of the thesis	4
2 Methodology	7
2.1 General considerations	7
2.2 Similitude parameters	8
2.3 Experimental approach	15

2.4 Numerical approach	15
3 Method of Numerical Solution	17
3.1 Introductory remarks	17
3.2 Finite element formulation	19
3.3 Numerical calculation	24
3.4 Testing of the solution	26
4 Experimental Facilities	33
4.1 The air duct	33
4.2 Models of surface texture	38
4.2.1 Randomly rough surface	41
4.2.2 Sinusoidally wavy surface	45
4.2.3 Physically smooth surface	45
4.3 Hot-wire anemometry	46
4.4 Flow visualization	50
5 Results for Unilateral Sinusoidally Wavy Wall	52
5.1 Numerical solution obtained by FEM	52
5.2 Comprehensive quantification of findings	73
5.3 Experimental observations	82
6 Results for Unilateral Randomly Rough Wall	94

6.1	Introductory remarks	94
6.2	Experimental findings	97
6.2.1	Velocity distribution	97
6.2.2	Flow visualization	103
7	Threshold of the Smooth Boundary Condition	107
7.1	Unilateral sinusoidally wavy wall	107
7.2	Two-dimensional randomly rough wall	111
8	Conclusions	113
	Appendices	115
A	Simplifying Assumptions Used in Hydrodynamic Lubrication	115
B	Overview of Lubrication Theories of Bearing Roughness	118
C	Aspects of Surface Topography	126
D	Coefficients of Matrices in FEM	134
E	Mesh Consideration	139
F	ASME Paper No. 96-Trib-15	141
	Bibliography	147

List of Figures

1.1	Schematic diagrams of typical thrust bearing (a) Michell offset line pivot; (b) Kingsbury button point pivot (adapted from Williams, 1994)	2
1.2	(a) Cross-section of slider bearing; (b)Resulting pressure profile	3
1.3	Research loop in hydrodynamic lubrication	6
2.1	Similarity between wedge flow (a) and plane-Poiseuille flow (b)	9
2.2	Definition diagram of laminar sheet flow	11
3.1	Two-dimensional flow between a flat and a sinusoidally wavy wall	19
3.2	Mapping of global(a) and local(b) coordinates	22
3.3	(a)Definition diagram of plane Poiseuille flow; (b)Error distribution over cross-section	28
3.4	Definition diagram of laminar flow over a backward-facing step	29
3.5	Transverse velocity profiles along channel with backward-facing step, at var- ious Reynolds numbers: numerical predictions vs. experimental findings . .	30

3.6	Transverse velocity profiles along channel with backward-facing step obtained with two different meshes, at $Re = 800$	31
3.7	Streamline contours of flow over backward-facing step at $Re = 800$	32
4.1	Schematic diagram of the experimental set-up	36
4.2	Photograph of the Dayton cross-flow blower	37
4.3	Photograph of the building process of the experimental set-up: (a) duct bottom; (b) side walls; (c) levelling og the structure	39
4.4	Photographic overview of the experimental set-up	40
4.5	One segment of a tilting pad bearing	41
4.6	Schematic of three-dimensional surface measurement system	42
4.7	Surface topography of the bearing pad ($3.0\text{mm} \times 3.0\text{mm}$)	43
4.8	Surface topography of the bearing pad ($0.5\text{mm} \times 0.5\text{mm}$)	43
4.9	Master tile of the sinusoidally wavy wall	45
4.10	Photograph of probe calibration system	47
4.11	Calibration curve of P14 single wire probe	48
4.12	Calibration curve of x -component of P63 X-wire probe	49
4.13	Calibration curve of z -component of P63 X-wire probe	49
5.1	Plots of u/U for various reduced Reynolds numbers Re^* ; $\epsilon = 0.2, \gamma = 0.2$. .	54
5.2	Streamlines at various reduced Reynolds numbers Re^* ; $\epsilon = 0.2, \gamma = 0.2$. .	55
5.3	Influence of relative roughness ϵ on distribution of u/U ; $Re^* = 1.0, \gamma = 0.3$. .	57

5.4	Influence of relative roughness ϵ on streamlines; $Re^* = 1.0, \gamma = 0.3$	58
5.5	Influence of steepness γ on distribution of u/U ; $Re^* = 1.0, \epsilon = 0.2$	59
5.6	Influence of steepness γ on streamlines; $Re^* = 1.0, \epsilon = 0.2$	60
5.7	Velocity profiles at max/min channel stations, for various reduced Reynolds numbers Re^* , $\epsilon = 0.05$, and $\gamma = 0.1$	61
5.8	Velocity profiles at max/min channel stations, for various reduced Reynolds numbers Re^* , $\epsilon = 0.1$, and $\gamma = 0.1$	62
5.9	Velocity profiles at max/min channel stations, for various reduced Reynolds numbers Re^* , $\epsilon = 0.2$, and $\gamma = 0.1$	63
5.10	Velocity profiles at max/min channel stations, for various reduced Reynolds numbers Re^* , $\epsilon = 0.3$, and $\gamma = 0.1$	64
5.11	Velocity profiles at max/min channel stations, for various reduced Reynolds numbers Re^* , $\epsilon = 0.3$, and $\gamma = 0.05$	65
5.12	Velocity profiles at max/min channel stations, for various reduced Reynolds numbers Re^* , $\epsilon = 0.3$, and $\gamma = 0.2$	66
5.13	Velocity profiles at max/min channel stations, for various reduced Reynolds numbers Re^* , $\epsilon = 0.3$, and $\gamma = 0.3$	67
5.14	Local shear stress over one wavelength at various steepness (a) $\gamma = 0.05$; (b) $\gamma = 0.10$, (c) $\gamma = 0.20$, (d) $\gamma = 0.30$; for $\epsilon = 0.05$, and $Re^* = 1.0$	68
5.15	Local shear stress over one wavelength at various steepness (a) $\gamma = 0.05$; (b) $\gamma = 0.10$, (c) $\gamma = 0.20$, (d) $\gamma = 0.30$; for $\epsilon = 0.10$, and $Re^* = 1.0$	69

5.16 Local shear stress over one wavelength at various steepness (a) $\gamma = 0.05$; (b) $\gamma = 0.10$, (c) $\gamma = 0.20$, (d) $\gamma = 0.30$; for $\epsilon = 0.20$, and $Re^* = 1.0$	70
5.17 Local shear stress over one wavelength at various steepness (a) $\gamma = 0.05$; (b) $\gamma = 0.10$, (c) $\gamma = 0.20$, (d) $\gamma = 0.30$; for $\epsilon = 0.30$, and $Re^* = 1.0$	71
5.18 Local shear stress over one wavelength at various reduced Reynolds number (a) $Re^* = 0.1$; (b) $Re^* = 0.5$, (c) $Re^* = 1.0$, for $\epsilon = 0.1$, and $\gamma = 0.1$	72
5.19 Fully developed flow in duct of constant cross section	73
5.20 Fully developed flow in a rectangular duct between a flat wall and a sinusoidally wavy wall over one wave length	74
5.21 Friction coefficient f^* vs. Reynolds number Re as a function of relative roughness ϵ , with steepness γ as parameter	78
5.22 Friction coefficient f^* vs. Reynolds number Re as a function of relative roughness ϵ , with steepness γ as parameter	79
5.23 Friction coefficient f^* vs. Reynolds number Re ; relative roughness $\epsilon = 0.12$ and steepness $\gamma = 0.012$	80
5.24 Friction coefficient f^* vs. reduced Reynolds number Re^* ; relative roughness $\epsilon = 0.12$ and steepness $\gamma = 0.012$	80
5.25 Evolution of streakline picture at position $x = \lambda$ of sinusoidally wavy wall; $Re^* = 1.07$, $\epsilon = 0.15$, and $\gamma = 0.012$	85
5.26 Streakline pictures at various streamlinewise positions of sinusoidally wavy wall; $Re^* = 1.07$, $\epsilon = 0.2$, $\lambda = 0.012$	86

5.27 Overall comparison of velocity vector plots between experimental measurement and numerical results for sinusoidally wavy wall; $Re^* = 1.07$, $\epsilon = 0.2$, $\gamma = 0.012$	87
5.28 Comparison of velocity profile u/U between experimental measurement and numerical results for sinusoidally wavy wall; $Re^* = 0.49$, $\epsilon = 0.20$, $\gamma = 0.012$	88
5.29 Comparison of velocity profile u/U between experimental measurement and numerical results for sinusoidally wavy wall; $Re^* = 1.00$, $\epsilon = 0.20$, $\gamma = 0.012$	89
5.30 Comparison of velocity profile u/U between experimental measurement and numerical results for sinusoidally wavy wall; $Re^* = 1.00$, $\epsilon = 0.15$, $\gamma = 0.012$	90
5.31 Comparison of velocity profile u/U between experimental measurement and numerical results for sinusoidally wavy wall; $Re^* = 0.90$, $\epsilon = 0.30$, $\gamma = 0.012$	91
5.32 Streamlines along sinusoidal wall for varying relative roughness ϵ , $\gamma = 0.012$	92
5.33 Streamlines along sinusoidal wall at various positions, for $\gamma = 0.012$	93
6.1 Surface profile chosen as testing sample	96
6.2 Photograph of the two kinds of randomly rough testing tiles	97
6.3 Velocity vector plots and streamlines for part of surface RanTes1, by hot-wire anemometry, $Re^* = 0.349$, $\epsilon = 0.049$ ($h_0 = 15\text{mm}$), $\gamma = 0.014$	99
6.4 Velocity vector plots and streamlines for part of surface RanTes1, by hot-wire anemometry, $Re^* = 0.349$, $\epsilon = 0.073$ ($h_0 = 10 \text{ mm}$), $\gamma = 0.014$	100

6.5 Velocity vector plots and streamlines for part of surface RanTes2, by hot-wire anemometry, $Re^* = 0.349$, $\epsilon = 0.052$ ($h_0 = 15$ mm), $\gamma = 0.015$	101
6.6 Velocity vector plots and streamlines for part of surface RanTes2, by hot-wire anemometry, $Re^* = 0.349$, $\epsilon = 0.078$ ($h_0 = 10$ mm), $\gamma = 0.015$	102
6.7 Streamlines for various values of relative roughness, $\gamma = 0.014$	104
6.8 Streamlines for various values of reduced Reynolds number Re^*	105
6.9 Temporal flow streaklines for RanTes1 at $Re^* = 0.273$, $\epsilon = 0.049$ ($h_0 = 15$ mm), $\gamma = 0.014$	106
7.1 Variation of sensitivity parameter χ with relative roughness ϵ for two values of Re^* ; $\gamma = 0.1$	109
7.2 Variation of sensitivity parameter χ with relative roughness ϵ for two values of Re^* ; $\gamma = 0.012$	109
7.3 Variation of sensitivity parameter χ with steepness γ for two values of Re^* ; $\epsilon = 0.3$	110
7.4 Variation of sensitivity parameter χ with reduced Reynolds number Re^* ; $\epsilon = 0.12$, $\gamma = 0.012$	110
7.5 Envelope of equal sensitivity parameter $\chi = 10\%$	112
A.1 Clarifying diagram	116
B.1 Definition diagrams of two-dimensional roughness	119
B.2 Slider bearing with roughness on static surface	120

B.3 Coordinate transformation for inclined striated roughness	123
C.1 Geometric components of a surface	127
C.2 Surface profile: (a)The profile of a real surface greatly magnified; (b) the profile of the surface with a 5-times larger vertical magnification than a horizontal one; (c) as (b), but with ratio of 50:1 (From Dabhall, 1980) . . .	128
C.3 Geometrical representation of R_a and λ_a of a surface profile	129

List of Tables

A.1 Assumptions made in the derivation of the Reynolds equation	117
B.1 Comparison of the effects of surface roughness	123
E.1 Mesh consideration	140

List of Symbols

A	= area;
A_c	= hot-wire probe calibration constant;
$A(\beta_l)$	= autocorelation function;
B	= width of slider bearing;
B_c	= hot-wire probe calibration constant;
E	= voltage applied on hot-wire bridge;
F_r	= friction resistance force;
f	= Darcy-Weisbach friction factor;
f^*	= friction coefficient;
H	= channel height of plane Poiseuille flow, or flow over a backward-facing step;
$h(x)$	= film thickness in x -direction of plane slider bearing;
$h(x, y)$	= film thickness in x/y -plane of finite width slider bearing;
h_0	= nominal film thickness;
h_T	= local film thickness;
h_δ	= roughness deviating from the nominal centerline of a rough surface;
L	= length of slider bearing;
ΔL	= length of channel element;
L_d	= development length of plane Poiseuille flow;
M	= nodes of pressure used in FEM;

m	= integer number used in FEM;
N	= nodes of velocity used in FEM;
n	= integer numbers used in FEM;
n_c	= index coefficient of curve fitting in hot-wire probe calibration;
$P(\omega)$	= power spectrum;
p	= pressure;
q	= flow rate;
Δp	= pressure drop;
p_c	= centroidal pressure of element;
R_a	= average height of roughness;
R_w	= hot resistance of hot-wire probe;
R_g	= cold resistance of hot-wire probe;
Re	= bulk Reynolds number, $2Uh_0/\nu$;
Re^*	= reduced (micro-inertial) Reynolds number, $UR_a^2/(\nu\lambda_a)$, or $U\delta^2/(\nu\lambda)$;
Re^{**}	= conventional reduced (macroscopic) Reynolds number, $Uh_0^2/(\nu\Delta L)$;
$S_{2\pi}$	= surface area over length 2π ;
U	= average velocity over flow cross-section;
U_{eff}	= effective voltage applied to hot-wire;
u, w	= velocity components in x and z directions, respectively;
W	= load sustained by bearing;

x, y, z	= length coordinates;
$z(x)$	= vertical displacement of surface;
α_s	= wavy surface integration coefficient;
β	= pressure penalty parameter;
β_l	= length shift parameter;
γ	= steepness of roughness, R_a/λ_a , or δ/λ ;
Δ_a	= average slope of a profile;
δ	= amplitude of sinusoidal wave;
ϵ	= relative roughness, R_a/h_0 or δ/h_0 ;
λ	= length of sinusoidal wave;
λ_a	= average wavelength of arbitrary roughness;
μ	= dynamic viscosity;
ν	= kinematic viscosity;
ξ, η	= local coordinate;
ρ	= fluid density;
σ	= combined standard deviation of two surfaces, $\sigma = \sqrt{\sigma_1^2 + \sigma_2^2}$;
τ_w	= wall shear stress;
ϕ_i	= shape function of velocity ($i=1,2,\dots,9$);
ϕ_s	= shear flow factor;
ϕ_x	= pressure flow factor in x direction;

- ϕ_y = pressure flow factor in y direction;
 χ = sensitivity parameter;
 ψ_i = shape function of pressure ($i=1,2,3$);
 Ω_e = elemental volume;
 ω = frequency.

Matrices:

$[D]$ = pressure mass matrix;

$[L]$ = pressure matrix;

$[N]$ = convective matrix;

$[S]$ = viscous matrix.

$\bar{\cdot}$ = average quantity;

$\hat{\cdot}$ = non-centroidal nodes.

Chapter 1

Introduction

1.1 Fundamental concepts

This thesis deals with aspects of tribology and, hence, it may be appropriate to commence by providing a brief, although necessary incomplete overview of the subject.

The term *tribology*¹ was coined in 1966; it defines “the science and technology of interacting surfaces in relative motion and the practices related thereto” (Dowson, 1979). Tribology may be considered as a triangle made up of the three interacting components of *friction*, *lubrication*, and *wear* : lubrication is the key to reducing friction and wear, and thereby increases machinery efficiency and product life.

When two surfaces are in physical contact and forced to move relative to each other, resistance to the motion is generated by, mainly, adhesive processes. This frictional resis-

¹From the Greek word *τριβοσ* (tribos) = rubbing.

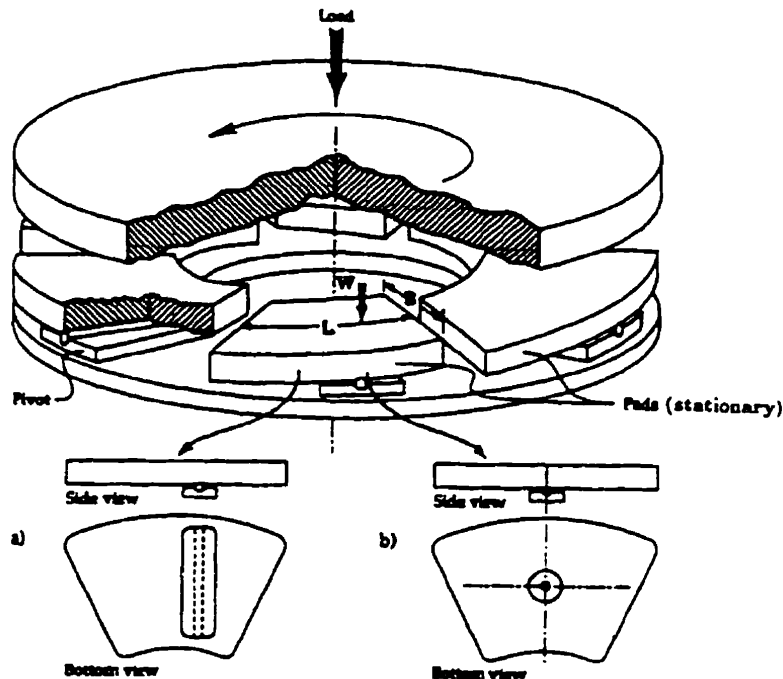


Figure 1.1: Schematic diagrams of typical thrust bearing (a) Michell offset line pivot; (b) Kingsbury button point pivot (adapted from Williams, 1994)

tance, described by the empirical laws of da Vinci, Amontons and Coulomb (Szeri, 1980), and the attendant surface damage by wear may be attenuated by interposing a shear layer of lubricant between the surfaces in relative motion. Wear will be eliminated if the layer is thick enough to separate the surfaces completely. If, in addition, the lubricant is a fluid, one speaks of fluid film lubrication which is extensively used in bearings. These are machine elements for the transmission of forces between surfaces in relative motion. An example is shown in Fig. 1.1.

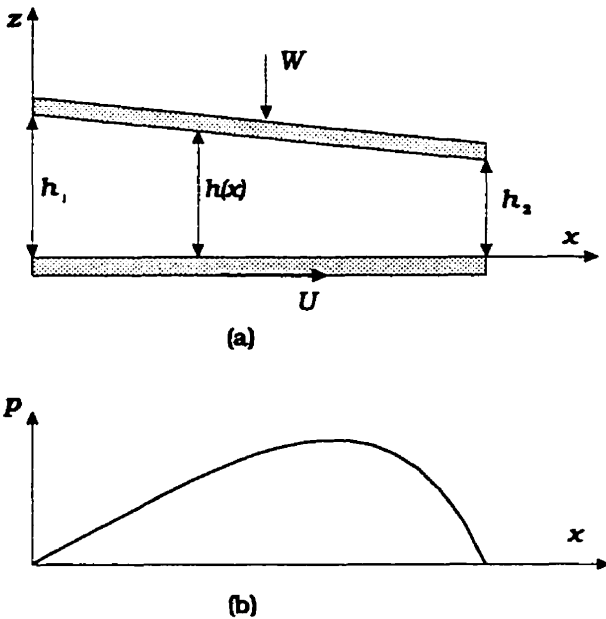


Figure 1.2: (a) Cross-section of slider bearing; (b) Resulting pressure profile

Very slow moving bearings (and bearings with parallel surfaces) require external pressurization in order to support a load and, hence, are referred to as hydrostatic. In the case of self-acting bearings, on the other hand, the load-carrying capacity is generated by the hydrodynamic miracle of the fluid wedge, i.e., a very slight convergence of the surfaces in direction of the induced lubricant flow, see Fig. 1.2, where h_1 and h_2 are the film thicknesses at the two ends of a typical slider bearing in the x/z -plane, U is the relative velocity in x -direction between the two surfaces in shearing motion, $p(x)$ is the thereby generated pressure between the surfaces, and, $W = \int_1^2 p dx$ is the load sustained by the bearing.

Mainly because of the extreme thinness of the lubricant layers, typically in the order of tenths of mm, the fluid motion therein is generally laminar and this is also assumed to hold true throughout the present work. However, turbulence may develop in fast running

bearings.

Another consequence of the thinness of the lubricant layer may be that the fluid ceases to act as a continuum (Gross, 1980). This possibility exists, usually, only for very high speed gas bearings with very thin films (in the order of tenths of μm , or smaller in thickness) and will not be considered further herein.

1.2 Scope of the thesis

The principal concern of this thesis are the effects of roughness of surfaces in relative motion on hydrodynamic lubrication under conditions of laminar flow.

The theory of hydrodynamic lubrication is based on the Navier-Stokes and the continuity equations. The relatively simple form of its working equation, the so-called Reynolds equation, for, e.g., the case of Fig. 1.2 (where $h = h(x)$ = film thickness, and μ = dynamic viscosity of the lubricant), viz.

$$\frac{d}{dx}(h^3 \frac{dp}{dx}) = 6\mu U \frac{dh}{dx} \quad (1.1)$$

is a consequence of certain simplifying assumptions (see Appendix A), making it possible to describe the pressure distribution throughout the flow field of the lubricant. This theory was initially formulated by Osborne Reynolds in 1886 (Dowson, 1979) for bearings, but, by now, has been adapted to suit practically all lubricating situations, including shaft seals and anatomical interfaces.

The boundary conditions of the Reynolds equation do not allow for possible roughness of the surfaces in relative motions. This is generally a reasonable assumption. However, when the thickness of a lubricating film is sufficiently reduced, as realized in heavily loaded bearings, and in magnetic head/disk storage devices, the size of the surface roughness may become significant compared with the film thickness (see, e.g., Best et al., 1988; Crone et al., 1991). and “micro-inertial” effects due to flow distortion by the surface texture may render the Reynolds equation invalid.

In the modern technical literature there are available essentially three theoretical approaches that have been developed for dealing with the roughness problem in bearings by modifying the classical Reynolds equation (Christensen, 1969/70; Patir and Cheng, 1978; Elrod, 1979), as discussed in Appendix B. At the same time, there exists only very limited (and doubtful) experimental support for these theories, and, indeed, an almost complete lack of detailed quantitative observations in rough non-deformable bearing flow (as opposed to elastohydrodynamic lubrication (EHL), e.g., de Silva et al., 1985).

It is the principal objective of the present work to establish the threshold of applicability of the classical Reynolds equation, and to provide a solid basis for the eventual development of a Reynolds-type equation in which proper allowance is made for the micro-inertial effects of the tortuous laminar flow about the surface roughness elements. To this end, a novel experimental approach, featuring greatly enlarged models of actual and idealized bearing elements, is combined with the predictions of a numerical solution of the Navier-Stokes equation, and the findings are analyzed in the light of a newly conceived set of similitude

parameters.

In order to facilitate the drawing of analytical deduction, much of the work is focused on the case of a sinusoidally wavy wall texture. This particular “roughness”, it is felt, conveniently joins mathematical simplicity with an, albeit crude, resemblance to a real surface. It, thus, offers an attractive environment for this fundamental inquiry.

The philosophy underlying the present work is portrayed by the block diagram of Fig. 1.3, (Pinkus, 1986). It is the Box 1 which determines the soundness of a model of hydrodynamic lubrication.

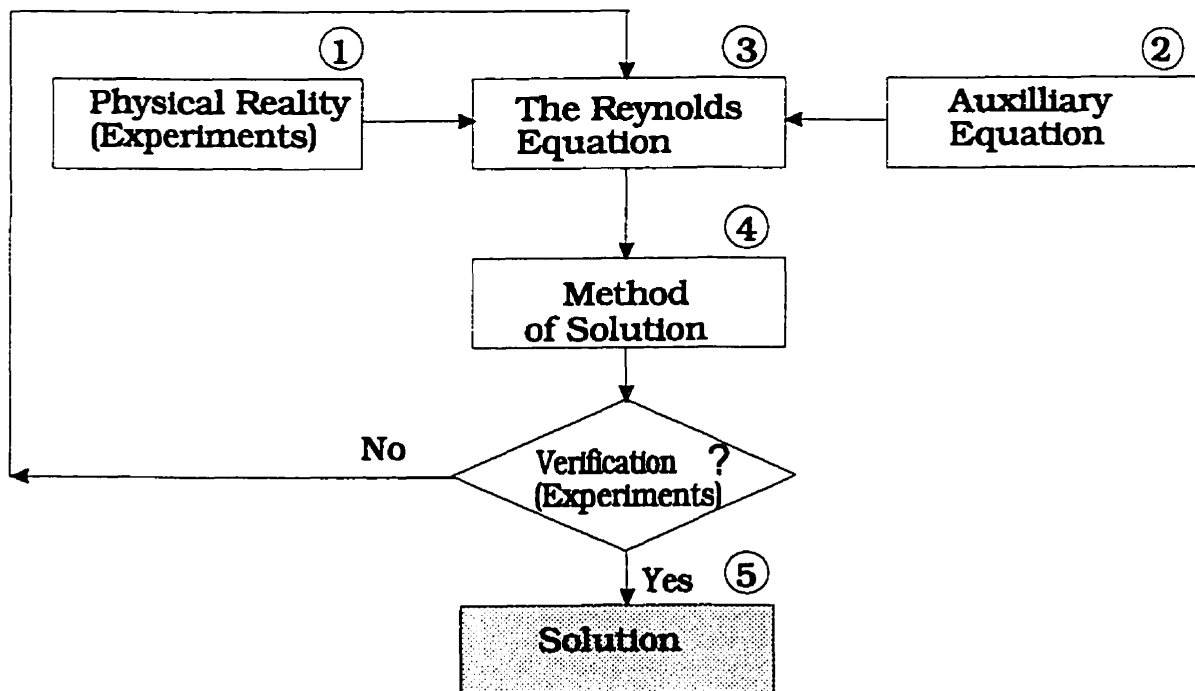


Figure 1.3: Research loop in hydrodynamic lubrication

Chapter 2

Methodology

2.1 General considerations

The fundamental difficulty of fluid film tribology rests in the extreme thinness of the sheared lubricant layer. This makes it virtually impossible to gain a direct insight into the laminar flow processes taking place between the two surfaces in relative motion, and the consequences of surface roughness can usually only be inferred from numerical solutions of appropriate analytical models, e.g., Serbetci and Tichy (1991); White et al. (1986); and Patel et al. (1991). However, even for laminar fluid motions without spatial constraints, such as boundary layers and flows in conduits, there exists a void of experimental information on the effects of boundary texture, and no guidance may be educed from these sources. It follows that an attempt to modify the classical Reynolds equation to reflect surface conditions on the basis of physical evidence will have to follow new directions. In

in the present case, the path chosen involves the use of an approximately 1000-times enlarged model of a bearing element.

In reality, most bearings extend in three dimensions. Therefore, a true experimental replica would have to be excessively large to exhibit visible surface roughness and to make flow quantities measurable. Even a two-dimensional model with one moving boundary would still pose considerable experimental difficulties (see Fig. 2.1(a)). Consequently it was decided to restrict the present inquiry to a two-dimensional, unilaterally rough plane-Poiseuille flow situation (Fig. 2.1(b) where U = average velocity over cross section, h_0 = nominal film thickness). This fluid motion is closely related to bearing flow, especially in hydrostatic bearings, and is considered adequate to provide the sought information on roughness effects in laminar sheet flow.

2.2 Similitude parameters

A thin-film channel flow between two smooth surfaces is schematically depicted in Fig. 2.2(a) where U is the average velocity in streamwise direction. The film thickness, h , is significantly smaller than the longitudinal dimension, ΔL , say $O(10^{-3})$. Under bearing conditions, i.e., with the two surfaces forming a load-sustaining fluid wedge, this feature permits to drop the (macroscopic) inertia terms in the Navier-Stokes equation and, hence, leads to the establishment of the classical Reynolds equation.

However, with decreasing film thickness, the magnitude of any surface roughness be-

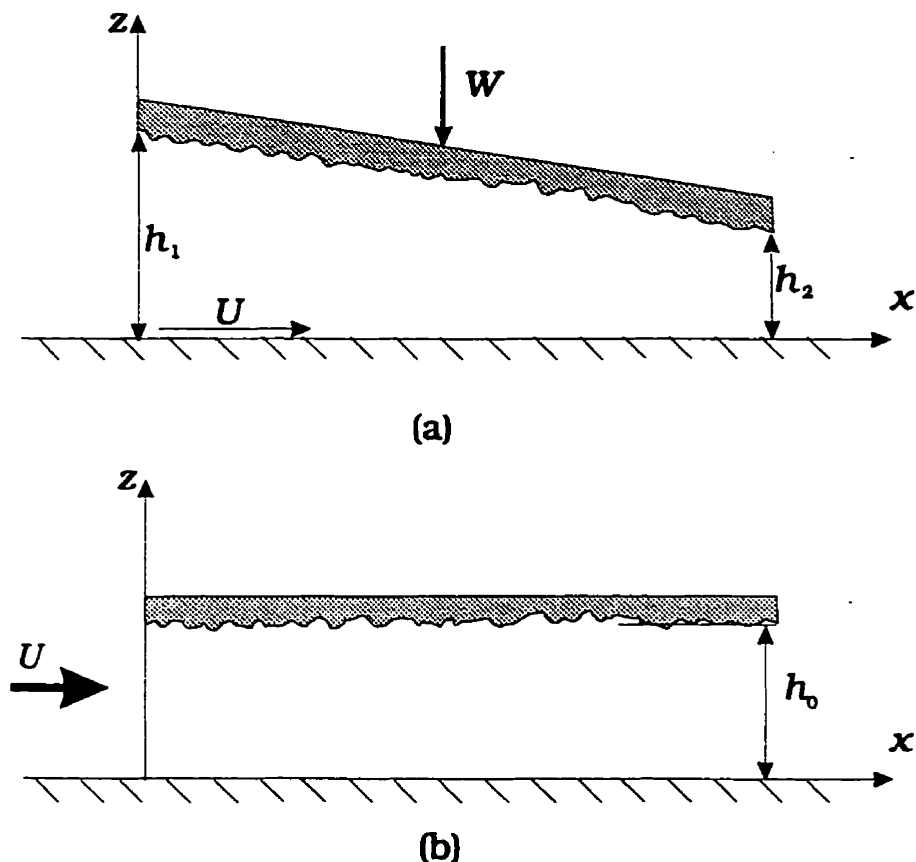


Figure 2.1: Similarity between wedge flow (a) and plane-Poiseuille flow (b)

comes closer to that of the film thickness, and the assumption of a physically smooth surface does not hold true any longer. Therefore, the real flow situation may be represented more closely by Fig. 2.2(b) where some arbitrary, albeit two-dimensional roughness is described by the parameters of average height R_a and average wavelength λ_a (see Appendix C). The corresponding length parameters for the global flow are now h_0 , the nominal film thickness, and ΔL , a characteristic length in streamwise direction.

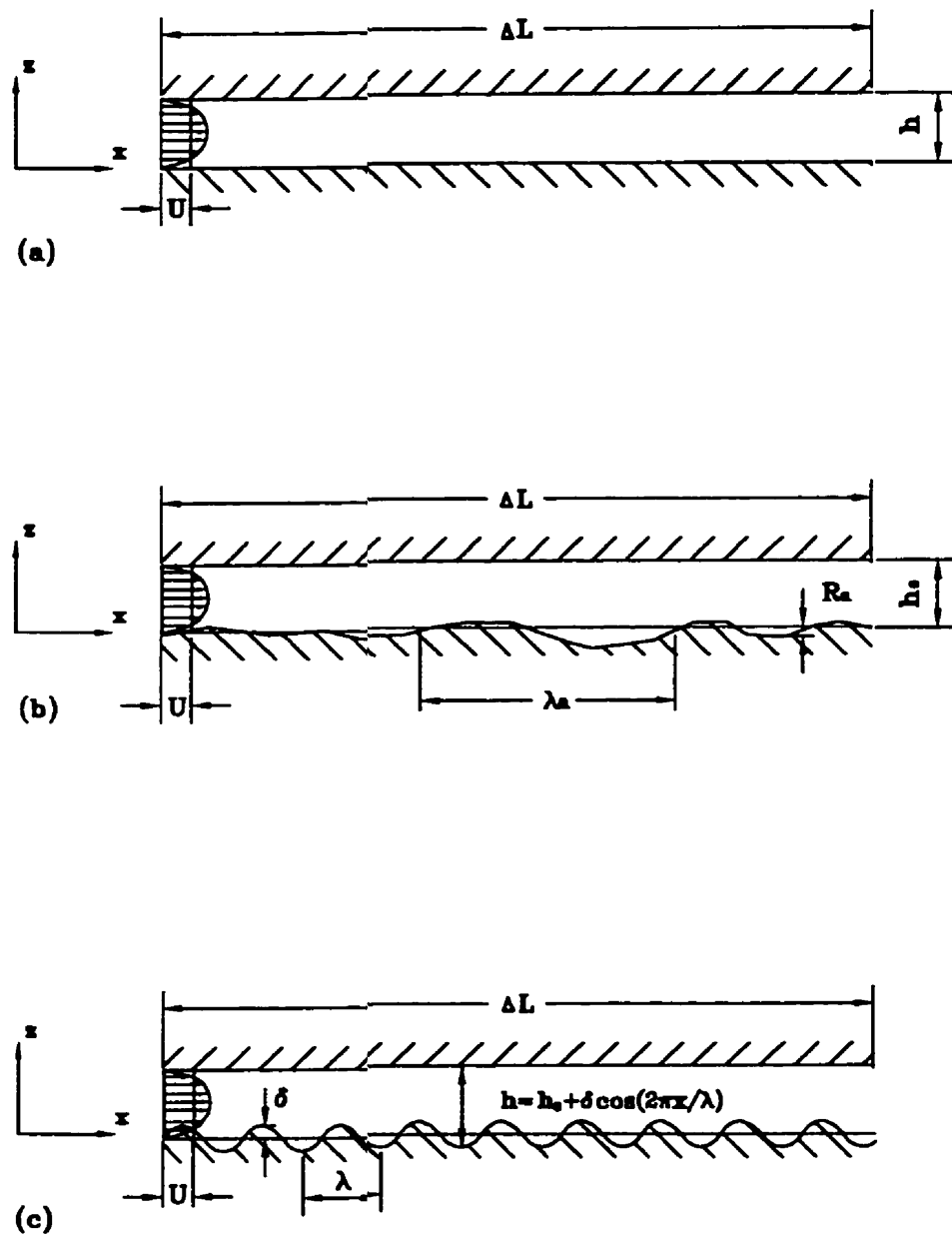


Figure 2.2: Definition diagram of laminar sheet flow

The governing equations for steady, laminar, incompressible, and isothermal Newtonian fluid flow in the x/z -plane are the continuity equation

$$\frac{\partial u}{\partial x} + \frac{\partial w}{\partial z} = 0 \quad (2.1)$$

and, neglecting body forces, the two components of the Navier-Stokes (N-S), or momentum equation

$$u \frac{\partial u}{\partial x} + w \frac{\partial u}{\partial z} = -\frac{1}{\rho} \frac{\partial p}{\partial x} + \nu \frac{\partial^2 u}{\partial x^2} + \nu \frac{\partial^2 u}{\partial z^2} \quad (2.2)$$

$$u \frac{\partial w}{\partial x} + w \frac{\partial w}{\partial z} = -\frac{1}{\rho} \frac{\partial p}{\partial z} + \nu \frac{\partial^2 w}{\partial x^2} + \nu \frac{\partial^2 w}{\partial z^2} \quad (2.3)$$

where, $\nu = \mu/\rho$ = kinematic viscosity of lubricant, ρ = density of lubricant, and u and w = velocity components in x and z directions, respectively.

For the situation depicted in Fig. 2.2(c) there are two significant length scales, i.e., the average wavelength of the roughness, λ_a , in the streamwise direction, and the average height of the roughness, R_a , in transverse direction (with R_a generally much smaller than λ_a). The corresponding velocity scales in the x and z directions are U and $R_a/\lambda_a U$, respectively.

In terms of nondimensional variables, viz. x/λ_a , z/R_a , u/U , $w/(UR_a/\lambda_a)$, $p/\rho U^2$, Eqs.(2.2) and (2.3), become:

$$Re^* \left(u \frac{\partial u}{\partial x} + w \frac{\partial u}{\partial z} + \frac{\partial p}{\partial x} \right) = \frac{R_a^2}{\lambda_a^2} \frac{\partial^2 u}{\partial x^2} + \frac{\partial^2 u}{\partial z^2} \quad (2.4)$$

$$Re^* \left(u \frac{\partial w}{\partial x} + w \frac{\partial w}{\partial z} + \frac{\lambda_a^2}{R_a^2} \frac{\partial p}{\partial z} \right) = \frac{R_a^2}{\lambda_a^2} \frac{\partial^2 w}{\partial x^2} + \frac{\partial^2 w}{\partial z^2} \quad (2.5)$$

where all terms are now understood to be nondimensional. The parameter

$$Re^* = UR_a^2/(\nu \lambda_a) \quad (2.6)$$

in these equations may be called the reduced (micro-inertial) Reynolds number. It represents the ratio of micro-inertial forces due to roughness to viscous forces, and is the appropriate scaling parameter for assuring dynamic similarity between comparable physical situations.

If, in lieu of R_a , the nominal film thickness h_0 were chosen as the transverse scaling unit (ΔL should then be used for the streamwise direction) the conventional reduced (macroscopic) Reynolds number would be

$$Re^{**} = Uh_0^2/(\nu \Delta L) . \quad (2.7)$$

The two reduced Reynolds numbers, viz. Eqs. (2.6) and (2.7), measure inertia forces in different regions of the flow. The conventional definition, i.e. Re^{**} , corresponds to the whole, macroscopic flow field, while Re^* refers to the micro-inertial effects of the asperities. The latter is the principal concern of the present research.

In addition, of course, there can always be defined an overall, or bulk Reynolds number

$$Re = \frac{2Uh_0}{\nu} \quad (2.8)$$

which determines the state, i.e., laminar or turbulent, of the flow. In Eq. (2.8), $2h_0$ is the equivalent diameter of a wide rectangular channel, and the flow is laminar (i.e., plane-Poiseuille flow) when Re is less than about 2000.

Besides the dynamic similitude parameter of the reduced Reynolds number Re^* suggested by the governing equations, dimensional analysis of the essential physical parameters involved in the problem, viz u , ρ , μ , R_a , λ_a , h_0 , show that there are also two geometric similitude parameters to be considered.

Based on experience, one of these is defined as the "relative roughness", viz.

$$\epsilon = \frac{R_a}{h_0} \quad (2.9)$$

It relates the size of the roughness to the extent of the flow field.

The other geometric similitude parameter relates the two characteristic lengths of the two-dimensional roughness and will be termed its "steepness", i.e.,

$$\gamma = \frac{R_a}{\lambda_a} \quad (2.10)$$

2.3 Experimental approach

The experiments were performed in an essentially two-dimensional variable speed air duct, of adjustable depth, 50 cm width, and 4 meter length [Hu, Leutheusser & Zhang (1994); Hu & Leutheusser (1995)]. Various interchangeable surface textures, including physically smooth, sinusoidally wavy, and randomly rough, can be installed on the bottom of the duct.

Because of the low velocities encountered in laminar air flow, all rate measurements were carried out by hot-wire anemometry using both single and x-wire probes. Flow visualization was realized by a smoke-wire technique employing a high energy pulse generator to heat an oil-covered nickel-chromium wire. The observations of the pulsed smoke plume were recorded by video cinematography and still photography.

2.4 Numerical approach

In order to analyze and extrapolate the experimental results, an analytical or numerical solution is desirable. To this end, a numerical solution by the finite element method (FEM) was developed for the case of a unilateral sinusoidally wavy boundary. The governing equations were solved using the Newton-Raphson method and employing the Crouzeix-Raviart element. The grid mesh of the fluid field was generated by a specially written code. All source codes were written in FORTRAN by the author except for the algebra system solver. The program was run on the Sparc station system of the department.

The description of the above analysis has been summarized in Hu and Leutheusser (1997a, 1997b), the later one (Hu and Leutheusser, 1997b) is included in Appendix F.

Chapter 3

Method of Numerical Solution

3.1 Introductory remarks

The governing equations of steady, laminar, incompressible and isothermal Newtonian fluid flow in the x/z -plane, viz. Eqs. (2.1)-(2.3), hold true for any texture of the physical flow boundaries. However, trying to solve these equations for randomly rough surfaces is not a realistic proposition. Nevertheless, there exist some simplified methods for solving these equations for a few macroscopic geometries. Thus, Serbetci and Tichy (1991) developed an analytical solution for two-dimensional, incompressible film flow between a sinusoidal grooved surface and a flat surface employing perturbation expansions; Ralph (1987) used the finite difference method for solving a vorticity transport equation, and a Poisson equation for finding the stream function in the case of axisymmetric flows through tubes with sinusoidal walls; finally, Patel et al. (1991) solved the Navier-Stokes equation in primitive

variables for flow in a duct with wavy walls, using a modified version of the SIMPLER algorithm.

Since the finite element method (FEM) is able to handle irregular boundary domains and nonuniform meshes with ease, it was added to the tools for the solution to the N-S equation by Oden in 1970 (Gartling and Nickell, 1977). Since that time, there has been a rapid increase in the related literature, reflecting the growing speed and memory of digital computers.

There are, generally, two categories of approaches for solving the N-S equation for the kind of flow under consideration herein, i.e., the primitive velocity-pressure approach, and the stream function-vorticity approach. Based on past research in this field, it appears that the primitive-variable formulation is preferable in terms of order of differentiation, and the treatment of boundary conditions.

Major difficulties of primitive-variable formulation in the FEM are the incompressibility constraint, and the lack of boundary conditions. These difficulties can be overcome, however, by introducing the pressure penalty method, which leads to the uncoupling of the momentum and continuity equations [Peyret and Taylor (1983); Reddy and Gartling (1994)].

In the present study, the primitive-variable formulation together with the pressure-penalty function method were used to solve the N-S equation for steady laminar flow of an incompressible Newtonian fluid in a two-dimensional channel between a flat and a sinusoidally wavy wall, see Fig. 3.1. The FEM formulation of the governing equations,

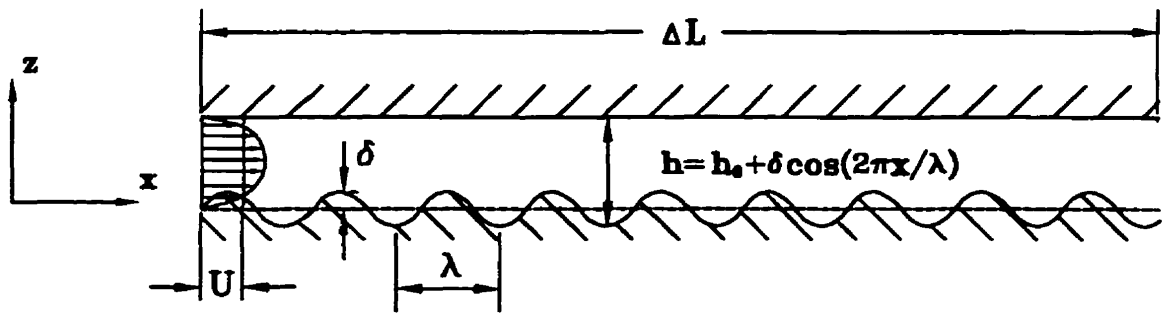


Figure 3.1: Two-dimensional flow between a flat and a sinusoidally wavy wall

the choice of element type, and the numerical method for solving the system of non-linear algebra equation are discussed in the following sections.

3.2 Finite element formulation

To generate the FEM formulation of a problem, an appropriate method must be used to relate the numerical solution of the N-S equation to the variational formulation, or its approximate form. It has been shown that the Galerkin method can be successfully applied to solve problems governed by the Navier-Stokes equation.

The following three steps are applied to get the FEM formulation of the equations:

- (1) multiply the governing equations (Eqs.(2.4)–(2.6)) by appropriate weight function to develop the corresponding weak forms;
- (2) choose an approximate form of the primitive variables; in practice, the expansions

of unknowns u , w , p , viz.

$$\begin{aligned} u &= \sum_{i=1}^N u_i \phi_i(x, z) \\ w &= \sum_{i=1}^N w_i \phi_i(x, z) \\ p &= \sum_{i=1}^{N_p} p_i \psi_i(x, z) \end{aligned} \quad (3.1)$$

where the functions $\phi_i(x, z)$ and $\psi_i(x, z)$ are called the shape (basis) functions; N and N_p are the numbers of total nodes for velocity and pressure, respectively; insert the expansions into the weak forms of the governing equations;

(3) use the proper interpolation function; in particular, let the weight function equal the shape function; this completes the Galerkin method.

For simplicity, only the major steps of the development of the FEM will be given here; details are available in the relevant literature, e.g., Cuvelier et al. (1986). Through the manipulations described in the preceding paragraphs, the matrix form of the momentum equations (Eqs. (2.5)–(2.6)) becomes:

$$[N]\{v\} + [S]\{v\} + [L]\{p\} = \{B_c\} \quad (3.2)$$

where

$$[N] = \begin{bmatrix} [N_{uu}] & [N_{uw}] \\ [N_{wu}] & [N_{ww}] \end{bmatrix} \quad (3.3)$$

$$[S] = \begin{bmatrix} [S_{uu}] & 0 \\ 0 & [S_{ww}] \end{bmatrix} \quad (3.4)$$

$$[L] = \begin{bmatrix} [L_u] & [L_w] \end{bmatrix} \quad (3.5)$$

$$\{p\} = \{p_1 \ p_2 \ \dots \ p_{N_p}\}^T \quad (3.6)$$

$$\{v\} = \{u_1 \ u_2 \ \dots \ u_N \ w_1 \ w_2 \ \dots \ w_N\}^T \quad (3.7)$$

and $\{B_c\}$ = boundary condition terms. $\frac{1}{R_e}$ is included in $[S]$, $\frac{R_a^2}{\lambda_a^2}$ is included in $[S_{uu}]$ and $[S_{wu}]$, and $\frac{\lambda_a^2}{R_a^2}$ is absorbed into $[L_w]^T$. All coefficients of above matrices are given in Appendix B.

The continuity equation Eq. (2.4) has the form:

$$[L]\{v\} = \{0\}. \quad (3.8)$$

By introducing the penalty function into Eq. (3.8), the pressure can be removed from Eq. (3.2) in terms of

$$\{p\} = \frac{1}{\beta}[D]^{-1} [L] \{v\} \quad (3.9)$$

where $[D]$ is the so-called *pressure mass matrix*, β is a small parameter usually less than

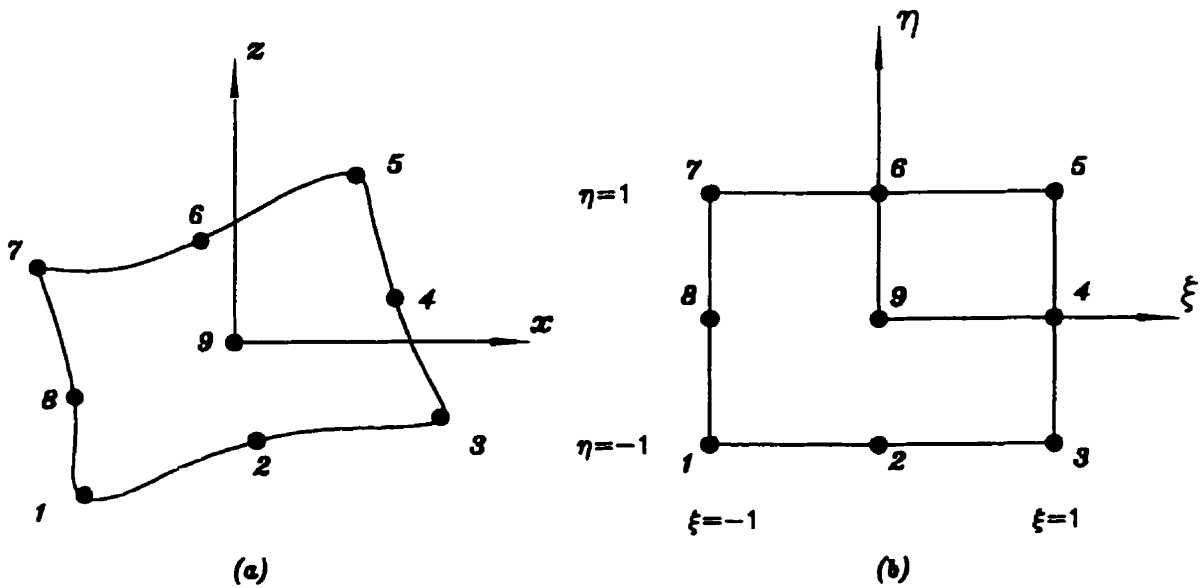


Figure 3.2: Mapping of global(a) and local(b) coordinates

10^{-6} . Therefore, Eq. (3.2) becomes:

$$[N]\{v\} + [S]\{v\} + \frac{1}{\beta} [L]^T [D]^{-1} [L]\{v\} = \{B_c\}. \quad (3.10)$$

All computations involving Eq. (3.2) referred to in the following were executed with the Crouzeix-Raviart element (Cuvelier et al., 1986) which is known to comply very well with the penalty function. This finite element is of nine-node rectangular shape and allows biquadratic interpolation of the velocity components while the pressure approximation is linear. This observation is suggested by the experience of other researchers with FEM applications to flows of the kind considered herein. Due to the linear form of the pressure approximation, the matrix $[D]$ is diagonal, which, of course, simplifies its inversion.

Since a sinusoidally wavy flow boundary is involved, the non-rectangular element, Fig.

3.2(a) is mapped into rectangular one in terms of local coordinates (Fig. 3.2(b)) using a Jacobian matrix, details are given in Appendix B. For this type of element, only the non-centroidal points of velocity need to be solved. The centroidal points of velocity and pressure can be obtained from Eqs. (3.12) and (3.15). To this end, a general matrix $[C]$ is partitioned to separate the centroidal points of variables from the total points of variables

$$[C] = \begin{bmatrix} C_{11} & C_{12} \\ C_{21} & C_{22} \end{bmatrix} \quad (3.11)$$

where

$$[\hat{C}] = [C_{11}] + [C_{12}] [R_0] + [R_0]^T [C_{21}] + [R_0]^T [C_{22}] [R_0] \quad (3.12)$$

and

$$\{v\} = \left\{ \begin{array}{c} \hat{v} \\ v_c \end{array} \right\} \quad \{p\} = \left\{ \begin{array}{c} p_c \\ \partial p / \partial x \\ \partial p / \partial z \end{array} \right\} \quad (3.13)$$

In these, $[R_0] = -[L_{22}][L_{21}]$. The overhead $\hat{\cdot}$ denotes a non-centroidal variable, and the subscript c denotes a centroidal variable.

The continuity equation and the penalty function become:

$$\{v_c\} = [R_0] \{\hat{v}\} \quad (3.14)$$

$$\{p_c\} = \frac{1}{\beta}[D_{11}]^{-1}[L_{11}]\{\hat{v}\} \quad (3.15)$$

3.3 Numerical calculation

The preceding procedures lead to the global, spatially discretized matrix equations of motion for the fluid. For clarity and convenience, Eq. (3.10) is re-written in the form

$$([A] + [N(v)])\{v\} = \{B_c\} \quad (3.16)$$

where the matrices $[N(v)]$ and $[A]$ represent the convective term and diffusive term, respectively.

A large, sparse system of algebraic equations remains to be solved, just like in most other FEM applications to engineering problems. The system of Eq. (3.16) is non-linear due to the convective acceleration. The solution route chosen herein is the iterative method. In order to obtain good initial values, the Stokes solution and Picard iteration, viz.

$$([A] + [N(v^{k-1})])\{v\}^k = \{B_c\} \quad (3.17)$$

$$([A] + [N(v^k)] + [N'(v^k)]) = -([A] + [N(v^k)])\{v\}^k - \{B_c\} \quad (3.18)$$

were used before applying the Newton-Raphson method.

The numerical integration was realized by the 3×3 Gaussian rule, i.e.,

$$\int_{-1}^1 \int_{-1}^1 f(\xi, \eta) d\xi d\eta = \sum_{i=1}^3 \sum_{j=1}^3 w_i w_j f(\xi_i, \eta_j) \quad (3.19)$$

where

$$w_1 = w_3 = 5/9 \quad (3.20)$$

$$w_2 = 8/9$$

$$\xi_1 = \eta_1 = -\sqrt{15}/5$$

$$\xi_2 = \eta_2 = 0$$

$$\xi_3 = \eta_3 = \sqrt{15}/5$$

The linearized algebraic equations were solved by means of a skyline solver. The source code¹ was supplied by the computational fluid dynamics lab of the department (Ethier, 1994).

The applicable boundary conditions were the Neumann conditions on both walls and the assumptions of a parabolic distribution of the streamwise (u) velocity at inlet, and fully developed, spatial periodicity at the exit from the thin-film flow channel. The first attempt of numerical calculation was carried out for only one wavelength. This proved to

¹The code was published originally in Dhatt and Touzot (1984); it was debugged by former CFD group student David Steinman.

be unsatisfactory for the periodic boundary condition and, hence, all subsequent numerical results were based on a flow field containing three wavelengths.

In order to obtain automatic mesh generation, a source code in FORTRAN was exclusively written for this problem prior to the execution of the main software.

3.4 Testing of the solution

In order to verify the code, two well-known examples were chosen, viz. plane-Poiseuille flow between smooth walls, and laminar flow in a channel with a backward-facing step.

For the first case, shown in Fig. 3.3(a), employing 400 elements (20 uniform elements in each direction of the x/z -plane), a ratio of channel length to channel height of 10, and $Re = 100$, the absolute error, defined as the difference of velocities between theoretical and numerical results at each grid point of the flow field, was found to be less than 10^{-5} (see Fig. 3.3(b)). The Darcy-Weisbach friction coefficient is defined as

$$f = 8 \frac{\tau_w}{\rho U^2} = 4 \frac{h_0}{\Delta L} \frac{\Delta p}{\rho U^2} \quad (3.21)$$

where τ_w = wall shear stress, viz.

$$\tau_w = \mu \left(\frac{\partial u}{\partial z} \right)_w \quad (3.22)$$

and Δp = pressure drop over ΔL . Also, the Darcy-Weisbach friction coefficient agreed

with the theoretical plane-Poiseuille value of $f = 96/Re$ with an error smaller than 10^{-4} .

The second test, viz. steady, laminar, incompressible flow over a two-dimensional backward-facing step, is very frequently used as a benchmark test for verifying computational codes. Although the major concerns are usually the details of flow separation at sudden changes in channel geometry, the present work employs an experimentally verified example, available in the literature, to test the soundness of the herein developed finite element code.

The geometry and boundary conditions used in the calculations are defined in Fig. 3.4 where H is the downstream channel height, and the step height and the height upstream of the inlet are $H/2$. The inlet velocity distribution is parabolic. The downstream channel length is $15H$ for all numerical results given in the following. The Reynolds number is defined as $Re = UH/\nu$, where U is the average velocity across the channel.

For a length of the downstream channel of $15H$, the grid system used has 360 9-node uniform rectangular elements, 6 by 60 in the x and z directions, respectively, giving a total of 1573 nodes and 2426 unknowns of velocity.² The numerical results are compared with experimental measurements by Armaly et al. (1983) in Fig. 3.5. No tabular results are given in the reference, and graphical results had to be scaled and interpolated to produce the data shown in Fig. 3.5. In general, there is very good agreement between the present FEM solutions and the experimental results. The discrepancy at $x/H = 7$ for $Re = 1000$,

²For comparison, Armaly et al. (1983) used a 2025 (45x45) grid for their backward-facing step analysis by the TEACH software.

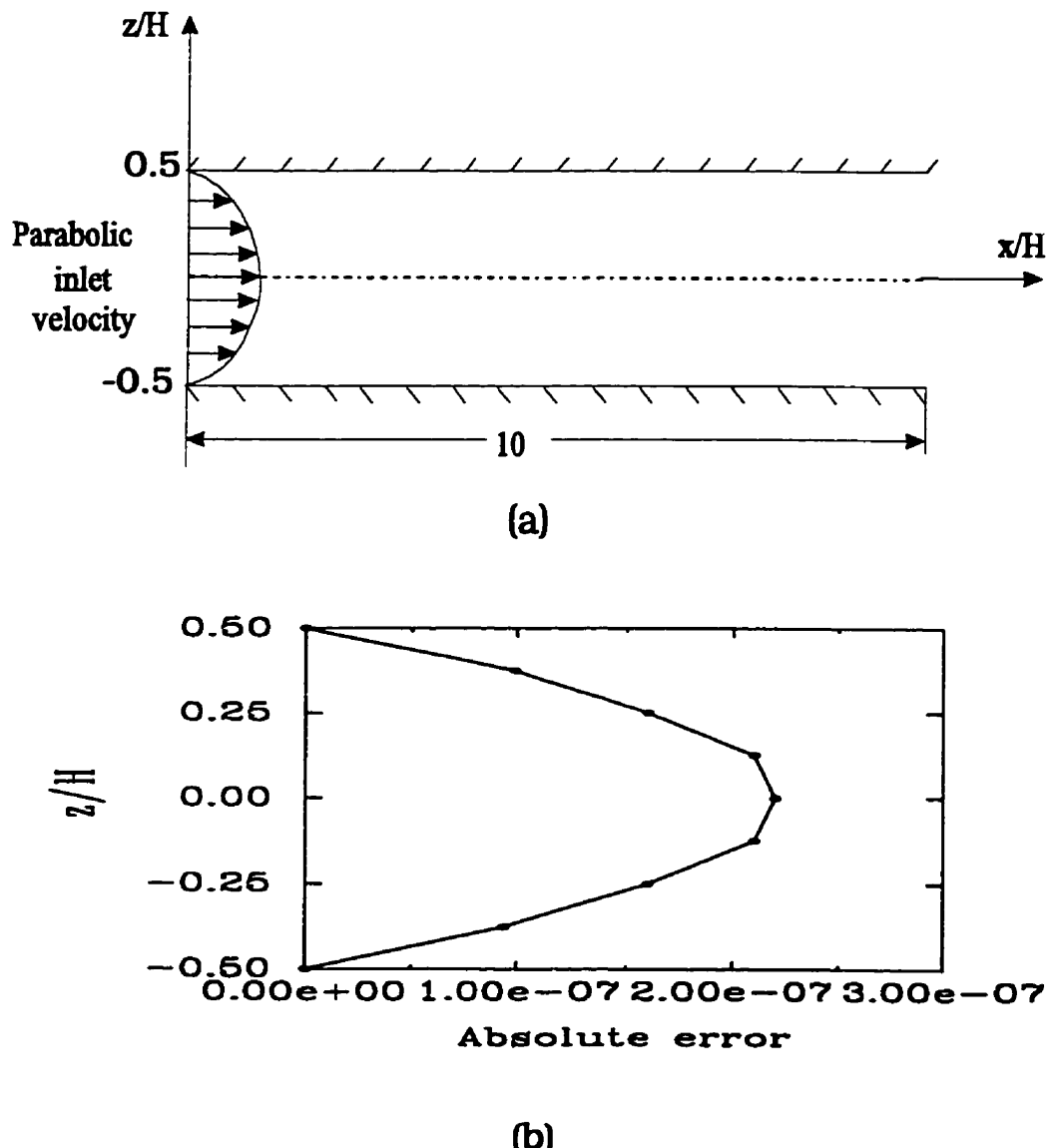


Figure 3.3: (a) Definition diagram of plane Poiseuille flow; (b) Error distribution over cross-section

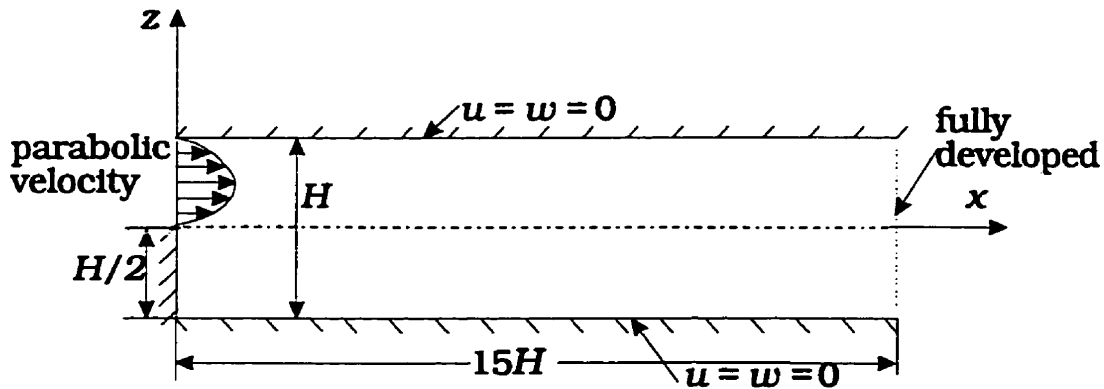


Figure 3.4: Definition diagram of laminar flow over a backward-facing step

see Fig. 3.5(i), is likely due to the development of three-dimensionality of flow structure in the experiment.

The current FEM solution is also compared with relevant results obtained by Gartling (1990) with a finer mesh at a Reynolds number of 800. Fig. 3.6 shows a comparison of the predicted velocity distribution by Gartling and the present FEM. In Gartling's work the results were obtained with a 8000(20×400) mesh, $30H$ long in downstream direction. The velocity distributions are practically identical.

The length of the separation bubble at the lower wall is $5.75H$ by the present FEM, and $6.10H$ by Gartling's. The length of the circulation region at the upper wall is $5.25H$ and $5.63H$, respectively. The differences are due to the greater length of flow field used by Gartling. The streamline contours, shown in Fig. 3.7, demonstrate flow separation and reattachment at $Re = 800$ according to the present FEM.

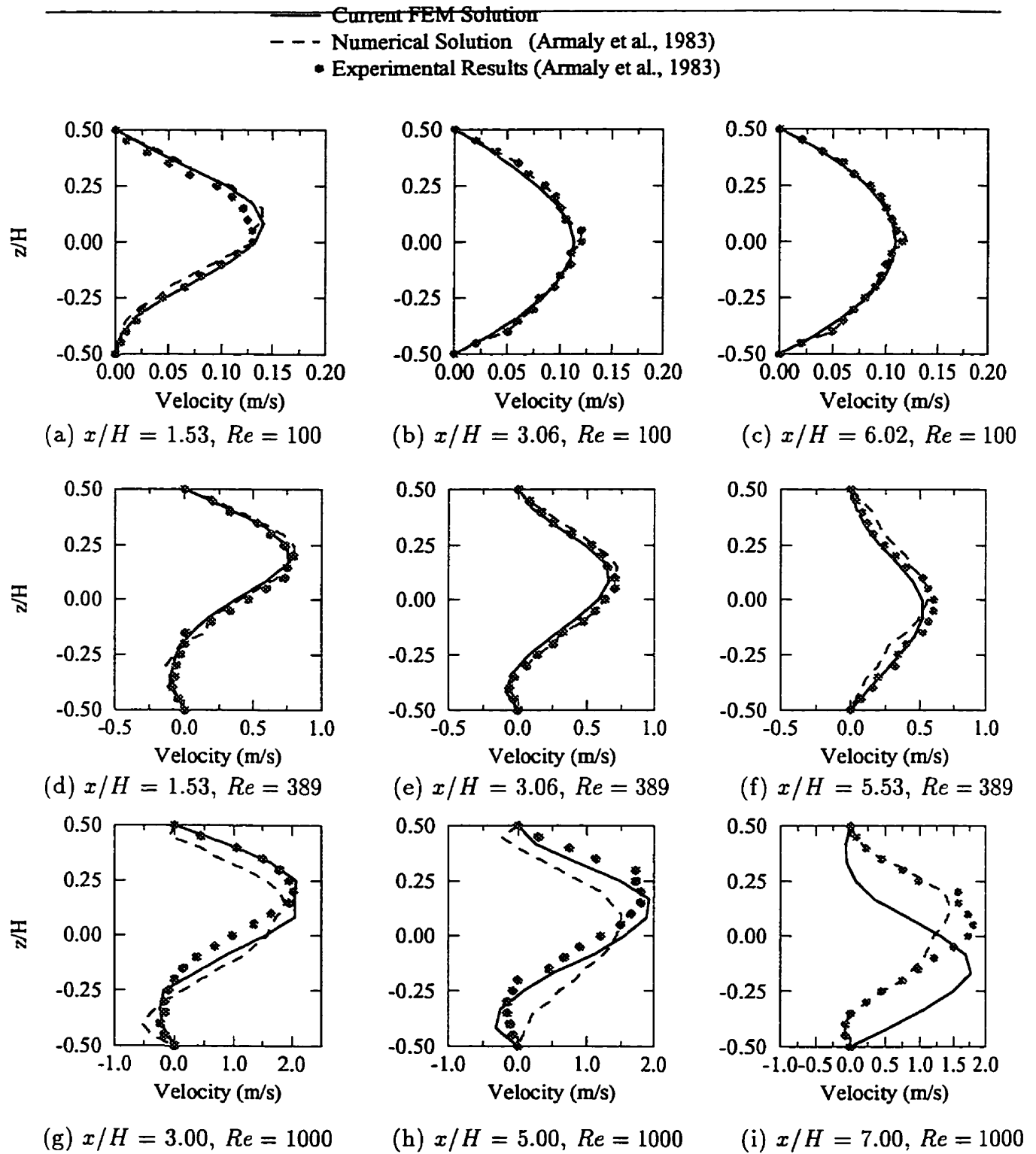


Figure 3.5: Transverse velocity profiles along channel with backward-facing step, at various Reynolds numbers: numerical predictions vs. experimental findings

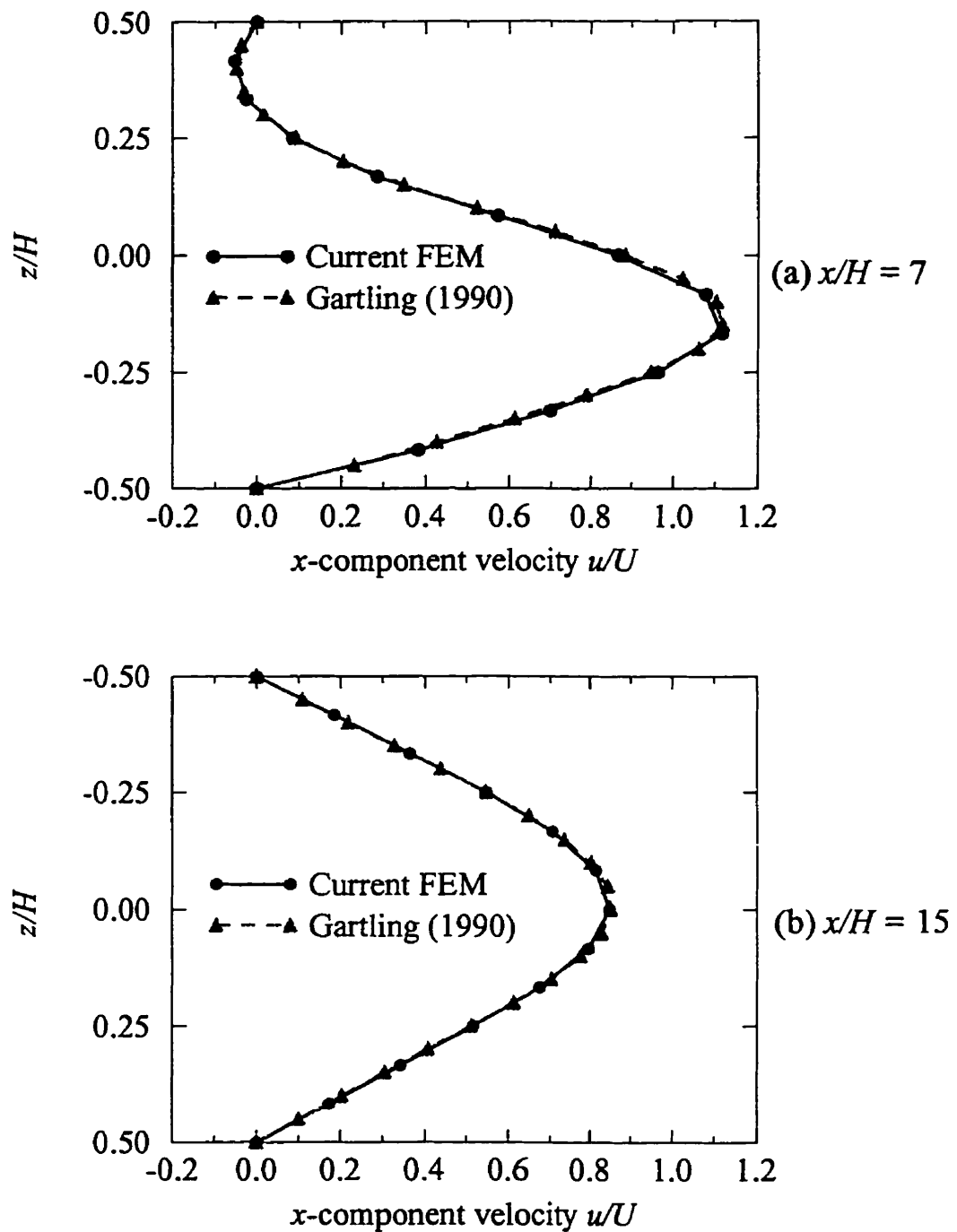


Figure 3.6: Transverse velocity profiles along channel with backward-facing step obtained with two different meshes, at $Re = 800$

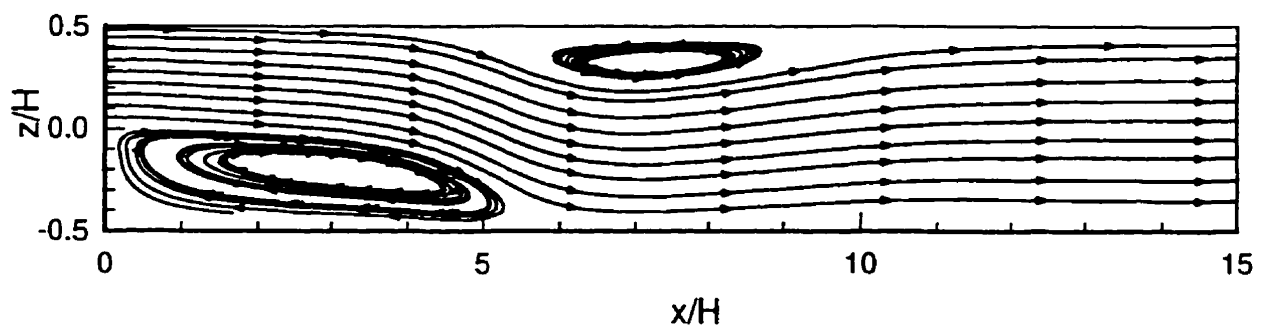


Figure 3.7: Streamline contours of flow over backward-facing step at $Re = 800$

Chapter 4

Experimental Facilities

4.1 The air duct

Several key questions associated with the projected experimental facility had to be resolved prior to its design and construction.

The first problem was to choose a suitable fluid medium. Compared with a liquid, air as the testing fluid offers significant advantages: it needs no circulation system and storage reservoir; well established wind tunnel techniques may be applied; and, from a practical point of view, structural and sealing demands are minimal. One other thing worth mentioning is that cavitation on surface roughness elements, which may happen in a liquid lubricating film, does not occur.

The experimental method of modeling in air what of are essentially liquid flow phenomena has been applied before in the laboratory of the department, albeit mostly un-

der turbulent flow conditions. Tsanis and Leutheusser (1988) studied wind-driven lake currents, Aydin and Leutheusser (1991) investigated plane Couette flow between smooth and bi-laterally rough walls, and Innes and Leutheusser (1991) determined the critical Reynolds number of laminar-to-turbulent transition for tilting-pad bearings. In contrast to the foregoing studies, the present investigation deals exclusively with laminar flow in a two-dimensional wind tunnel of which one long side wall can be roughened.

The next problem was to determine the target ranges of the required average flow velocity U and the reduced Reynolds number Re^* . The kinematic viscosity of air at 20°C is $1.51 \times 10^{-5} \text{ m}^2/\text{s}$. From surface measurements available in the literature, the magnitude of the average roughness R_a of a ground steel surface is about 1 μm , and the maximum peak-to-valley height is about 15 μm . Adopting a linear magnification factor (i.e., model scale) of 1000, this translates to 1 and 15 mm, respectively. For a channel height h_0 of up to 30 mm, comparable to the value of the peak-to-valley of height of the enlarged roughness, and assuming the flow to be laminar at $Re \leq 2000$, the average velocity U falls between 0.10 and 1.2 m/s, and the maximum value for the reduced Reynolds number Re^* is less than 1.0. The values of h_0 and U are the keys to the determination of the other dimensions of the facility and the selection of the required air blower. The value of Re^* ensures that the facility can provide the flow state which is realized in a typical prototype situation.

The values of the various system parameters were selected to fall within the ranges as encountered in actual lubrication practice. For instance, taking the typical case of a 26.7 cm (10.5 in.) diameter thrust bearing with $R_a = 1 \mu\text{m}$, $\lambda_a = 50 \mu\text{m}$ and $h_0 = 30$

μm , lubricated by a light turbine oil, such as ISO VG32, with a kinematic viscosity $\nu = 31.8 \times 10^{-6} \text{ m}^2/\text{s}$ at 37.8°C (100°F), operating at a mean relative velocity $U = 90 \text{ m/s}$, see Gregory (1975), the flow in the film would be laminar with $Re = 175$ and $Re^* = 0.056$. For a more normal working temperature of the film of close to 100°C the corresponding values would be $Re = 1050$ and $Re^* = 0.35$. These results show that the air duct is well capable of reproducing actual lubrication conditions.

The final problem was to decide on the length and the width of the apparatus. To ensure fully-developed flow, a length of 4 m was chosen in accordance with the required minimum development length, L_d , of plane Poiseuille flow, viz. (Schlichting, 1968)

$$L_d/h_0 = 0.06Re . \quad (4.1)$$

In order to minimize the effects of side walls and not to exceed local space limitations, a duct width of 50 cm was chosen. This, then, yielded a duct cross-section with aspect ratio of, at least, 10.

The finished experimental apparatus is an essentially two-dimensional, low-speed wind tunnel of adjustable height to maximum 5 cm, 50 cm width, and 4 m length. It is presented schematically in Fig. 4.1. The tunnel is located in the Flow Systems Laboratory of the department. Ancillary equipment provides for the measurement of velocities by hot-wire anemometry, and flow visualization by the smoke-wire method. No arrangements are made for monitoring the extremely small pressure drop of the laminar air flow along the duct.

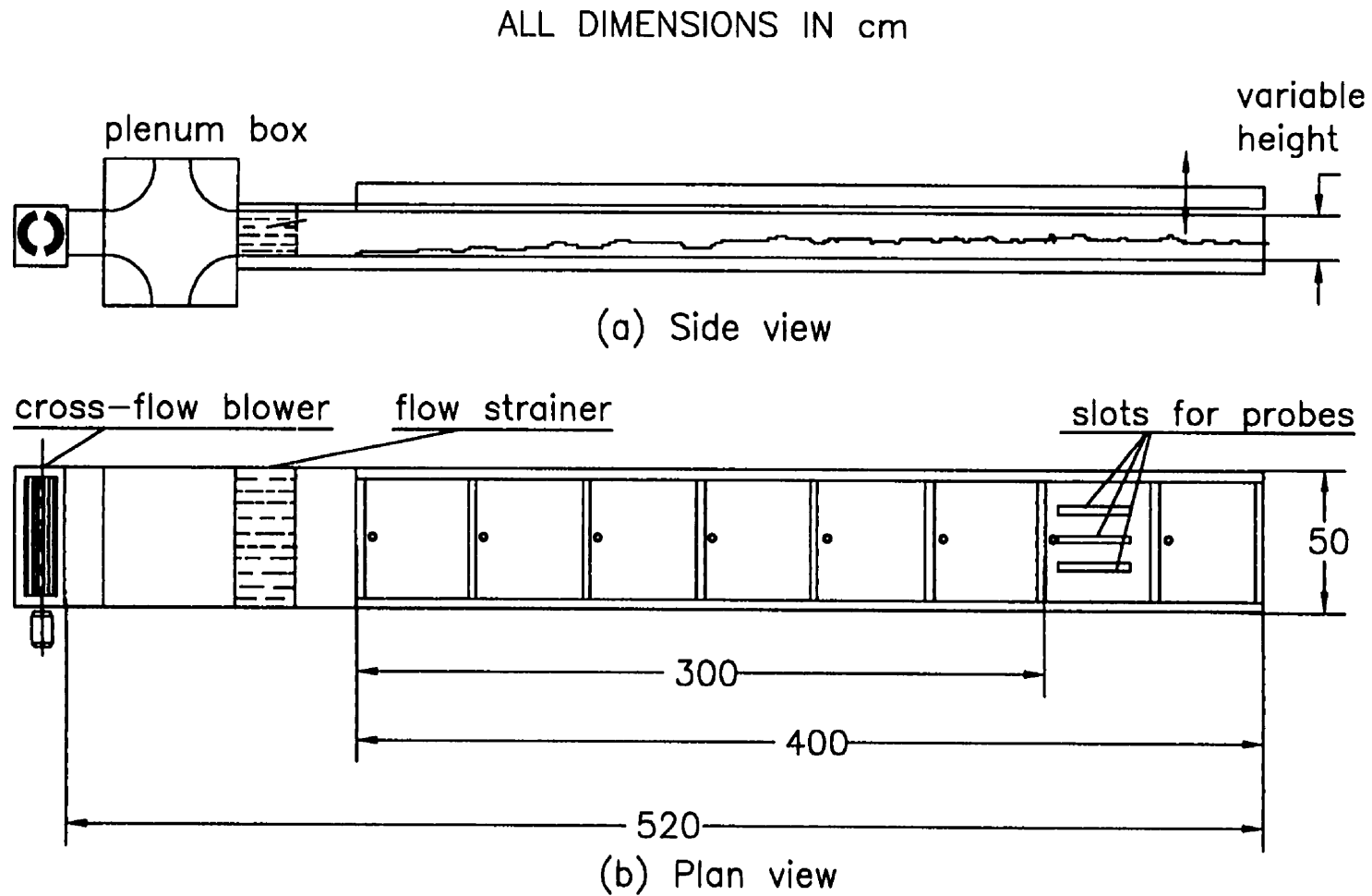


Figure 4.1: Schematic diagram of the experimental set-up

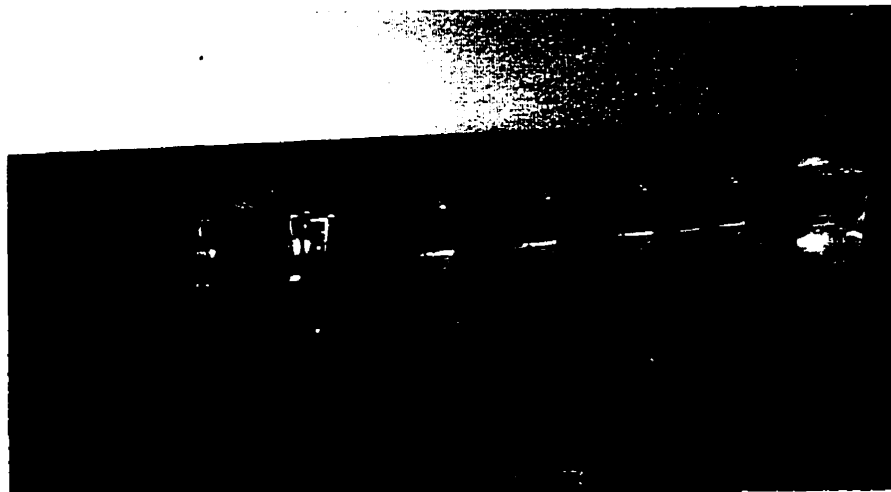


Figure 4.2: Photograph of the Dayton cross-flow blower

In order to achieve optimum uniform velocity distributions over the cross section, air flow is produced by a variable-speed cross-flow blower (Model 4C848, Dayton Electrical Manufacturing Co., Chicago, IL.), see Fig. 4.2, discharging into a large stilling chamber and thence, by way of a honeycomb composed of tightly packed drinking straws, into the duct proper.

The bottom wall of the duct is made of plywood (Fig. 4.3(a)). It is solidly supported on a rigid bench and carries the wall texture to be investigated in the form of an interchangeable layer. The surface of the bottom wall was adjusted horizontally by means of a level transit (Fig. 4.3(c)).

Top and side walls (Fig. 4.3(b)) of the duct are made of plexiglass to facilitate flow observation. To prevent warping of the top panel, a welded frame of 2.5 cm (actually 1 in.) square aluminum tubing was built to render the large plexiglass sheets rigid. The top surface of the wind tunnel is arranged in such a way that the depth of the duct can be

readily changed from practically zero to about 5 cm. This is effected by a system of nuts and bolts between five sets of cross bars and pi-shaped suspension stands placed one meter apart. The cross bars are attached to the top of the duct, while the suspension stands are fastened to lateral extensions of the bottom wall. Air leakage from the slightly pressurized duct to the outside is prevented by clamping the side walls against top and bottom, and by applying duct tape to cover all cracks.

During a test the bulk Reynolds number Re is monitored routinely by a hot-film probe permanently installed near the outlet from the honeycomb. Tapping points along the length of the duct make it possible to access its interior for measurement and smoke injection for flow visualization. However, most of the flow studies are performed near the exit from the wind tunnel. The photograph of Fig. 4.4 gives a physical impression of the facility.

4.2 Models of surface texture

Plaster of Paris was used to reproduce geometrically similar but linearly enlarged version of various types of surface texture, such as smooth, sinusoidally wavy, and randomly rough, and to install these as layers on the plywood floor of the wind tunnel. For reasons of practicality, each layer is segmented into square tiles measuring 25 cm by 25 cm, with a minimum thickness of 1 cm to ensure strength in carrying. A total of 32 tiles is required to prepare the wind tunnel for a particular test series. Each set of tiles is cast from a carefully machined master mould.

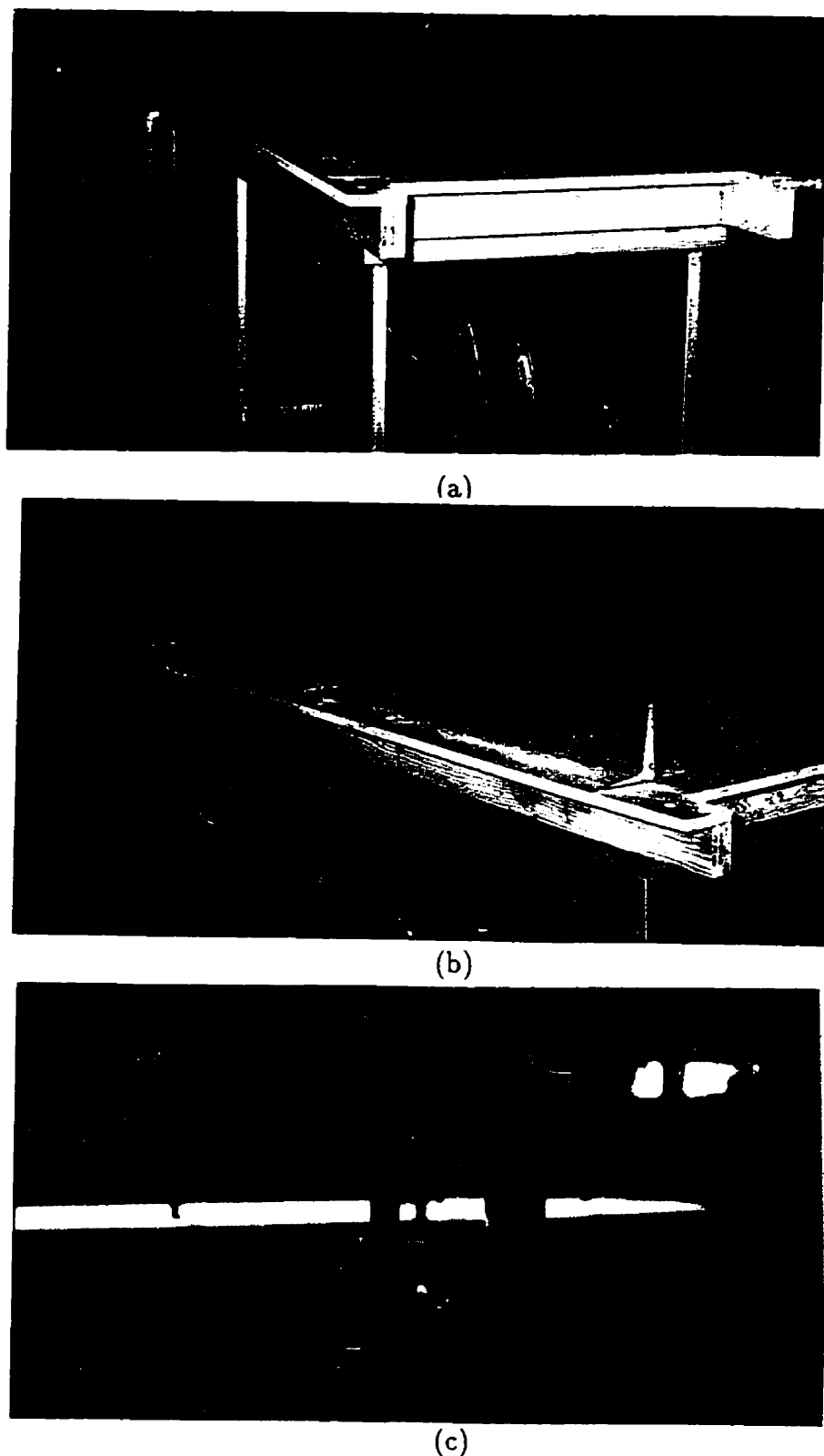


Figure 4.3: Photograph of the building process of the experimental set-up: (a) duct bottom; (b) side walls; (c) levelling of the structure

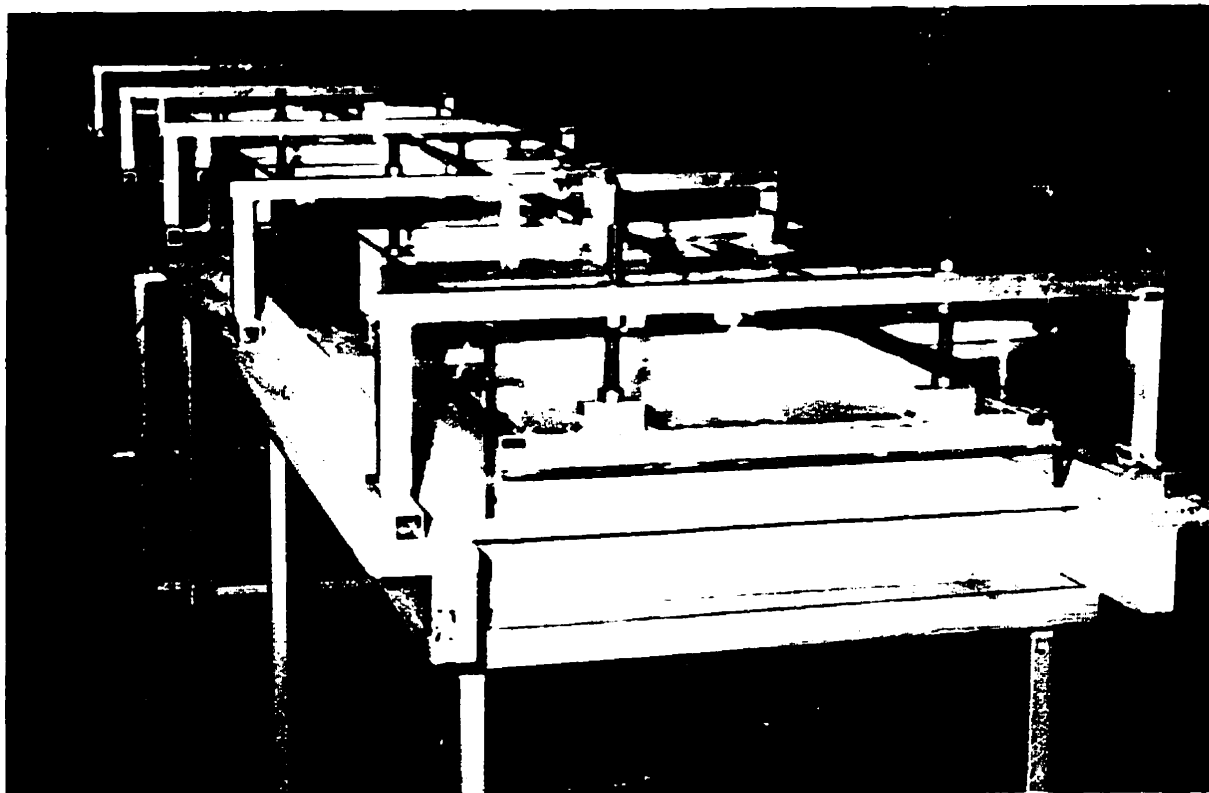


Figure 4.4: Photographic overview of the experimental set-up

4.2.1 Randomly rough surface

Random surface roughness is patterned after the conditions of actual bearing pads supplied by Kingsbury Inc. of Philadelphia, PA. The photograph of Fig. 4.5 shows one of six bearing pads of a 30 cm diameter thrust bearing with lapped (i.e., very smooth) surface finish.

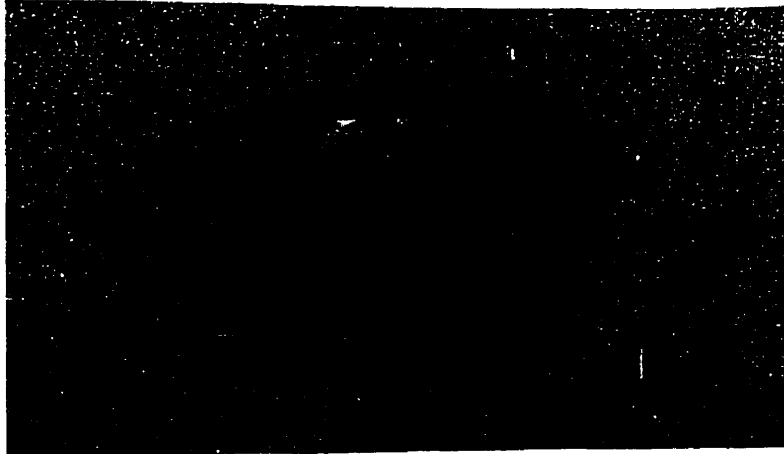


Figure 4.5: One segment of a tilting pad bearing

Surface profile measurements were done by a technician at the Research Laboratory of Ontario Hydro, using a three-dimensional surface measurement system. This includes a $4 \mu\text{m}$ diameter stylus, a Hommel America Profilometer, a Daedal microplacement stage driven by stepping motor with controller, a regular A/D converter, and a personal computer to record the discrete data for further analysis (see Fig. 4.6).

From the experimental results obtained with the surface profiler, the two selected parameters, viz., the average roughness height R_a and the average wavelength λ_a (see Appendix B) were calculated. It has been reported (Moalic et al., 1989) that the average profile slope, and hence, the wavelength (like other areally related statistical parameters) is dependent on the sampling interval. The average slope increases when the interval decreases. Mc-

Cool (1985) suggests that at least eight points per cycle are needed, when calculating these parameters in order to avoid serious error.

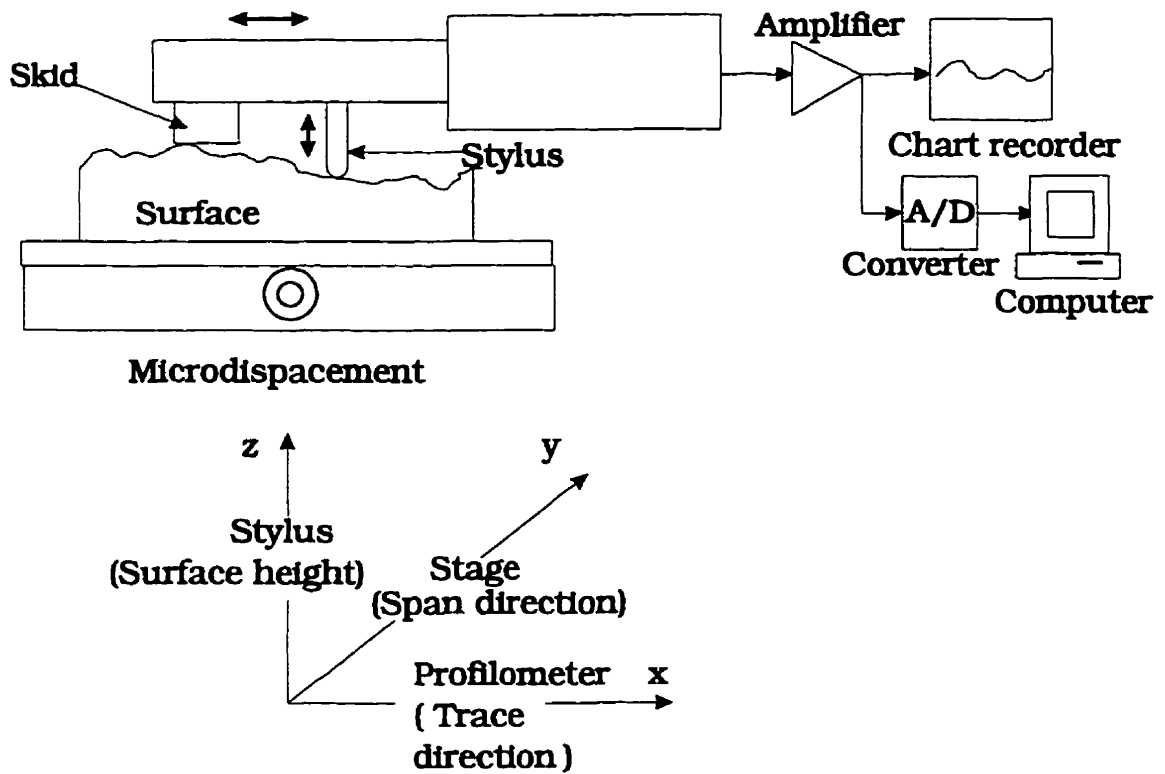


Figure 4.6: Schematic of three-dimensional surface measurement system

Roughness measurements over an area of 3 mm by 3 mm, in the centre of the pad of Fig. 4.5, are depicted in Fig. 4.7. The spatial interval is $24 \mu\text{m}$, which is determined by the maximum number of sample data recordable by the system, viz. 125 in each direction. The measurements suggest an average roughness $R_a = 0.633 \mu\text{m}$, a rms of area $R_q = 0.809 \mu\text{m}$, the average slope of one profile $\Delta_a = 0.0358$, and a corresponding average wavelength $\lambda_a = 108 \mu\text{m}$.

In order to get more refined values of the parameters of roughness and corresponding

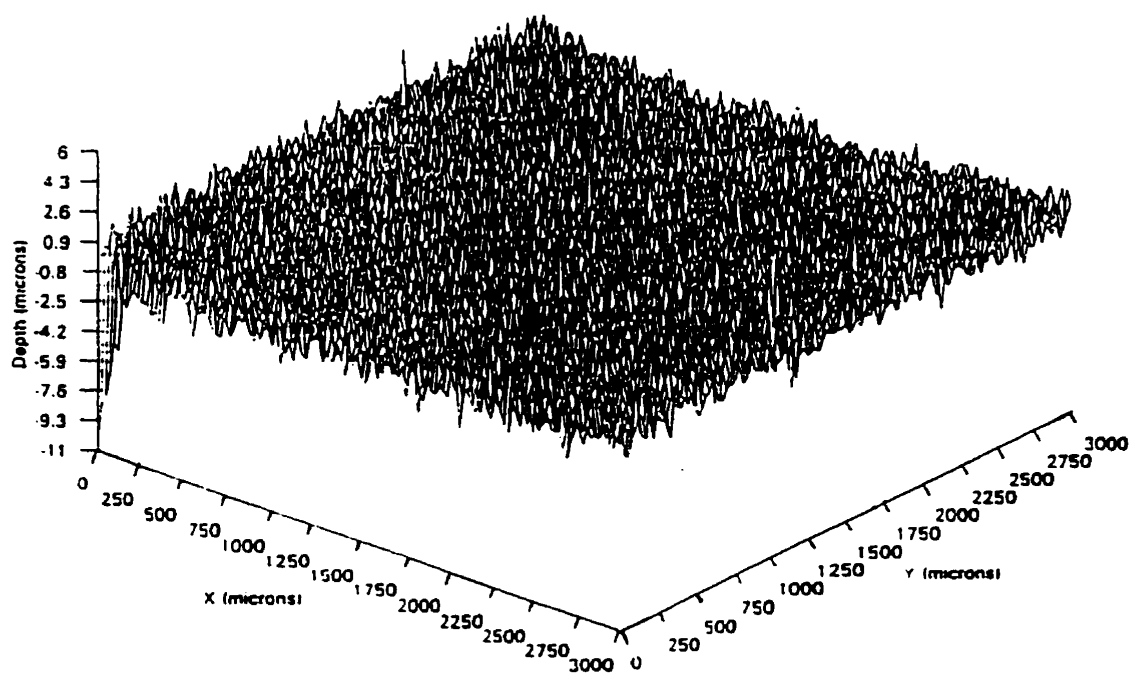


Figure 4.7: Surface topography of the bearing pad (3.0mm × 3.0mm)

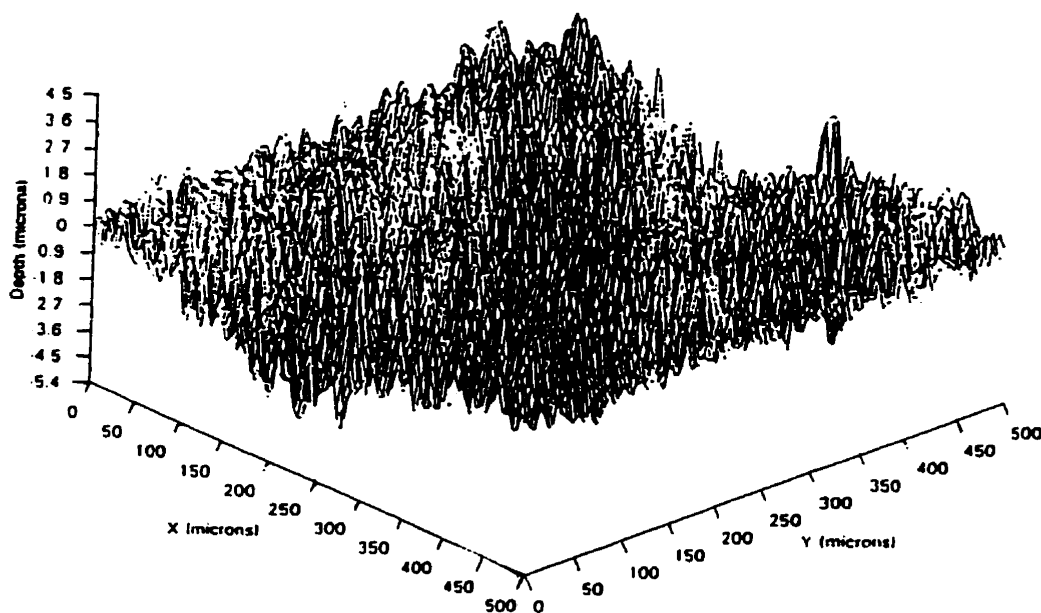


Figure 4.8: Surface topography of the bearing pad (0.5mm × 0.5mm)

surface profile, a square segment of the bearing surface with a side length of 0.5 mm was measured. The resulting topography is shown in Fig. 4.8. For the same maximum number of sample data as before, this measurement at a spatial interval of 4 μm gives a smaller value of the average wavelength, viz. $\Delta_a = 0.106$ and $\lambda_a = 49.3\mu\text{m}$, but the same magnitude for the average roughness and the average root mean square roughness, viz. $R_a = 0.832\mu\text{m}$ and $R_q = 1.01\mu\text{m}$. In the latter calculation, there are more than ten points per cycle of a surface profile undulation involved. Apparently, the previous sample interval of 24 μm does not yield a satisfactory approximation, supplying only about 6 points per cycle.

The above average roughness and wavelength values of, respectively, $R_a = 0.832\mu\text{m}$, $\lambda_a = 49.3\mu\text{m}$, when translated into dimensions enlarged at a linear scale of 1000:1, give the values of 0.832 mm and 49.3 mm, respectively. These are tangible quantities which can be physically reproduced in the model and, thus, their fluid dynamic effects can be tested.

4.2.2 Sinusoidally wavy surface

Fig. 4.9 shows a photograph of the master tile for a sinusoidally wavy surface with amplitude and wavelength of , respectively, $\delta = 3 \text{ mm}$ and $\lambda = 250 \text{ mm}$. The values of amplitude and wavelength were chosen arbitrarily but comparable with the corresponding magnitudes of the real bearing surface discussed in the foregoing.

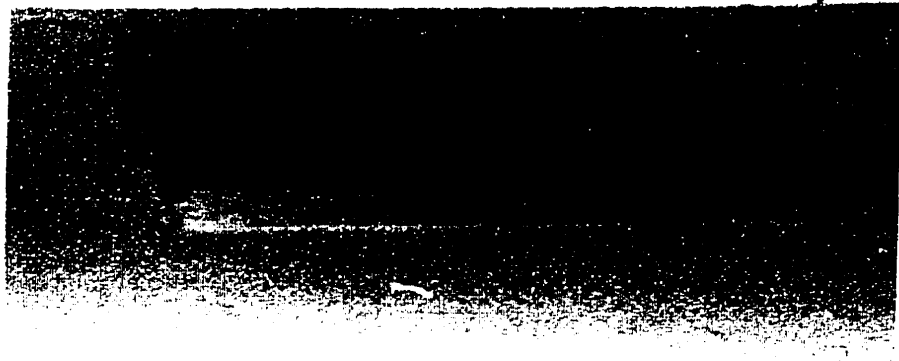


Figure 4.9: Master tile of the sinusoidally wavy wall

4.2.3 Physically smooth surface

In order to compare the experimental measurements from the samples of randomly rough and sinusoidally wavy walls with those from a physically smooth surface, a full set of smooth surface tiles was also made out of Plaster of Paris.

4.3 Hot-wire anemometry

Because of the low velocities encountered in laminar air flow, measurements in the present study are principally effected with the aid of hot-wire anemometry.

DISA P14 single wire probes are used for measuring the velocity of parallel flow. Because of the two-dimensional nature of the flow close to the rough surface, X-wire probes of type DISA P61 & P63 are generally employed. The sensing wires of the probe are made of platinum-plated tungsten, have a length of 1.25 mm and a diameter of 5 μm . In order to achieve a high velocity sensitivity, an overheat ratio of 1.8 is used for both measurements and calibration (Bruun, 1994).

The ancillary electronic equipment comprises a DISA 55M system composed of 55M01 main unit, 55M10 Constant Temperature Anemometer(CTA) standard bridge, and 55D31 digital voltmeter. Other regular equipment involved are oscilloscope and power supply. For probe calibration and data recording are used an A/D board (PCL-812), a 486/33Mhz IBM-compatible computer, with the software developed by Dziedzic(1994).

During tests, the hot-wire probe can be moved vertically by means of a step motor and horizontally via a 2-D traversing mechanism. For the calibration of the sensors, a rotating table with known speed characteristics was employed, see Fig. 4.10.

The classical equation relating voltage, required for keeping the wire temperature constant, to flow velocity is King's formula, viz.



Figure 4.10: Photograph of probe calibration system

$$\frac{E^2}{R_w - R_g} = A_c + B_c U_{eff}^{n_c} \quad (4.2)$$

where E = voltage; R_w and R_g = hot and cold resistances; A_c, B_c, n_c = calibration constants, and U_{eff} = effective velocity sensed by the hot-wire, i.e., U_0 for a single wire probe, and U_1, U_2 for x-wire probe. The calibration system is shown as Fig. 4.10.

Before a calibration, the adjustable rotating speed of the turntable was measured. This was done by videotaping ten turns of the marked 1-m disk at different settings of its speed indicator dial.

The turntable can rotate at speeds of 8 to 68 rpm. With the hot-wire probe positioned

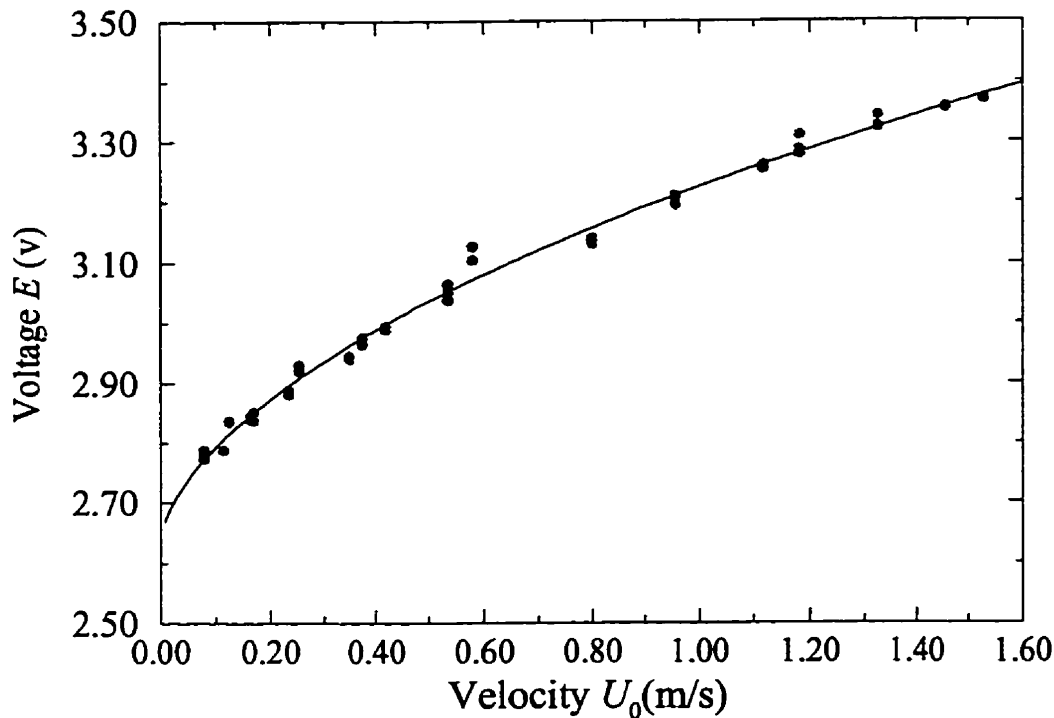
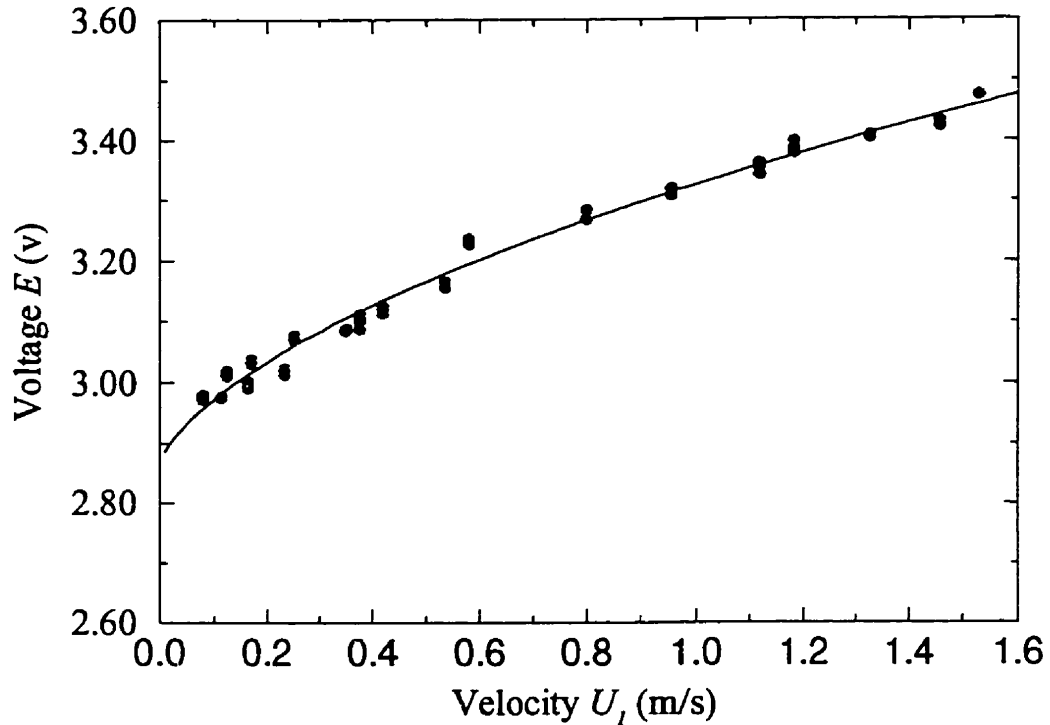
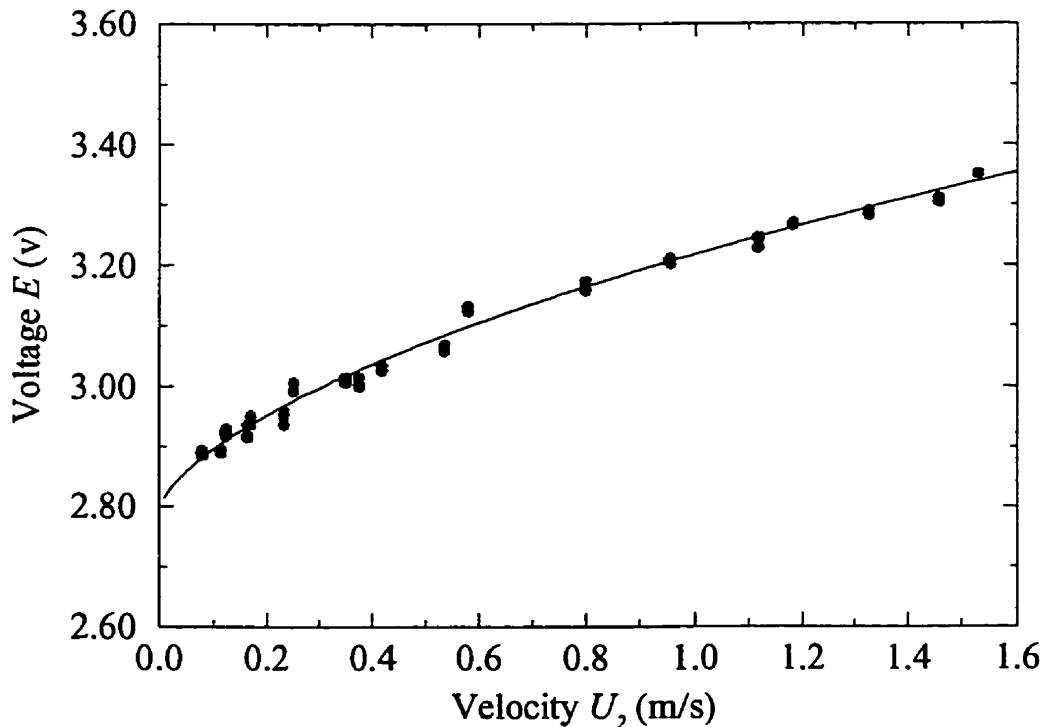


Figure 4.11: Calibration curve of P14 single wire probe

radially from the disk centre at 9.5 cm, 19.5 cm, 39.5 cm and 44.5 cm, the relative velocity of the probe is the tangential velocity at that position, ranging from 0.08 to 1.5 m/s, These values agree with the velocities encountered in the present study which are usually less than 1 m/s.

Fig. 4.13 shows an example of the calibration curve for a DISA type P14 single wire probe. While the two calibration curves of a P63 X-wire probe are shown as Fig. 4.11 and 4.12.

Figure 4.12: Calibration curve of x -component of P63 X-wire probeFigure 4.13: Calibration curve of z -component of P63 X-wire probe

4.4 Flow visualization

The vector character of the flow velocity calls for measurements of both magnitude and direction. Accordingly, velocity measurements undertaken in this study are guided and complemented by flow visualization using the smoke-wire technique. There are a variety of methods to generate smoke for experiments in fluids (Merzkirch, 1987). Several approaches were tried before the smoke-wire technique (Corke et al., 1977; Torii, 1979) was considered to be the best one suited for producing stable smoke filaments. In this method, the smoke is generated by pulsed electric heating and evaporation of an oil film (usually paraffin oil) uniformly coating a metal wire. The wire, about 0.1 mm in diameter, is made of stainless steel and placed vertically in the flow. The smoke-wire technique produces relatively fine smoke lines in an air stream. Its readily controlled spatial and temporal behaviour facilitates its use in research.

There are essentially two ways to apply the oil coating to the wire. The manual one requires to wipe the wire with a cotton-tipped applicator, possibly using a remotely-controlled mechanism, such as a bicycle brake cable (Innes, 1987). The other way is to continuously force the oil down the wire from a reservoir (Corke et al., 1977). In order to obtain continuous fine streamlines an oil reservoir similar to the one used by Corke et al. (1977) was developed in the present application of flow visualization.

Available instrumentation in the department, previously built by Tsanis (1986) according to Torii's (1979) design, includes a high energy pulse generator and nickel-chrome wire

of 0.1 mm diameter. The required energy, and duration and interval of its application in terms of milliseconds are monitored by a Hewlett Packard 5304A timer/counter. The wire is suspended vertically from a supporting arm in the centre plane of the wind tunnel, 1 m upstream from its exit, and observations of the pulsed smoke plume are recorded by video and still photography. Lighting of the smoke scene is provided by a light sheet emitted from a slide projector installed above the position of observation.

Video instrumentation employed includes a Panasonic TV camera, model MV-1500; a 4-head video cassette recorder, model Omnidivision II (VHS); and a TV monitor. For the analysis of the taped observations, photographs were taken with a Nikon F3 Camera directly from the TV monitor, stilled by the frame-play mode of the VCR. Photographic films (T-MAX 100 black and white) were processed and printed by the writer in a darkroom of the department.

Chapter 5

Results for Unilateral Sinusoidally Wavy Wall

5.1 Numerical solution obtained by FEM

For the case of laminar sheet flow between a flat wall and a sinusoidally wavy one as shown in Fig. 3.1, including three wavelengths, a total of 480 elements (48 and 10 grid intervals in x and z directions, respectively) was used (see Appendix E). Hence, there were $2037(97 \times 21)$ grid points and 3114 [$2 \times (2037-480)$] unknowns. The number of boundary grid points is 464. To achieve automatic generation of the mesh system, the whole domain area of one wavelength was divided along the z -axis into two parts: the first part extended between the sinusoidal wall and one third of the channel height, with the mesh size increasing in geometrical progression; the balance of the area was discretized into rectangles.

The effects of the reduced Reynolds number may be viewed from Figs. 5.1 and 5.2. There is no obvious effect of an increase in Re^* on the overall distribution of the non-dimensional velocity, an observation which is confirmed by the max/min-values of Figs. 5.7 through 5.13. However, on detailed inspection of the streamlines especially in the troughs, or wall “cavities” (Fig. 5.2), a somewhat different picture emerges. Circulation of flow starts in Fig. 5.2(a), gradually increases with increasing Re^* , until it involves the whole cavity in Fig. 5.2(c). Since in the present instance there is no change in either relative roughness ϵ or steepness γ , the increase in the reduced Reynolds number Re^* means an increase of the bulk Reynolds number Re . The variation of circulation and back flow in cavities as functions of bulk Reynolds number Re has been studied by Patel, Chon and Yoon (1991) and Ralph (1987) for various other cases of wavy walls. The present results are similar to theirs.

The effects of changing the relative roughness are elucidated in Fig. 5.3 where four velocity profiles, each with a different value of ϵ , are displayed for fixed values of Re^* and γ . While the distribution of the velocity u/U becomes more “compressed” with increasing relative roughness, small changes occur only in the cavity circulation (Fig. 5.4).

It follows from this that micro-inertia effects, which are essentially due to the churning flow in the driven cavities, appear to be practically independent of relative roughness ϵ if Re^* is fixed. Since, by Eqs. (2.6), (2.8), (2.9) and (2.10),

$$Re^* = \frac{UR_a^2}{\nu\lambda_a} = \frac{1}{2} \frac{U2h_0}{\nu} \frac{R_a}{h_0} \frac{R_a}{\lambda} = \frac{1}{2} Re\epsilon\gamma \quad (5.1)$$

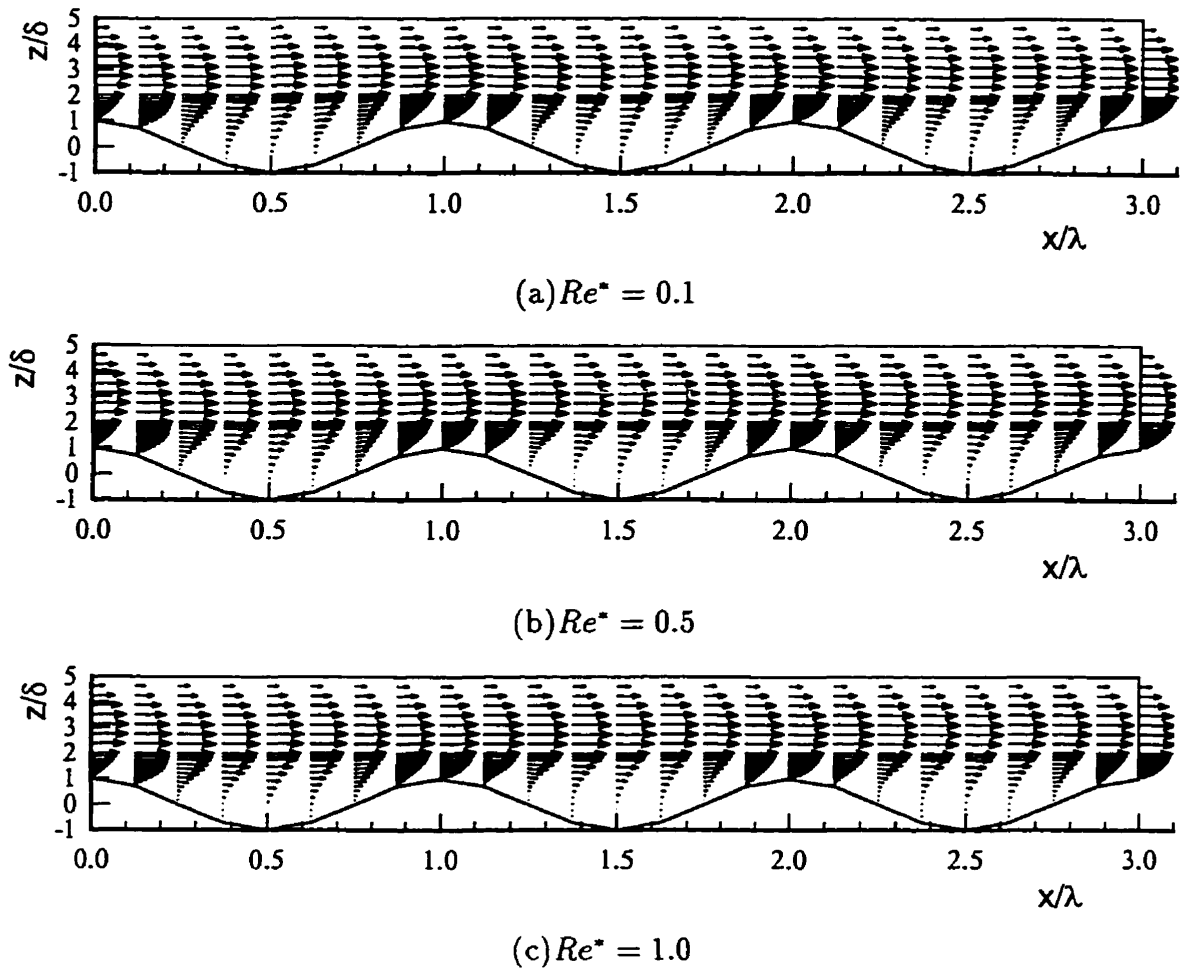


Figure 5.1: Plots of u/U for various reduced Reynolds numbers Re^* ; $\epsilon = 0.2, \gamma = 0.2$

this also means that, for given steepness γ , a flow will behave more tortuous for increasing relative roughness ϵ when the bulk Reynolds number Re is fixed.

Figs. 5.5 and 5.6 show the effects of changing the parameter of steepness γ at constant reduced Reynolds number Re^* and relative roughness ϵ . As would be expected, there is a significant increase in cavity activity with increasing steepness γ .

Figs. 5.7 to 5.10 give profiles of the non-dimensional velocities u/U and w/U at max-

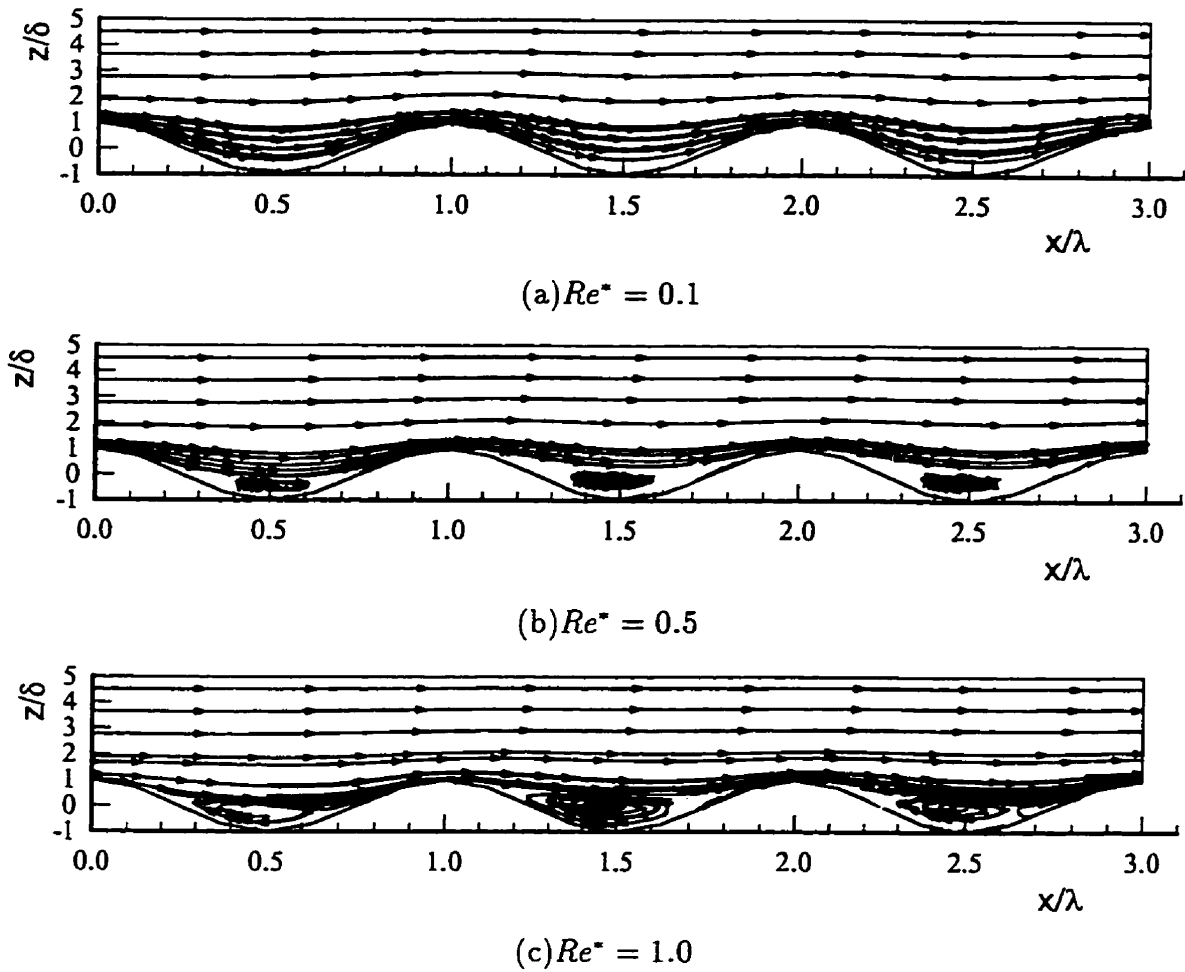


Figure 5.2: Streamlines at various reduced Reynolds numbers Re^* ; $\epsilon = 0.2, \gamma = 0.2$

imum and minimum channel positions for various values of the reduced Reynolds number Re^* and relative roughness ϵ with fixed steepness $\gamma = 0.1$. Corresponding presentations for constant $\epsilon = 0.3$ but variable γ are shown in Figs. 5.11 through 5.14. The outstanding feature of these two series of diagrams is the relative insensibility of both velocity components u/U and w/U to changes in Re^* .¹ On the other hand, there is a clear tendency toward

¹The plotting scales used for w/U are not identical with those in the u/U diagrams.

instability of the u/U -profiles in the cavity regions of the wavy wall with increases of both relative roughness ϵ and steepness γ .

The wall shear stresses were calculated by the backward difference (3^{rd} order) formula of velocities multiplied by the viscosity at relevant grid points. The accuracy of the calculation is proportional to the product of the square of grid interval and the third derivative of the velocities. For the typical case, a deep cavity wall with $\epsilon = 0.3$ and $\gamma = 0.3$ (cf. Fig. 5.3(d)), the shear stress obtained from the mesh with 480 elements has an uncertainty of 1.6% when compared with the corresponding result of the mesh with 720 elements.

Figs. 5.14 through 5.17 show the effects of changing relative roughness ϵ on the distribution of the non-dimensional local wall shear stress $\tau_w/\rho U^2$ over one wavelength for a fixed reduced Reynolds number Re^* . The magnitude of $\tau_w/\rho U^2$ in the accelerated flow (or minimum area) region of the channel increases with both γ and ϵ . At the same time, however, flow separation develops in the cavities as evidenced by the reversed, i.e., upstream, direction of the shear stress there.

The effect of the reduced Reynolds number Re^* on the wall shear stress $\tau_w/\rho U^2$ can be assessed from 5.18 where relative roughness ϵ and steepness γ are fixed. There is only a slight increase in the magnitude of shear stress with a decrease in reduced Reynolds number Re^* . But this is accompanied by a significant growth in flow reversal. Clearly, micro-inertia effects and churning cavity flows are one and the same.

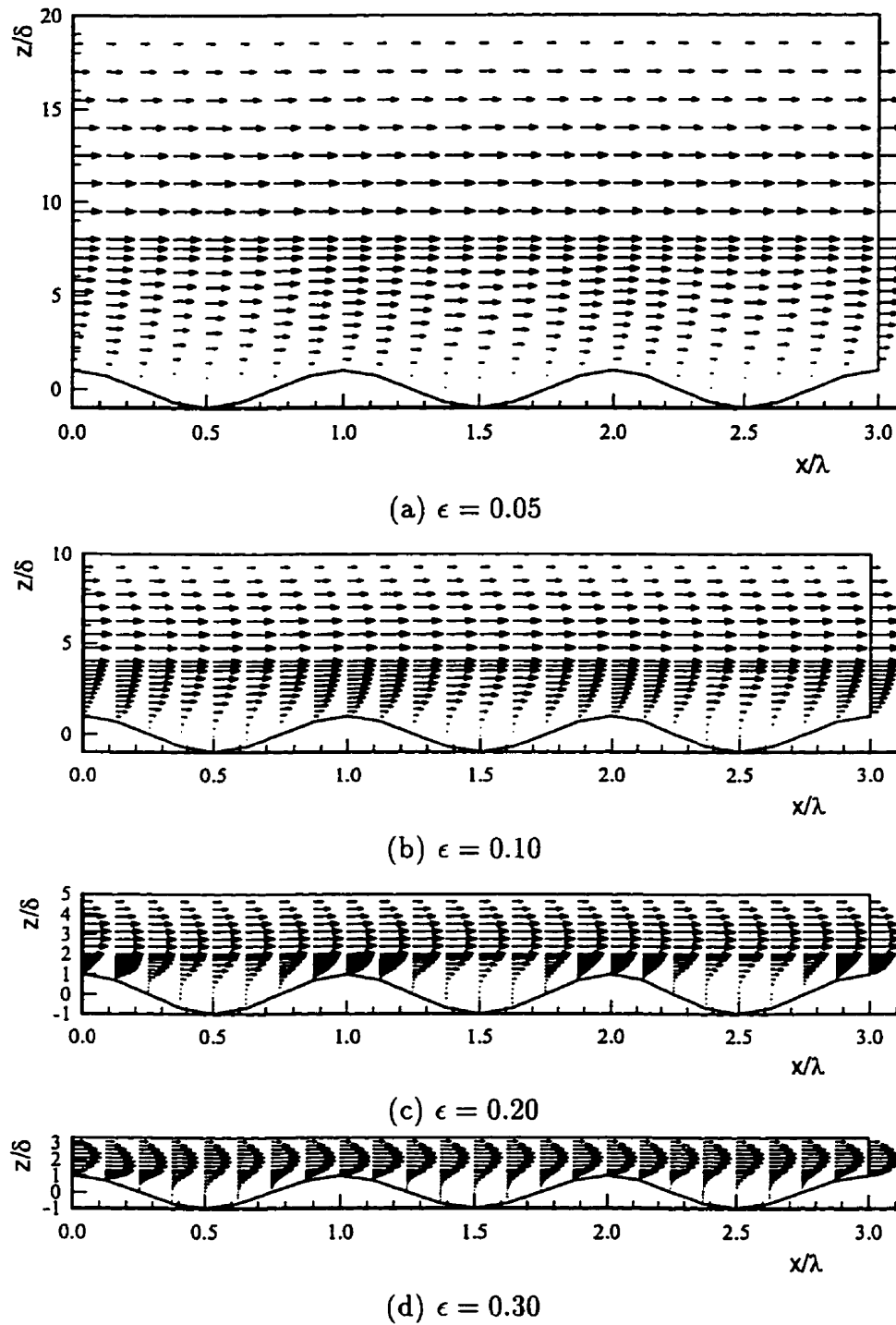


Figure 5.3: Influence of relative roughness ϵ on distribution of u/U ; $Re^* = 1.0$, $\gamma = 0.3$

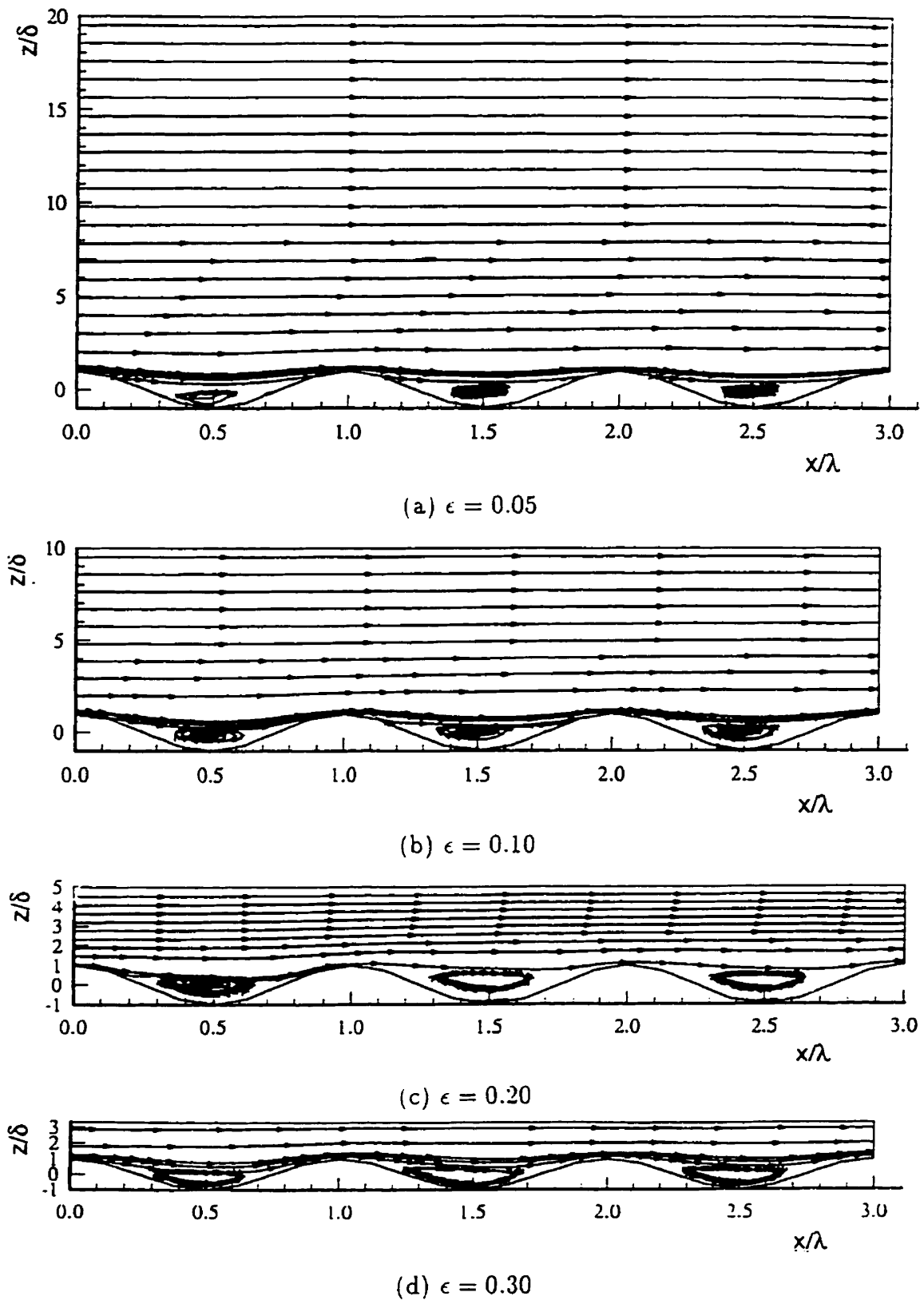


Figure 5.4: Influence of relative roughness ϵ on streamlines; $Re^* = 1.0$, $\gamma = 0.3$

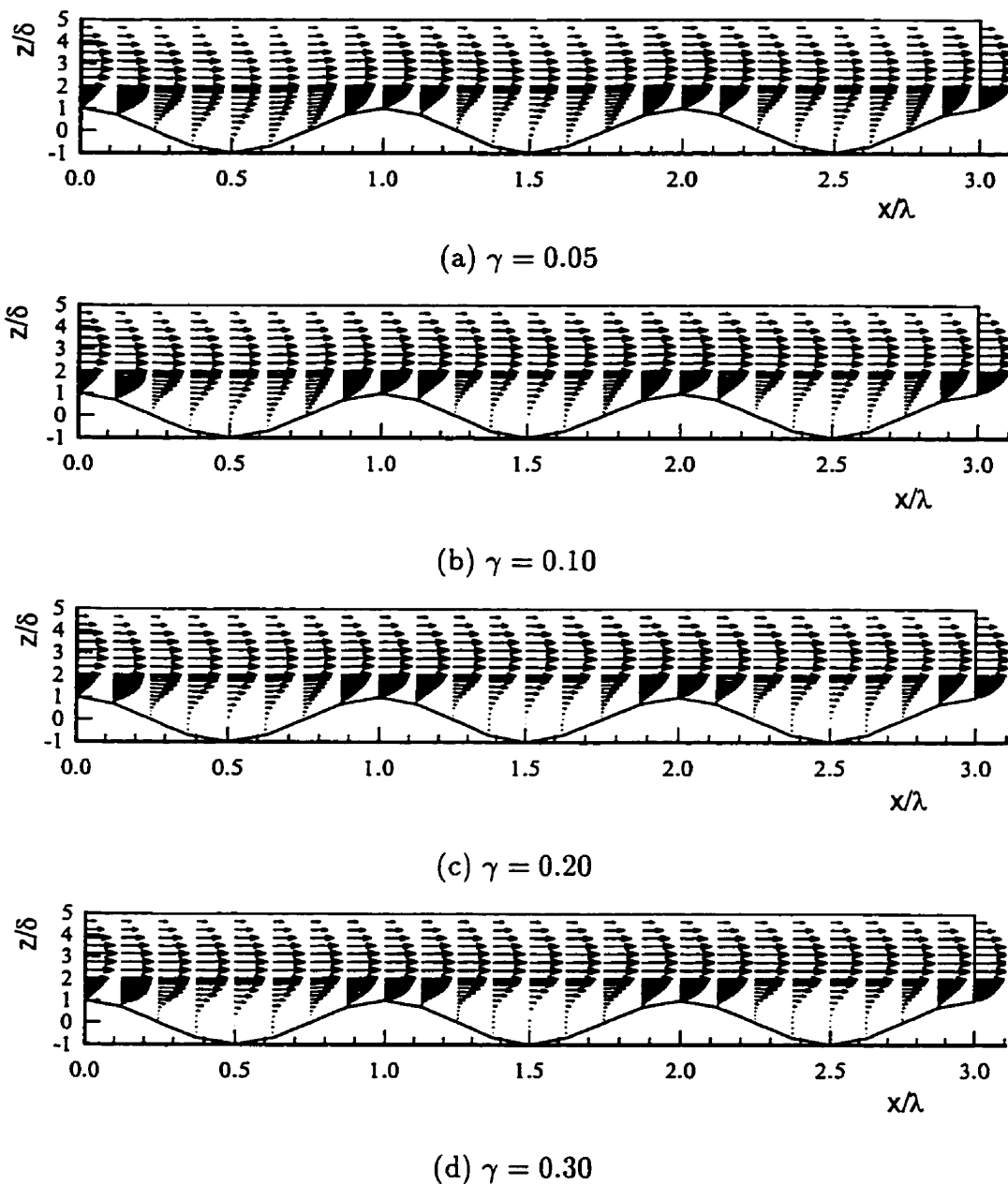


Figure 5.5: Influence of steepness γ on distribution of u/U ; $Re^* = 1.0$, $\epsilon = 0.2$

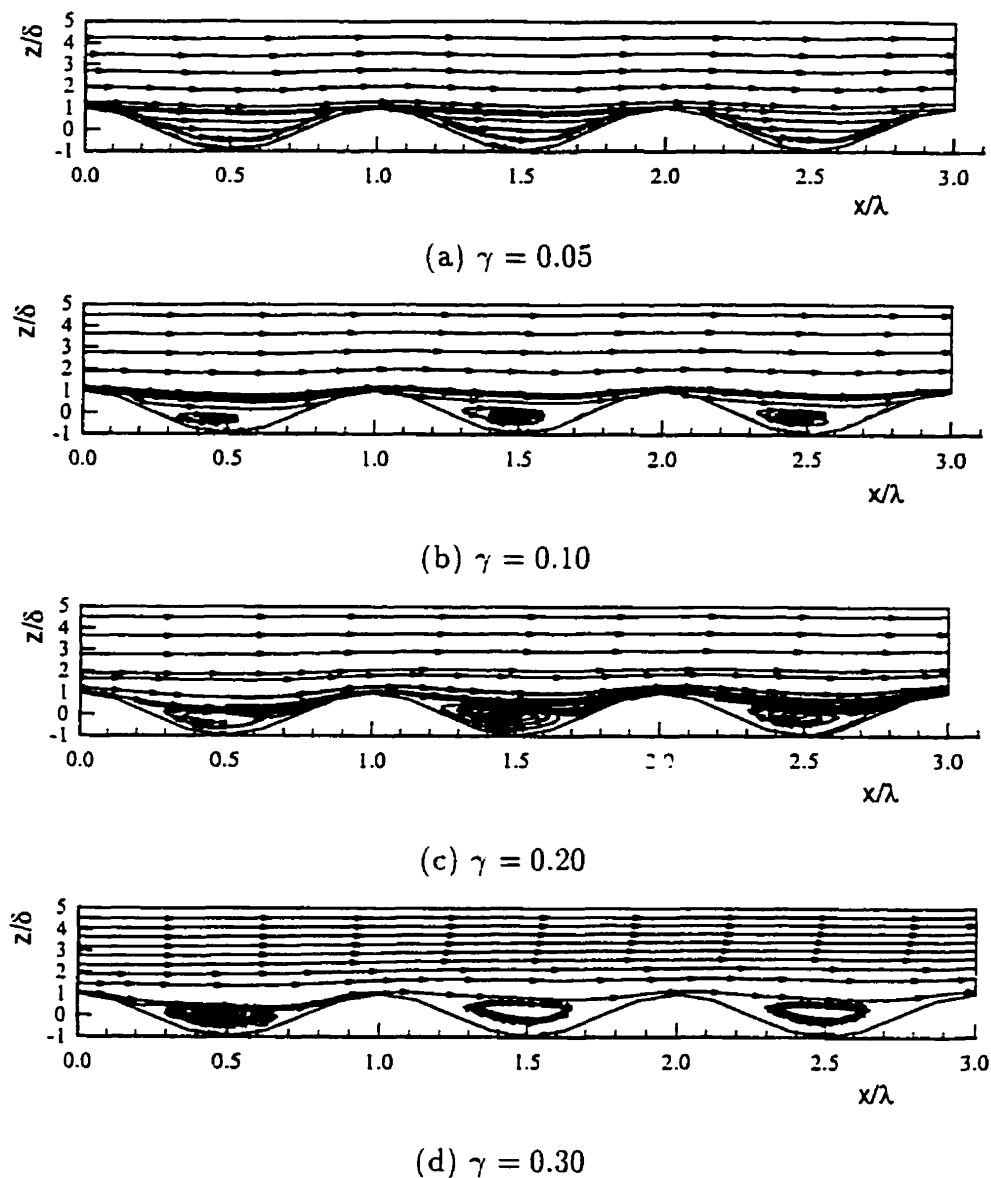


Figure 5.6: Influence of steepness γ on streamlines; $Re^* = 1.0$, $\epsilon = 0.2$

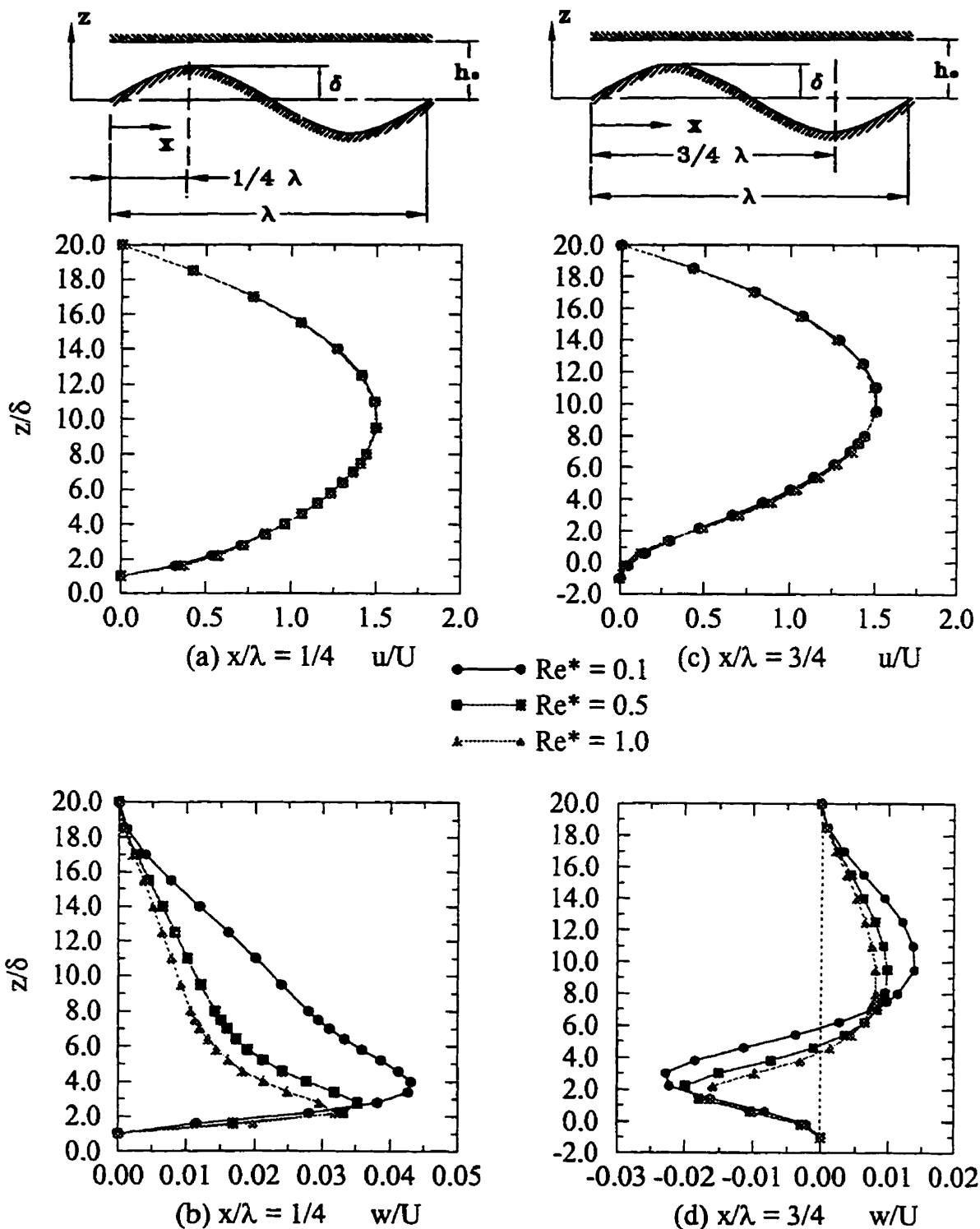


Figure 5.7: Velocity profiles at max/min channel stations, for various reduced Reynolds numbers Re^* , $\epsilon = 0.05$, and $\gamma = 0.1$

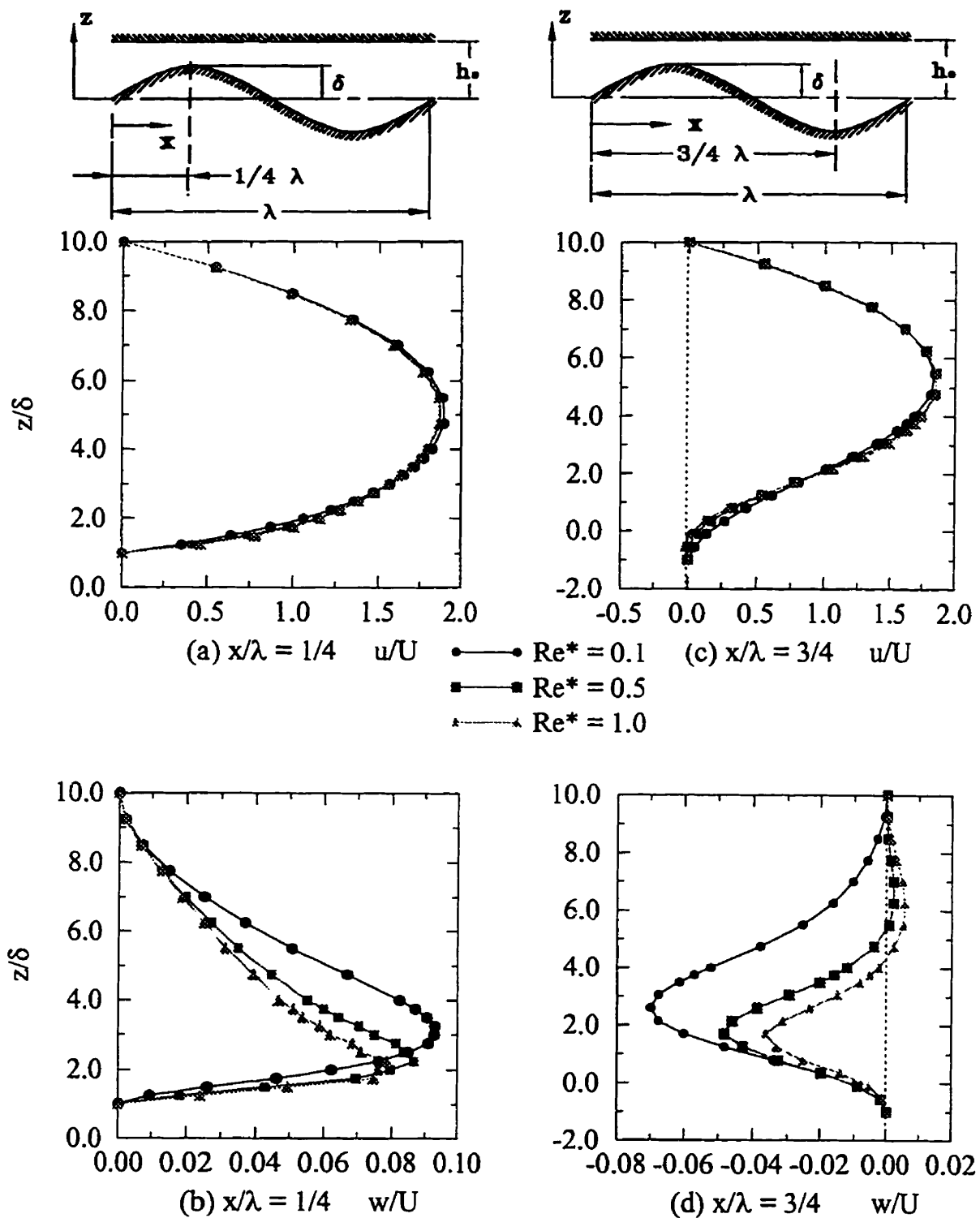


Figure 5.8: Velocity profiles at max/min channel stations, for various reduced Reynolds numbers Re^* , $\epsilon = 0.1$, and $\gamma = 0.1$

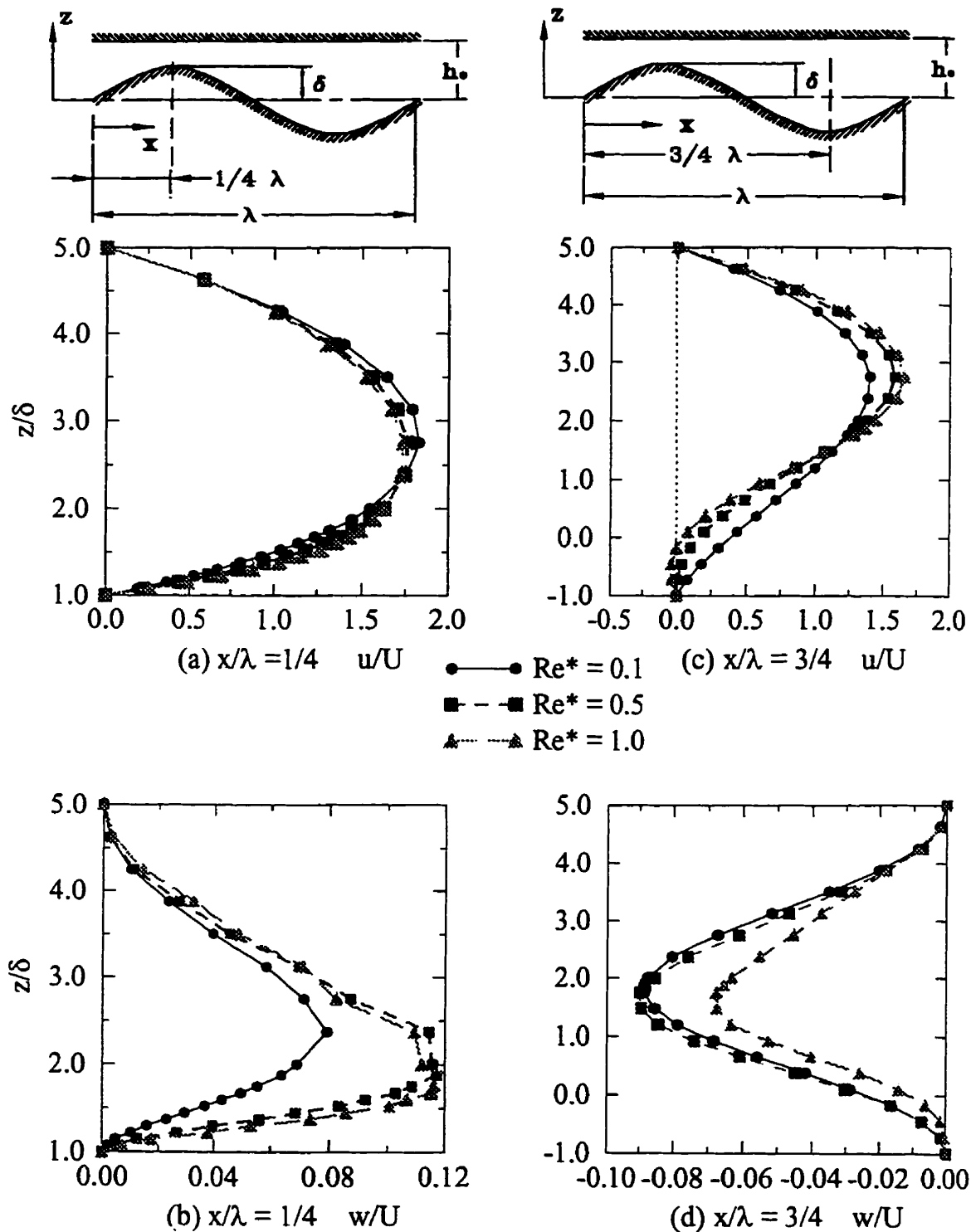


Figure 5.9: Velocity profiles at max/min channel stations, for various reduced Reynolds numbers Re^* , $\epsilon = 0.2$, and $\gamma = 0.1$

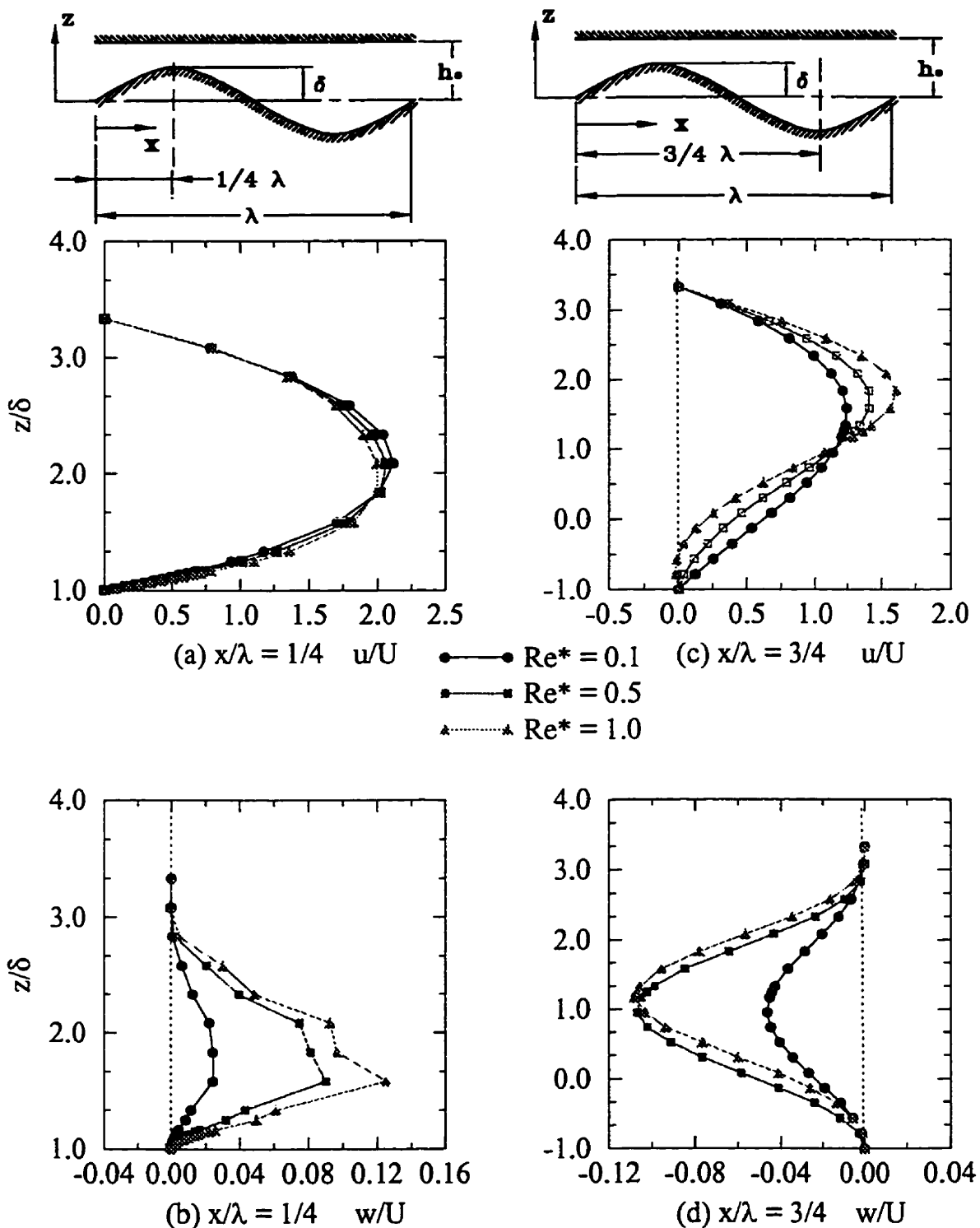


Figure 5.10: Velocity profiles at max/min channel stations, for various reduced Reynolds numbers Re^* , $\epsilon = 0.3$, and $\gamma = 0.1$

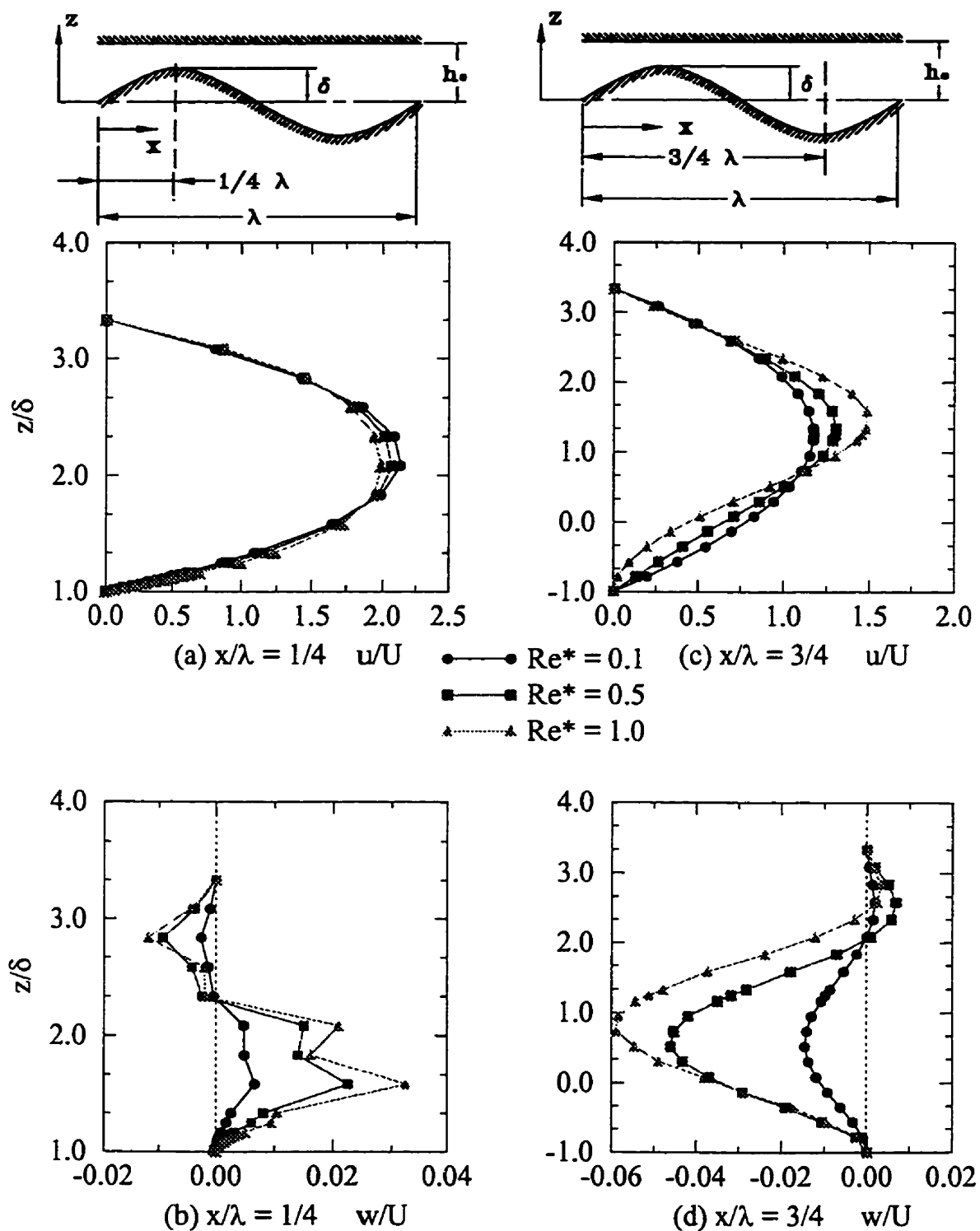


Figure 5.11: Velocity profiles at max/min channel stations, for various reduced Reynolds numbers Re^* , $\epsilon = 0.3$, and $\gamma = 0.05$

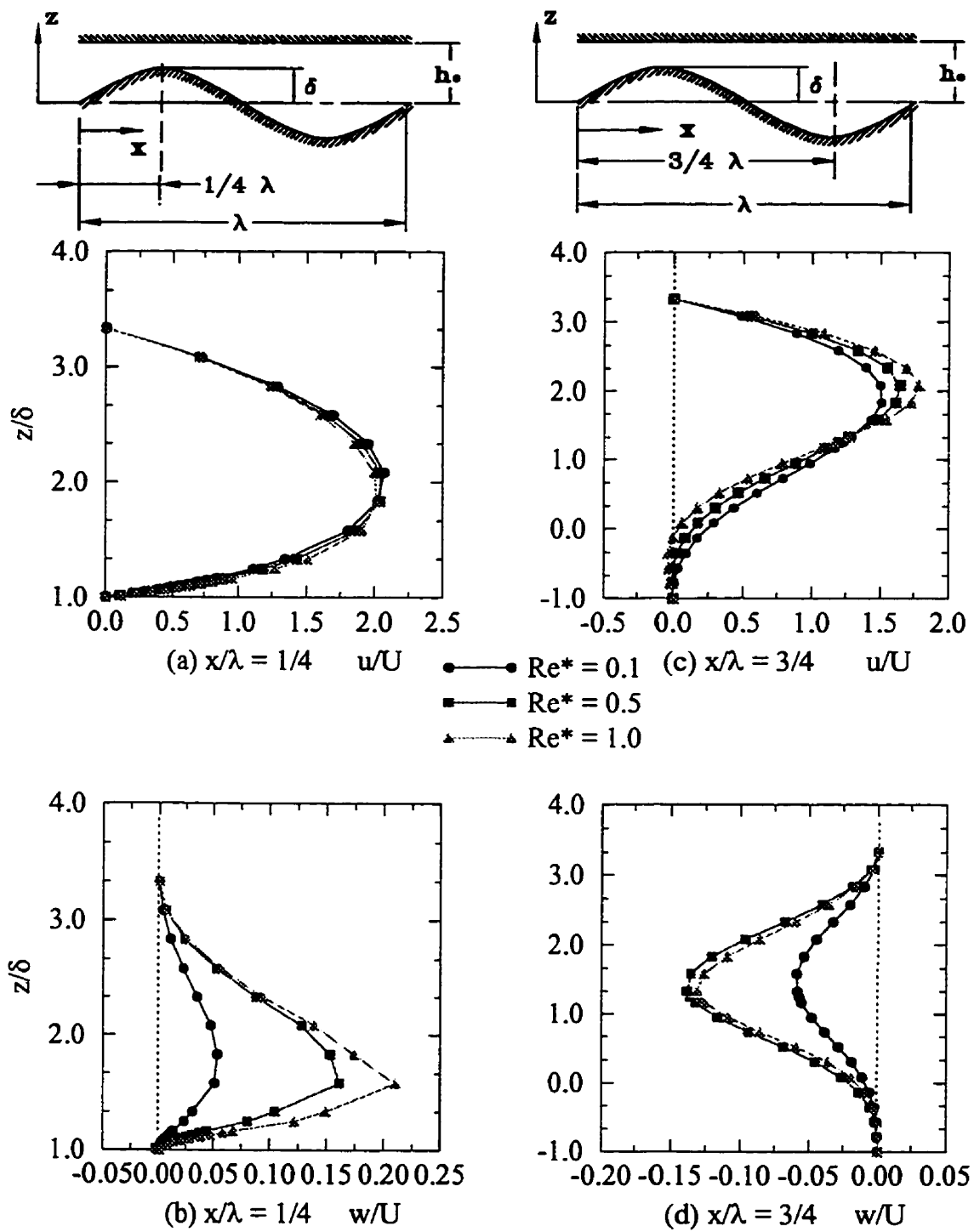


Figure 5.12: Velocity profiles at max/min channel stations, for various reduced Reynolds numbers Re^* , $\epsilon = 0.3$, and $\gamma = 0.2$

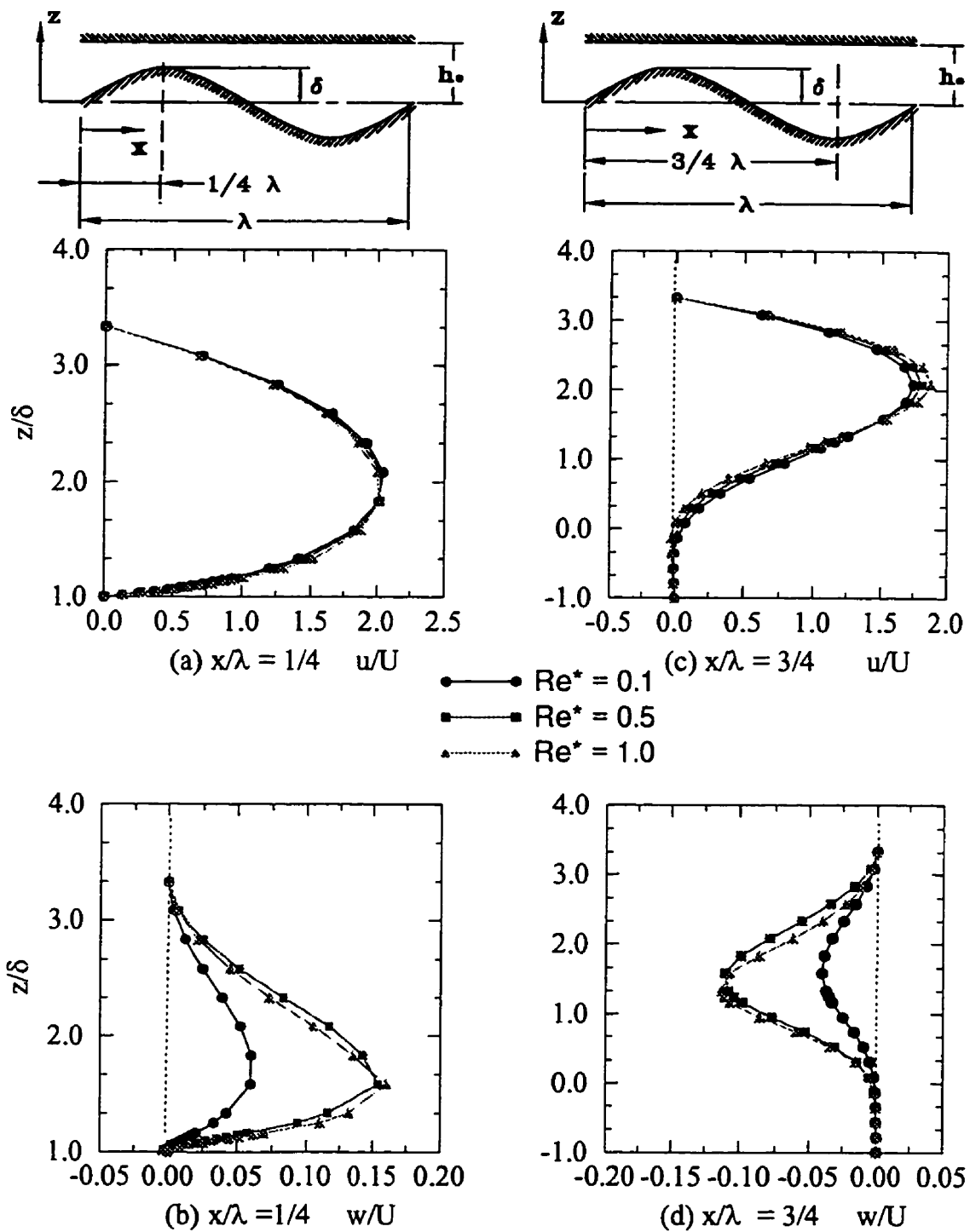


Figure 5.13: Velocity profiles at max/min channel stations, for various reduced Reynolds numbers Re^* , $\epsilon = 0.3$, and $\gamma = 0.3$

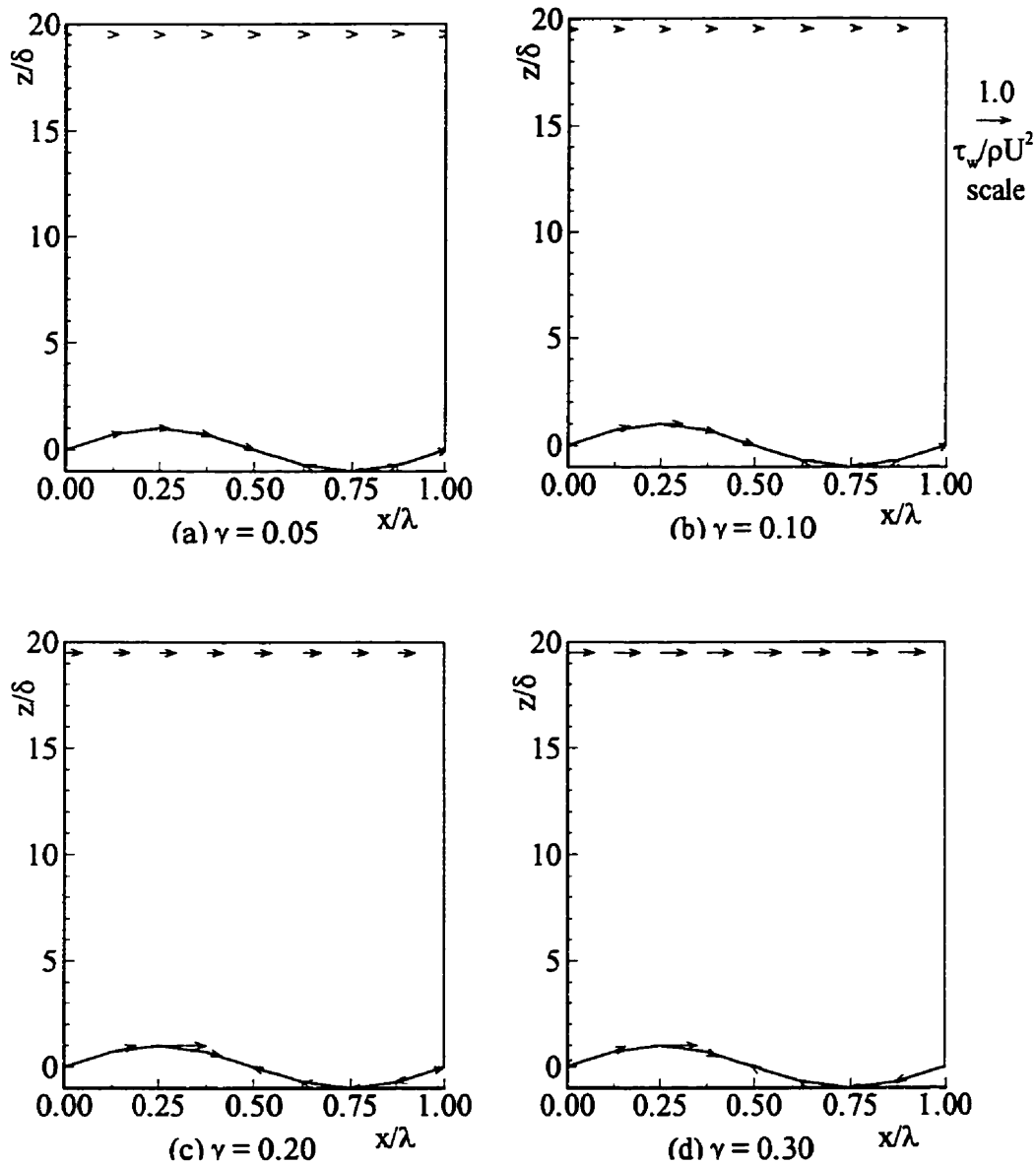


Figure 5.14: Local shear stress over one wavelength at various steepness (a) $\gamma = 0.05$; (b) $\gamma = 0.10$, (c) $\gamma = 0.20$, (d) $\gamma = 0.30$; for $\epsilon = 0.05$, and $Re^* = 1.0$

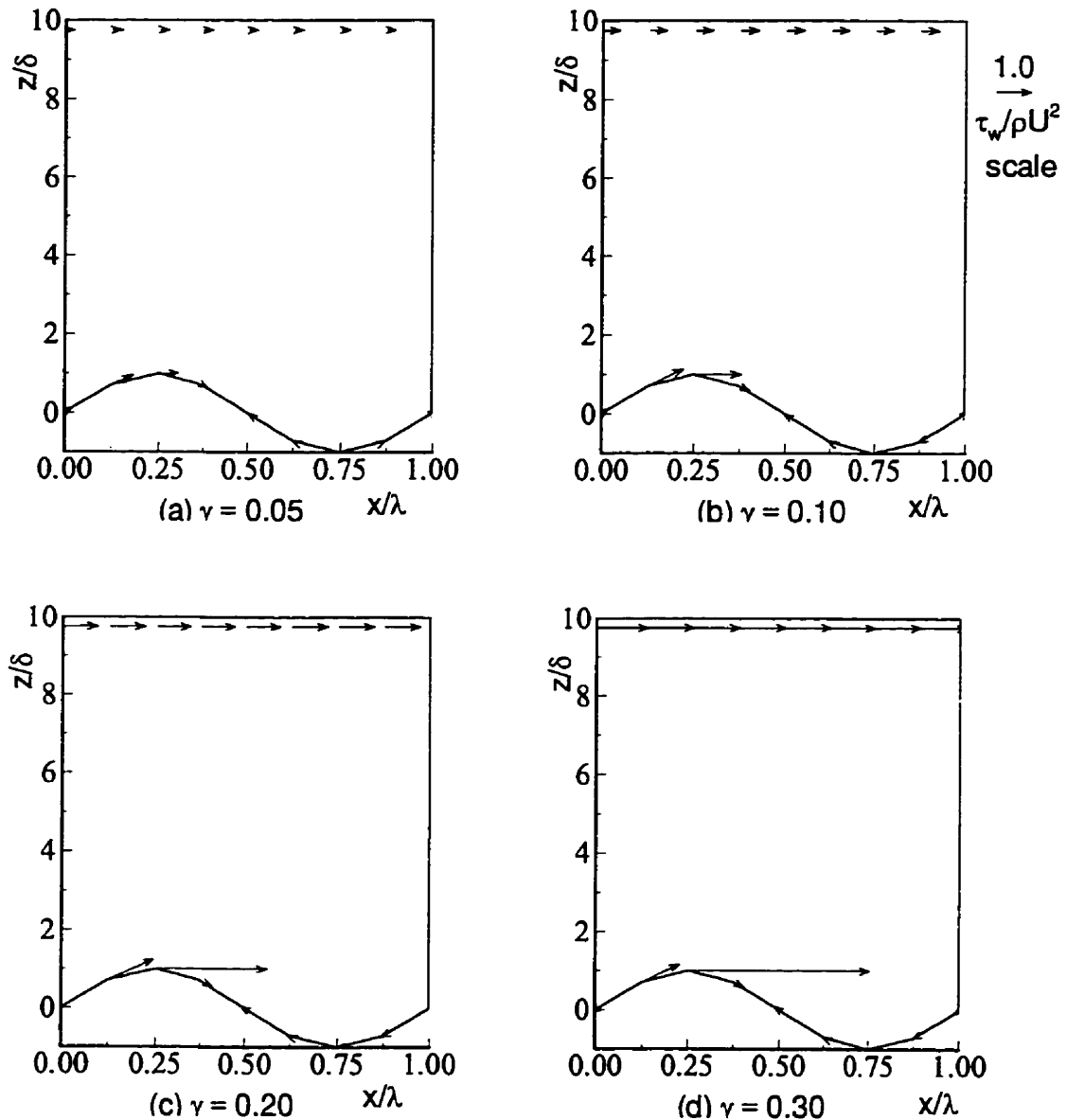


Figure 5.15: Local shear stress over one wavelength at various steepness (a) $\gamma = 0.05$; (b) $\gamma = 0.10$, (c) $\gamma = 0.20$, (d) $\gamma = 0.30$; for $\epsilon = 0.10$, and $Re^* = 1.0$

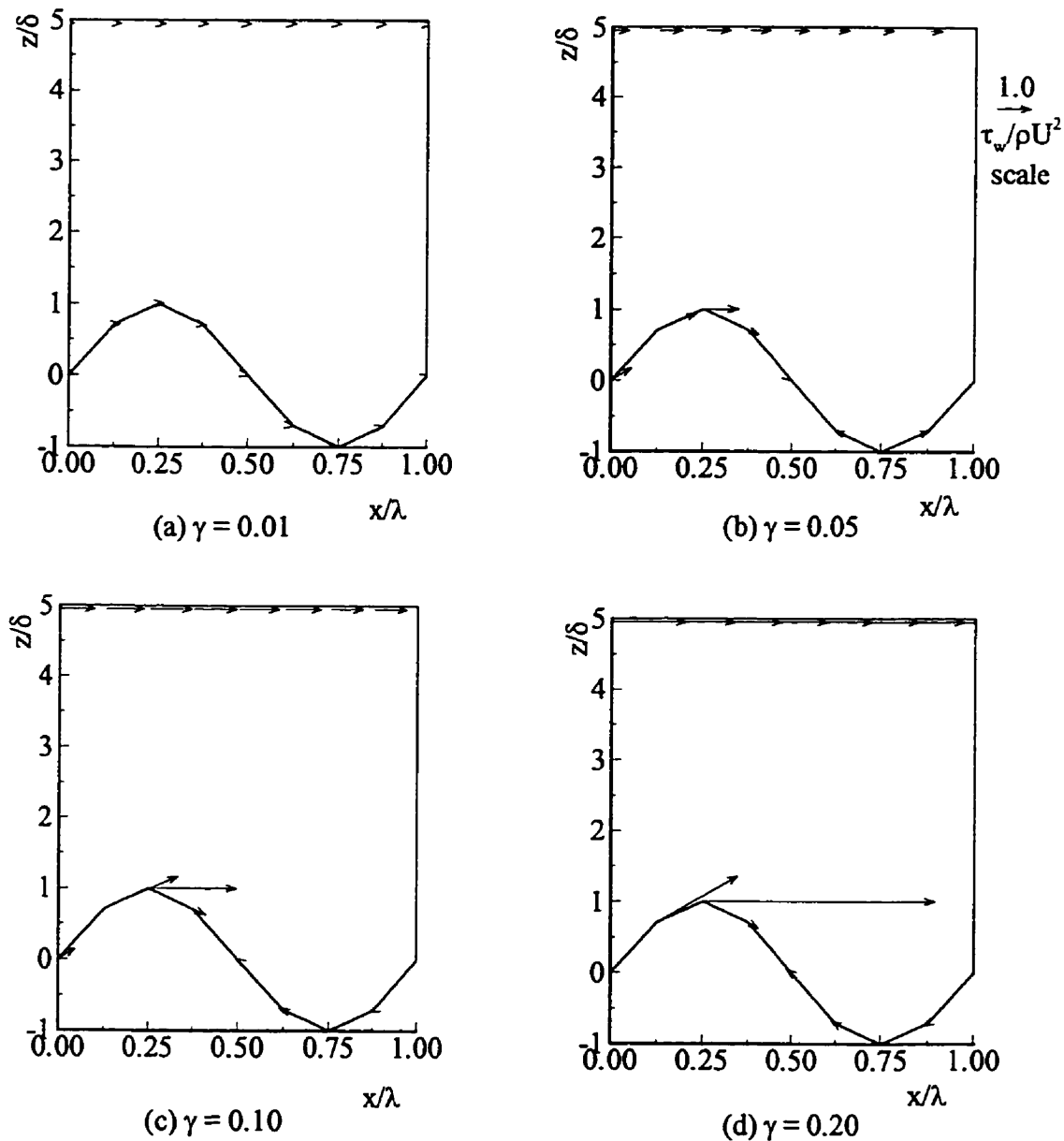


Figure 5.16: Local shear stress over one wavelength at various steepness (a) $\gamma = 0.05$; (b) $\gamma = 0.10$, (c) $\gamma = 0.20$, (d) $\gamma = 0.30$; for $\epsilon = 0.20$, and $Re^* = 1.0$

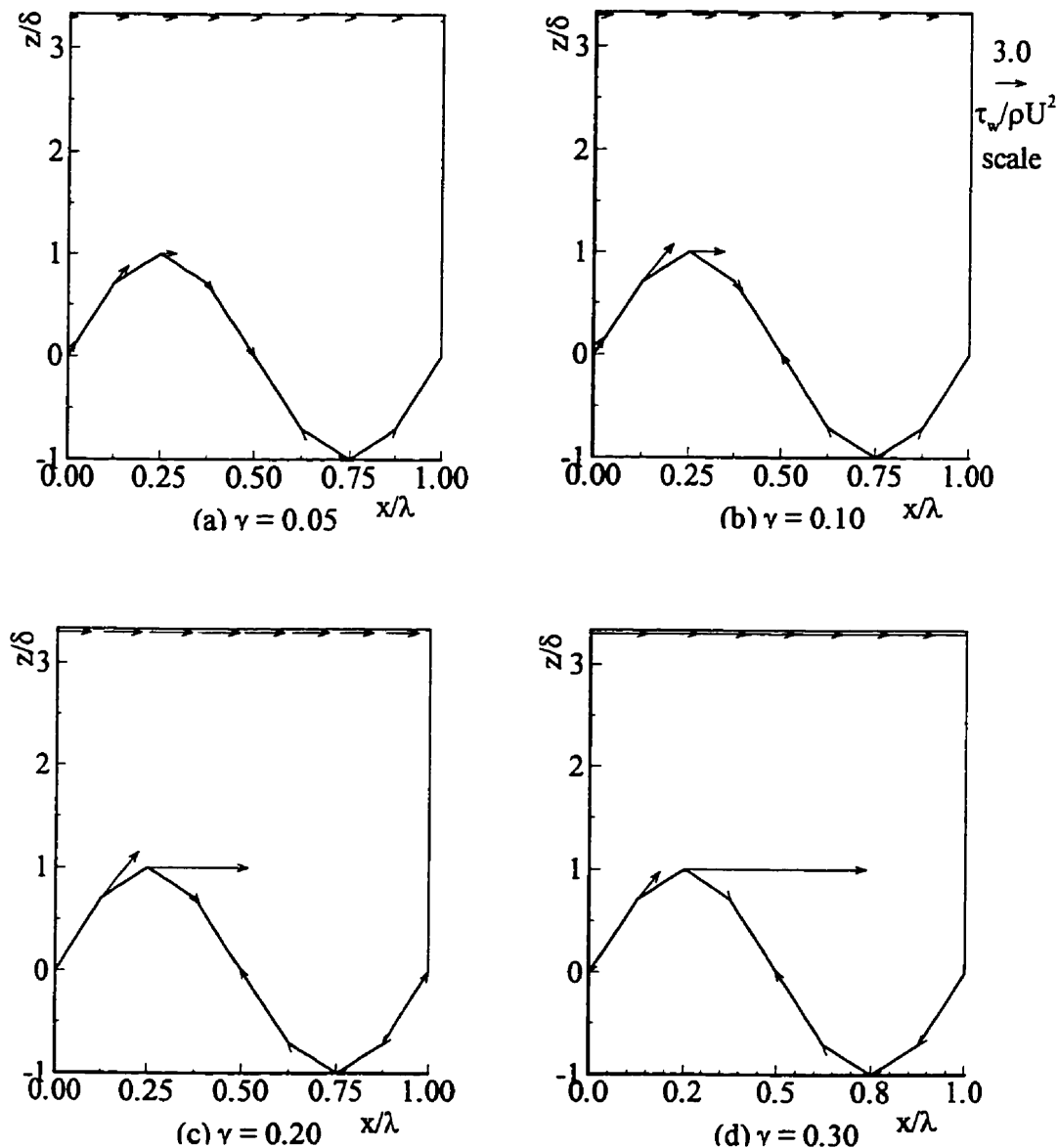


Figure 5.17: Local shear stress over one wavelength at various steepness (a) $\gamma = 0.05$; (b) $\gamma = 0.10$, (c) $\gamma = 0.20$, (d) $\gamma = 0.30$; for $\epsilon = 0.30$, and $Re^* = 1.0$

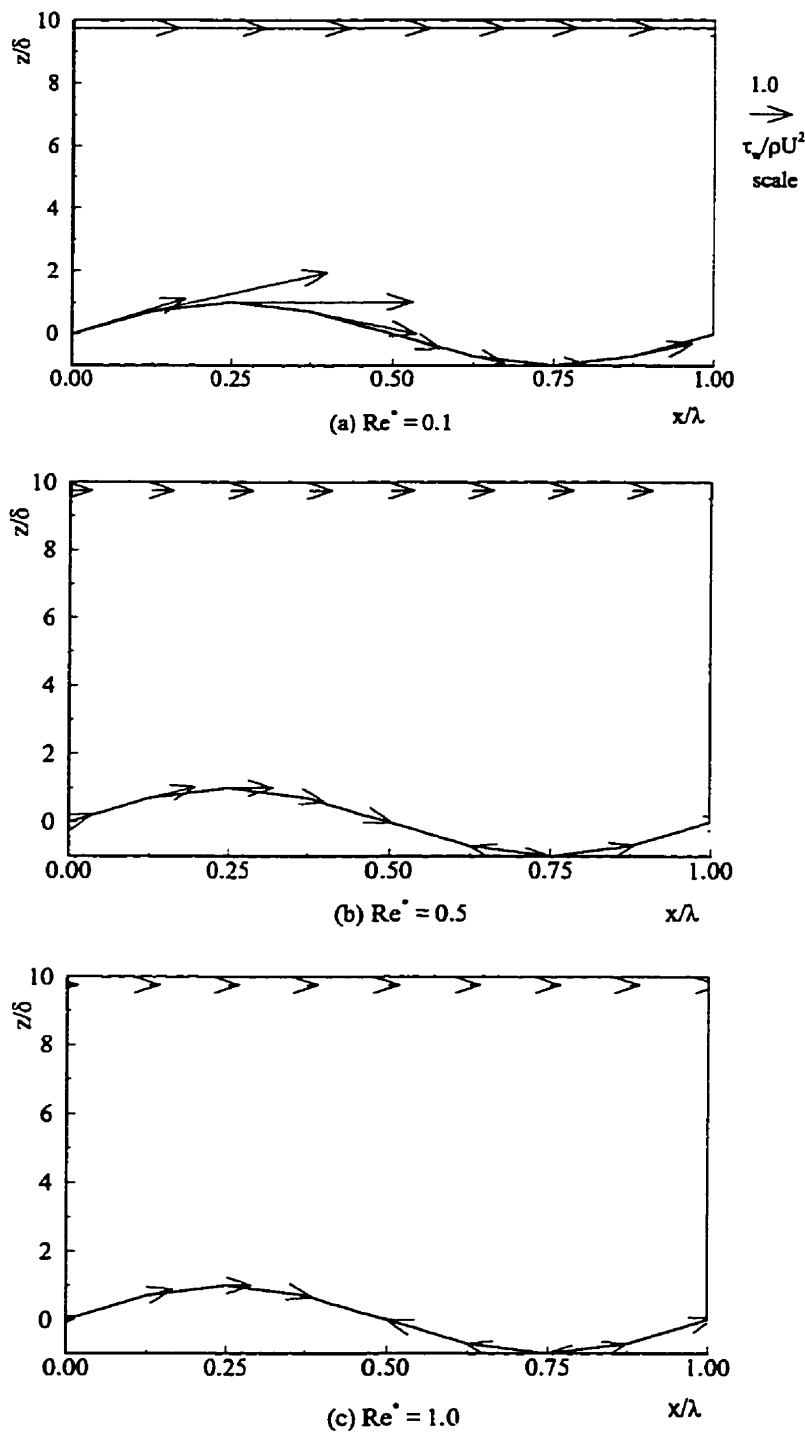


Figure 5.18: Local shear stress over one wavelength at various reduced Reynolds number
(a) $Re^* = 0.1$; (b) $Re^* = 0.5$, (c) $Re^* = 1.0$, for $\epsilon = 0.1$, and $\gamma = 0.1$

5.2 Comprehensive quantification of findings

While the above results show the detailed influence of key parameters, such as Re^* , ϵ , and γ on velocity, streamline and shear stress, the associated global energy loss is a comprehensive index which may be used to quantify the laminar sheet flow under consideration. The idea is borrowed from the energy analysis of one-dimensional flow. It is applied to the current flow situation subject to appropriate modifications.

Neglecting gravity the one-dimensional energy equation for the steady, fully developed flow of a real incompressible fluid in a straight, very wide duct (Fig. 5.19) reduces to

$$\frac{\bar{p}_1}{\rho} - \frac{\bar{p}_2}{\rho} = f \frac{\Delta L}{2h_0} \frac{U^2}{2} \quad (5.2)$$

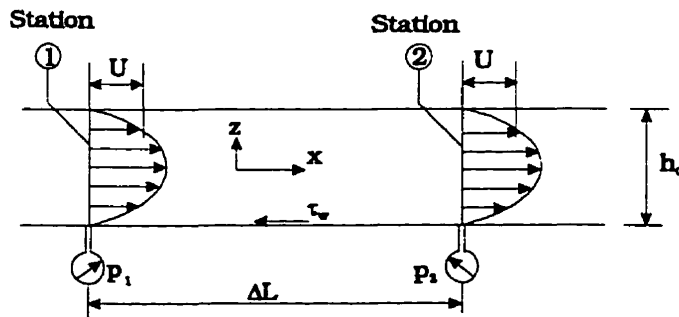


Figure 5.19: Fully developed flow in duct of constant cross section

In this equation, f is the Darcy-Weisbach friction factor (Gerhart and Gross, 1985), defined by Eq. (3.21) and here for convenience reproduced, viz.

$$f = 8 \frac{\tau_w}{\rho U^2} \quad (5.3)$$

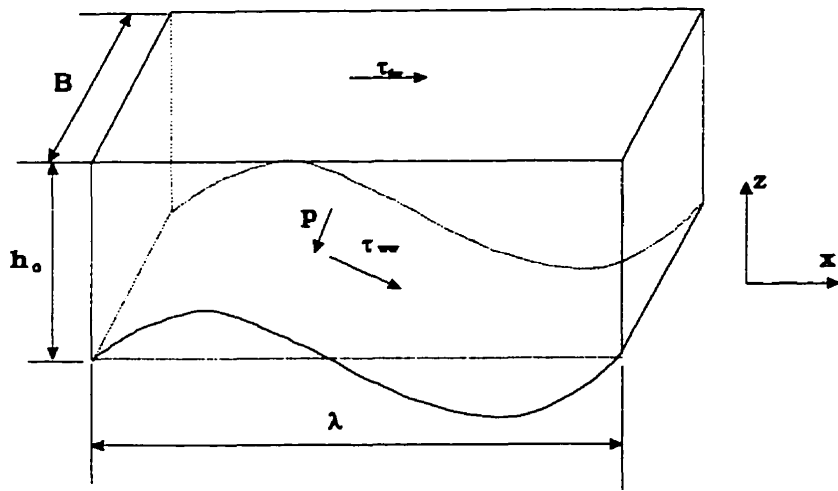


Figure 5.20: Fully developed flow in a rectangular duct between a flat wall and a sinusoidally wavy wall over one wave length

and \bar{p} denotes the average pressure over the cross section. When combined Eqs. (5.2) and (5.3) assume the form of the corresponding x -component of the one-dimensional momentum equation, viz.

$$\frac{\bar{p}_1 - \bar{p}_2}{\rho} = 2 \frac{\tau_w}{\rho} \frac{\Delta L}{h_0} \quad (5.4)$$

which illustrates the balance between pressure and shear forces for straight walls.

For the relevant case of flow in a wide duct ($h_0/B \rightarrow 0$) with a flat wall and wavy wall shown in Fig. 5.20, Eqs. (5.2) and (5.4) hold true for any whole periodic length of the conduit. However, the right hand side of the equations must be modified to account for the presence of both shear stress and wall pressure along the sinusoidally wavy boundary. Thus, the pressure drop is now:

$$\bar{p}_1 - \bar{p}_2 = \frac{1}{A} \left[\int_{A_{ww}} (\tau_{ww,x} + p_x) dA + \int_{A_{fw}} \tau_{fw,x} dA \right] \quad (5.5)$$

where A is the area of the duct cross section at stations 1 and 2.²

$$A = h_0 B \quad (5.6)$$

and

$$\int_{A_{fw}} \tau_{fw,x} dA = \lambda B \bar{\tau}_{fw,x} \quad (5.7)$$

$$\int_{A_{ww}} \tau_{ww,x} dA = \bar{\tau}_{ww,x} \int_{A_{ww}} dA \quad (5.8)$$

$$\int_{A_{ww}} p_x dA = \bar{p}_{ww,x} \int_{A_{ww}} dA \quad (5.9)$$

In terms of (5.6) through (5.9), Eq. (5.5), and introducing the parameters, ϵ and γ , results in

$$\bar{p}_1 - \bar{p}_2 = \frac{\epsilon}{\gamma} [\bar{\tau}_{fw} + \frac{\alpha_s}{2\pi} (\bar{\tau}_{ww,x} + \bar{p}_{ww,x})] \quad (5.10)$$

where α_s is related to the wavy surface and follows from its integration. Thus, with $h(x) = \delta \sin(2\pi x/\lambda)$, and for $B = \text{constant}$, the surface area becomes

²ww = wavy wall, fw = flat wall

$$S_{2\pi} = \int_0^{2\pi} \sqrt{1 + \left[\frac{dh(x)}{dx}\right]^2} dx \quad (5.11)$$

whence

$$\alpha_s = \int_0^{2\pi} \sqrt{1 + (2\pi\gamma)^2 \cos^2(X)} dX \quad (5.12)$$

where $X = 2\pi x/\lambda$.

Calling the friction coefficient in the present case f^* , its magnitude emerges from Eq. (5.2) with $\Delta L = \lambda$, and $(\bar{p}_1/\rho - \bar{p}_2/\rho)$ from Eqs. (5.5) and (5.10) as

$$f^* = 4 \frac{1}{\rho U^2} [\bar{\tau}_{fw} + \frac{\alpha_s}{2\pi} (\bar{\tau}_{ww,x} + \bar{p}_{ww,x})] \quad (5.13)$$

Eq. (5.13) reduces to Eq. (5.3) for the case of a straight duct where $\epsilon = \gamma = 0$.

Employing the numerical results presented in Section 5.1, the variation of the friction coefficient f^* with Reynolds number Re as functions of relative roughness and steepness are displayed in Figs. 5.21 and 5.22.³ In Fig. 5.21, the friction coefficient f^* increases with an increase of the relative roughness ϵ for two values of steepness, viz. $\gamma = 0.05$ (a) and $\gamma = 0.10$ (b). The solid line in the diagrams is the friction coefficient for plane Poiseuille flow, i.e., $f = 96/Re$. In Fig. 5.22, the friction coefficient f^* increases with increasing steepness γ for two values of relative roughness ϵ .

The phenomena reflected in the diagrams of Figs. 5.21 and 5.22 can be understood by

³For the sake of maintaining convention the bulk Reynolds number Re is used here instead of Re^* .

considering the composition of the reduced Reynolds number, i.e., Eq. (5.1). Thus, for the same bulk Reynolds number Re and constant relative roughness ϵ , an increasing steepness γ will result in an increase of the reduced Reynolds number Re^* . The same will happen with increasing relative roughness at fixed steepness.

Comparable effects of the geometry on laminar flow through tubes with sinusoidal axial variations in diameter, and with periodic step changes in diameter were noted by, respectively, Deiber and Schowalter (1979) and Azzam and Dullien (1977). Of more relevant interest is the numerical work on ripples performed at the Iowa Institute of Hydraulic Research (Patel et al., 1991). It involves laminar flow between a flat wall and a wavy surface composed of a finite wave train of six sinusoids. Expressed in terms of the present nomenclature, a typical finding of the Iowa-group for $Re = 21,520$ ($Re = Uh_0/\nu = 10,760$ in the paper(Patel et al., 1991)), $\epsilon = 0.11$, $\gamma = 0.10$ yields a friction coefficient $f^* = 0.0254$. The corresponding extrapolated result for the model developed in this thesis is $f^* = 0.0250$. These two results are very close to each other, and this finding strongly supports the analytical/numerical method used herein.

Recently, Russ and Beer (1997a, 1997b) investigated heat transfer and flow in a pipe with a sinusoidally wavy surface of limited longitudinal extent. Their principle parameters are identical to those used in the present study. However, the results presented do not provide relevant conclusive experimental data on friction coefficients in laminar flow.

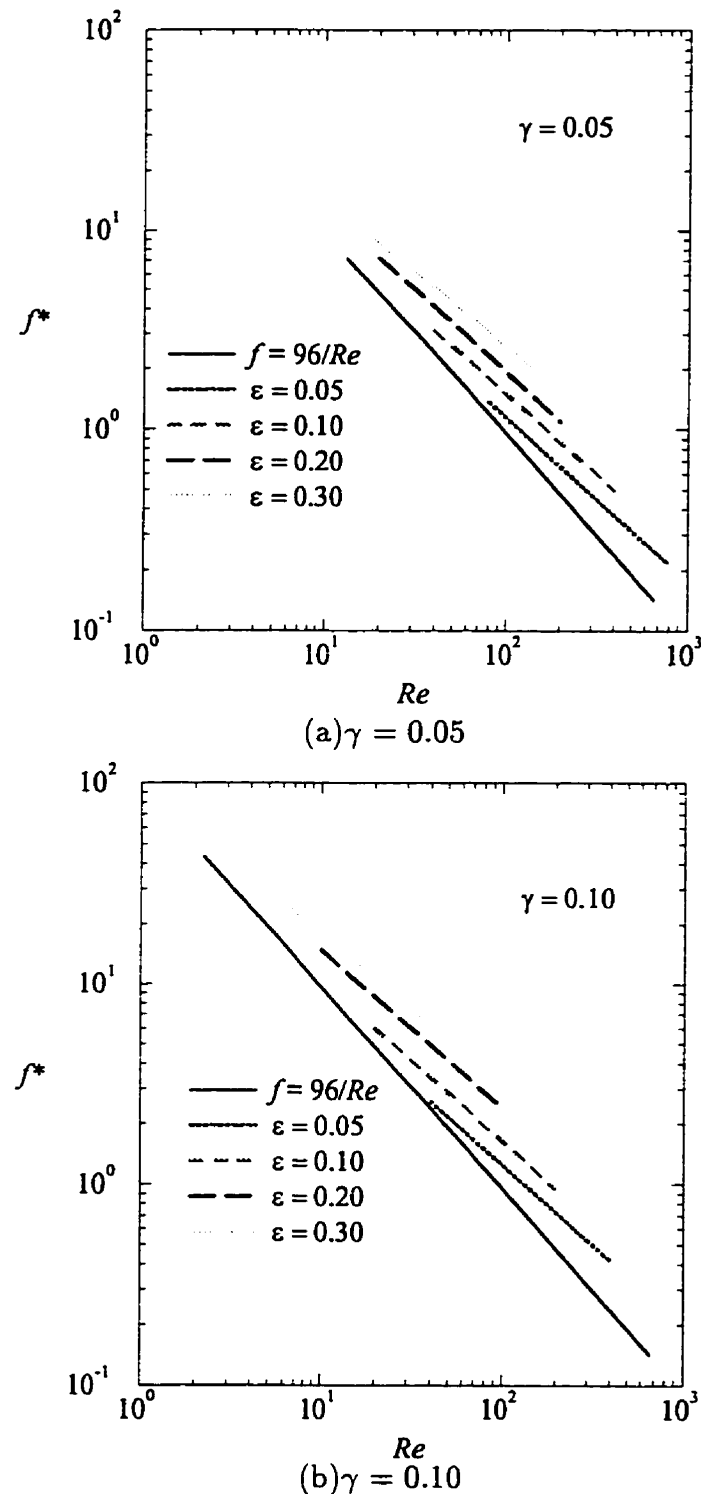


Figure 5.21: Friction coefficient f^* vs. Reynolds number Re as a function of relative roughness ϵ , with steepness γ as parameter

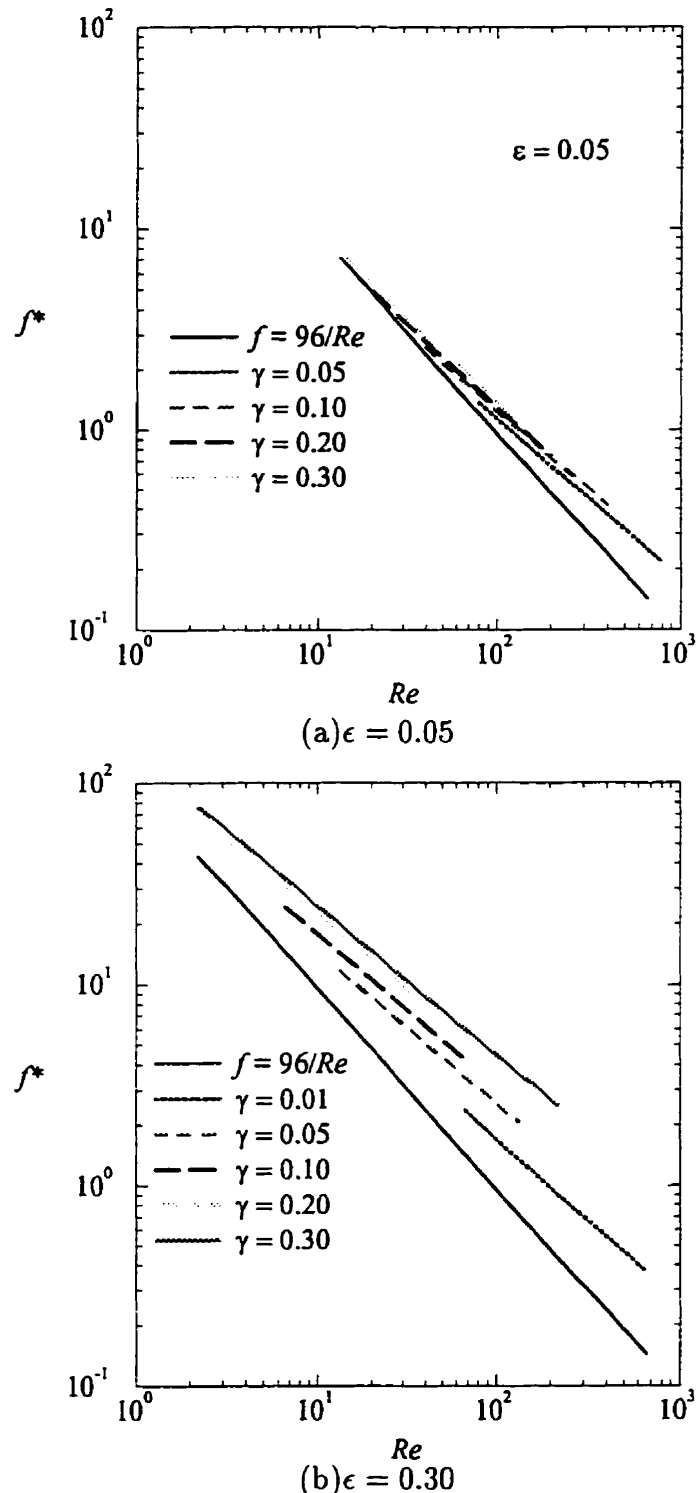


Figure 5.22: Friction coefficient f^* vs. Reynolds number Re as a function of relative roughness ϵ , with steepness γ as parameter

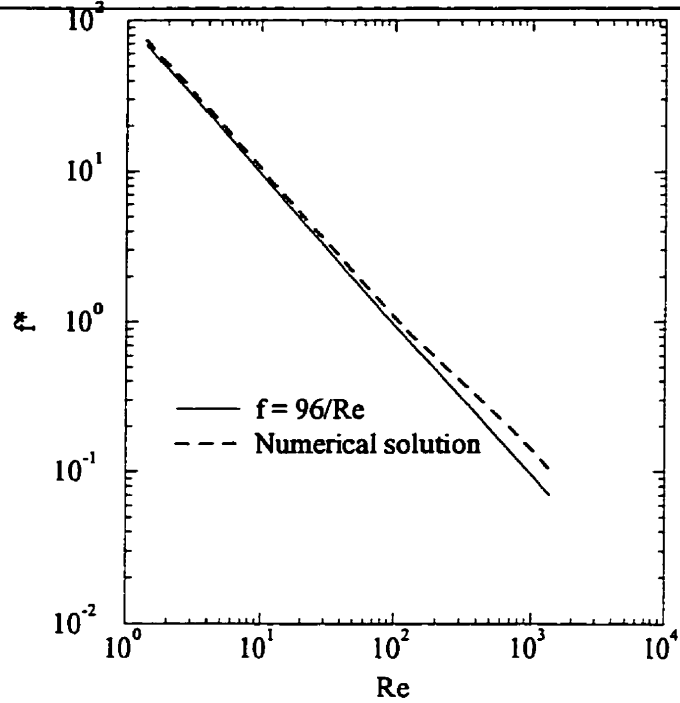


Figure 5.23: Friction coefficient f^* vs. Reynolds number Re ; relative roughness $\epsilon = 0.12$ and steepness $\gamma = 0.012$

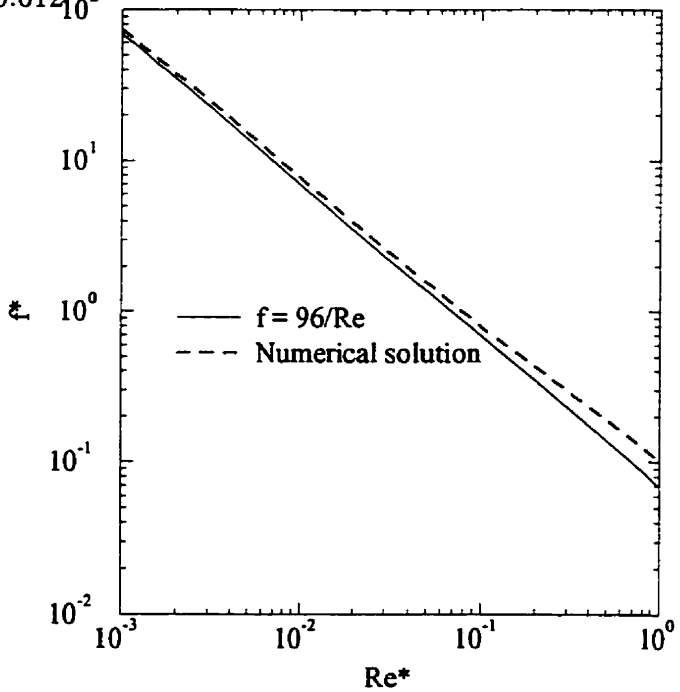


Figure 5.24: Friction coefficient f^* vs. reduced Reynolds number Re^* ; relative roughness $\epsilon = 0.12$ and steepness $\gamma = 0.012$

Extensive calculations with various sets of relative roughness ϵ and steepness γ were carried out in order to establish a reasonably precise threshold of applicability of the classic Reynolds equation for the situation of unilateral, sinusoidally wavy wall. This matter is addressed in Chapter Seven.

The diagrams of Figs. 5.21 and 5.22 are complemented by the corresponding information for the case of the physical model (see Chapter Four) with $h_0 = 25$ mm, $\delta = 3$ mm, $\lambda = 250$ mm, whence $\epsilon = 0.12$ and $\gamma = 0.012$. In particular, Fig. 5.23 shows the variation of f^* over the range of bulk Reynolds number $10^0 < Re < 10^3$, while in Fig. 5.24 f^* is plotted as a function of the reduced Reynolds number Re^* . The two diagrams are equivalent, of course, since, with fixed values of ϵ and γ , Re and Re^* are proportional to each other according to Eq. (5.1). However, they show, again, the monotonically increasing effects of micro-inertia on f^* with increasing reduced Reynolds number Re^* . In the present case, for instance, f^* exceeds the plane-Poiseuille value by more than 10% for $Re^* > 10^{-2}$ (or $Re \geq 15$).

5.3 Experimental observations

Fig. 5.25 shows typical streakline profiles, made visible by the smoke-wire technique, for flow past the sinusoidally wavy wall of the apparatus described in Chapter Four. The time difference between the three exposures is $1/30$ of a second. The corresponding velocity profile follows from the distance traveled by the smoke particles between two exposures and the intervening time period.

Video images of smoke-wire streaklines at different streamwise positions along the duct are displayed in Fig. 5.26. These profiles were recorded at a setting of $h_0 = 15$ mm and $U = 0.45$ m/s, equivalent to $Re^* = 1.07$, $\epsilon = 0.2$, $\delta = 3$ mm, $\lambda = 250$ mm, and $Re = 894$. The corresponding velocity vector plots, obtained from both hot-wire anemometer measurements and the numerical results of FEM, are shown in Fig. 5.27. There is overall agreement between numerical and experimental results although heat convection effects may be noticed in Figs. 5.26(b) and 5.26(d) due to the relatively small velocity at the bottom of these two positions.

Figs. 5.28 to 5.31 give more detailed comparisons between experimental data obtained by hot-wire anemometry and numerical solutions acquired by the finite element method. For various channel heights h_0 (corresponding to various values of ϵ), these quantitative plots demonstrate very good agreement with each other. Clearly, the experimental apparatus has reached its design goal by providing a variety of measurable conditions. For instance, the reduced Reynolds number Re^* can be anywhere between 0.1 and 1.5 for

various channel heights h_0 .

Figs. 5.28 and 5.29 correspond to two values of the reduced Reynolds number for the same geometrical set, i.e., the same values of ϵ and γ . The significant difference between the two sets of diagrams is the clear trend towards flow reversal in the vicinity of the wavy wall at stations $x/\lambda = 1/2$ and $3/4$ (i.e., in the “cavity” region) for the case with the greater Re^* (Fig. 5.29). Finally, Figs. 5.30 and 5.31 are additional demonstrations of the good agreement between experiment and analysis with relative roughness $\epsilon = 0.15$ and 0.30 , respectively.

The effects of relative roughness $\epsilon = \delta/h_0$ on streamline pattern is shown in the photographs of Fig. 5.32. For the fixed dimensions of the sinusoidally wavy surface, the steepness is constant at $\gamma = \delta/\lambda = 3 \text{ mm} / 250 \text{ mm} = 0.012$. The reduced Reynolds number is about unity, while the channel height h_0 varies from 10 mm to 20 mm . The increasing relative roughness increases the curve portion of the streamline in the cross section.

The streamlines in the converging and diverging areas for the case of $h_0 = 20 \text{ mm}$ are given in Fig. 5.33 (a) and (b).⁴

Fig. 5.33(c) illustrates the effect of heat convection occurring at lower values of the reduced Reynolds number. The corresponding average velocity is 0.32 m/s , which is too low for proper flow visualization by the smoke wire technique.

Securing experimental evidence of separation and “cavity” circulation for the sinusoidally wavy wall proved not to be possible. The reason for this becomes clear from the

⁴It should be pointed out that reflections on the wavy wall are also recorded in the photographs.

FEM solution for the highest practical $Re^* = 2.25$ (corresponding $Re = 3123 > 2000!$) for $\epsilon = 0.12$ ($h_0 = 25\text{mm}$) and $\gamma = 0.012$.

In summary, the numerical results of the solution of the Navier-Stokes equation for the case of a unilateral, sinusoidally wavy wall have been verified, both qualitatively and quantitatively, by corresponding experimental findings. In particular, the significance of the three parameters of, respectively, reduced Reynolds number Re^* , relative roughness ϵ and steepness γ have been clearly established, and the micro-inertia effects of surface roughness have been linked to the flow activities taking place in the “cavity” zones of the wall.

Various measures were taken to strengthen confidence in the findings. Thus, the global mass conservation needs to be checked for the numerical method to estimate the uncertainty of its result, since the Crouzeix-Raviart element complying with pressure penalty method provides only elemental mass conservation. Similarly, the experimental velocity findings were tested to ensure continuity.

For example, the experimental velocity profiles were integrated by applying Simpson's rule, and a quadratic Lagrange interpolation function was used to obtain the values at the designated even grid points.

As a typical example, for the case of $\epsilon = 0.2$, $\gamma = 0.012$, $Re^* = 1.07$, shown in Fig. 5.27, the uncertainty of the maximum value of the nine calculated flow rates is found to be less than 5% for the experimental results, and less than 0.65% for the numerical solution at all nine of the stations identified.

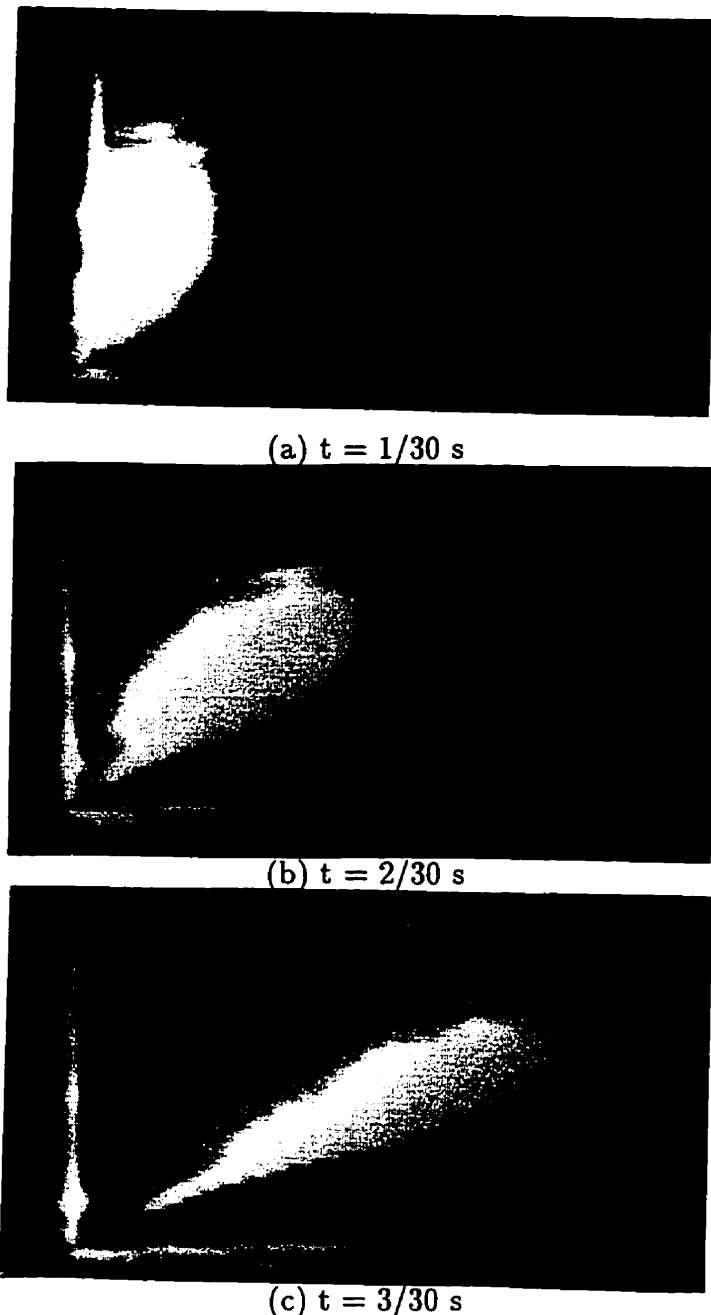


Figure 5.25: Evolution of streakline picture at position $x = \lambda$ of sinusoidally wavy wall; $Re^* = 1.07$, $\epsilon = 0.15$, and $\gamma = 0.012$

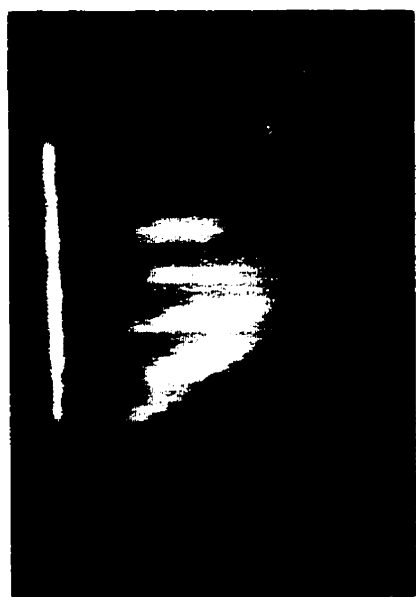
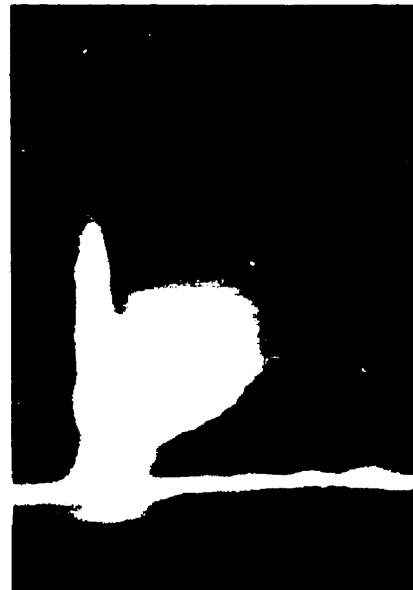
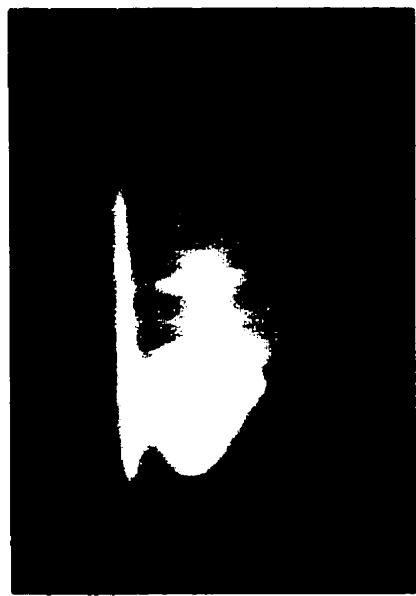
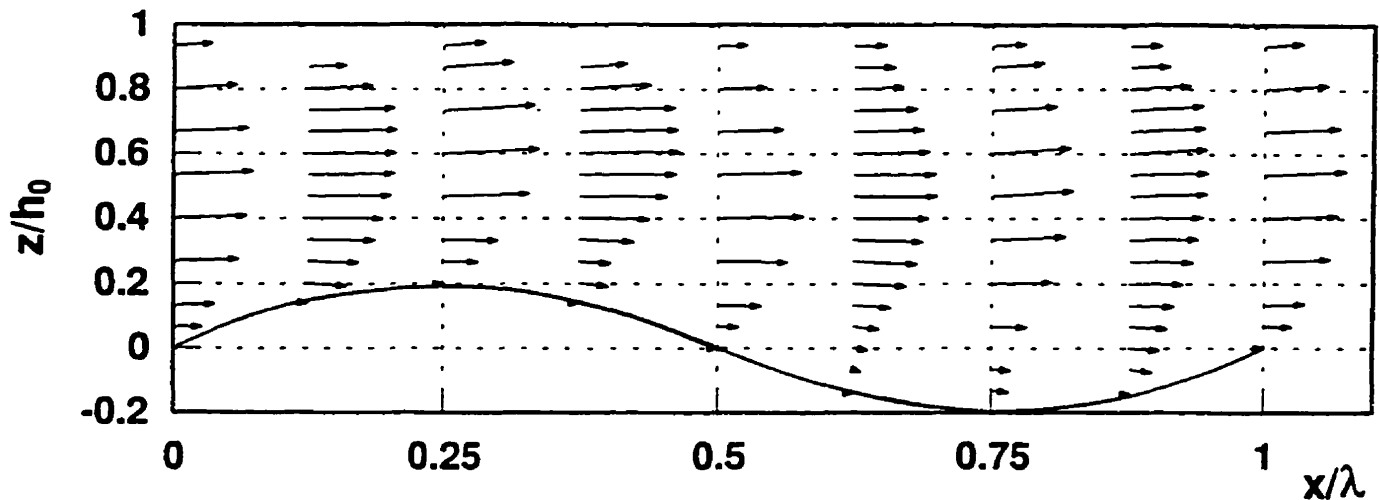
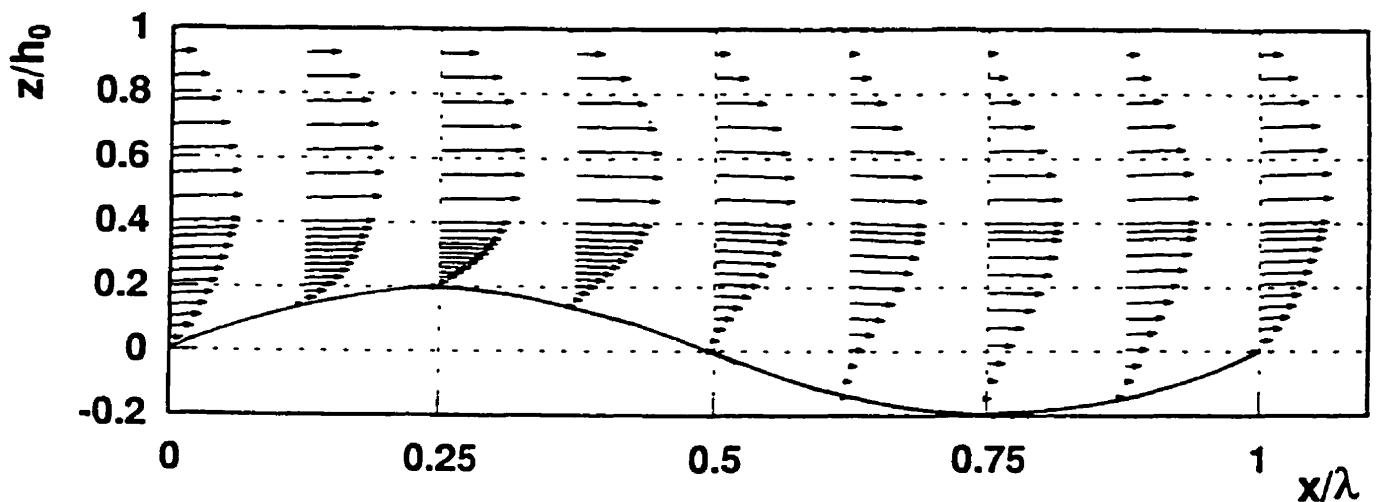
(a) $x = 0$ (b) $x = 1/4 \lambda$ (c) $x = 1/2 \lambda$ (d) $x = 3/4 \lambda$

Figure 5.26: Streakline pictures at various streamlinewise positions of sinusoidally wavy wall; $Re^* = 1.07$, $\epsilon = 0.2$, $\lambda = 0.012$



(a) Velocity vector obtained by hot-wire anemometer



(b) Velocity vector obtained by finite element method

Figure 5.27: Overall comparison of velocity vector plots between experimental measurement and numerical results for sinusoidally wavy wall; $Re^* = 1.07$, $\epsilon = 0.2$, $\gamma = 0.012$

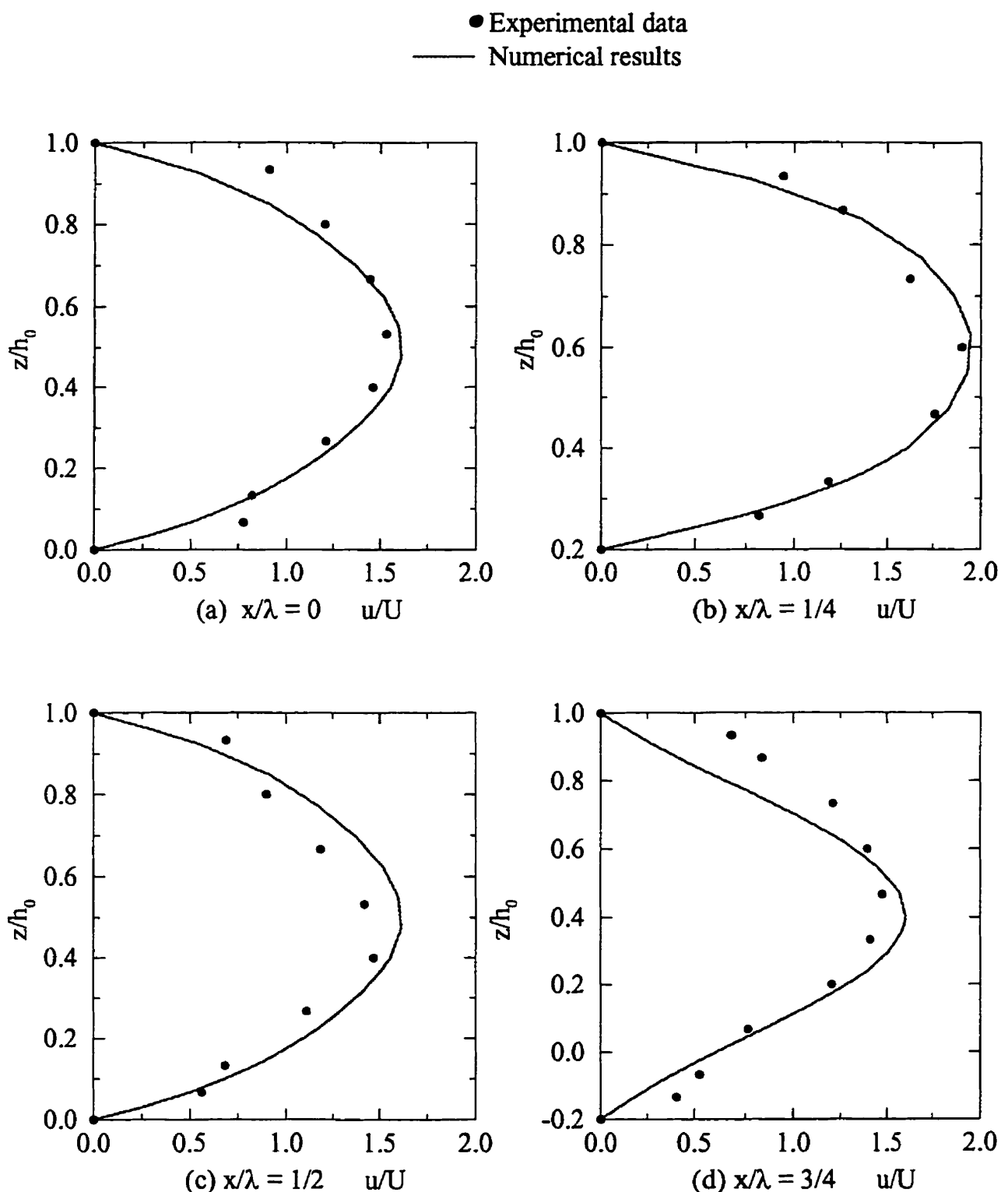


Figure 5.28: Comparison of velocity profile u/U between experimental measurement and numerical results for sinusoidally wavy wall; $Re^* = 0.49$, $\epsilon = 0.20$, $\gamma = 0.012$

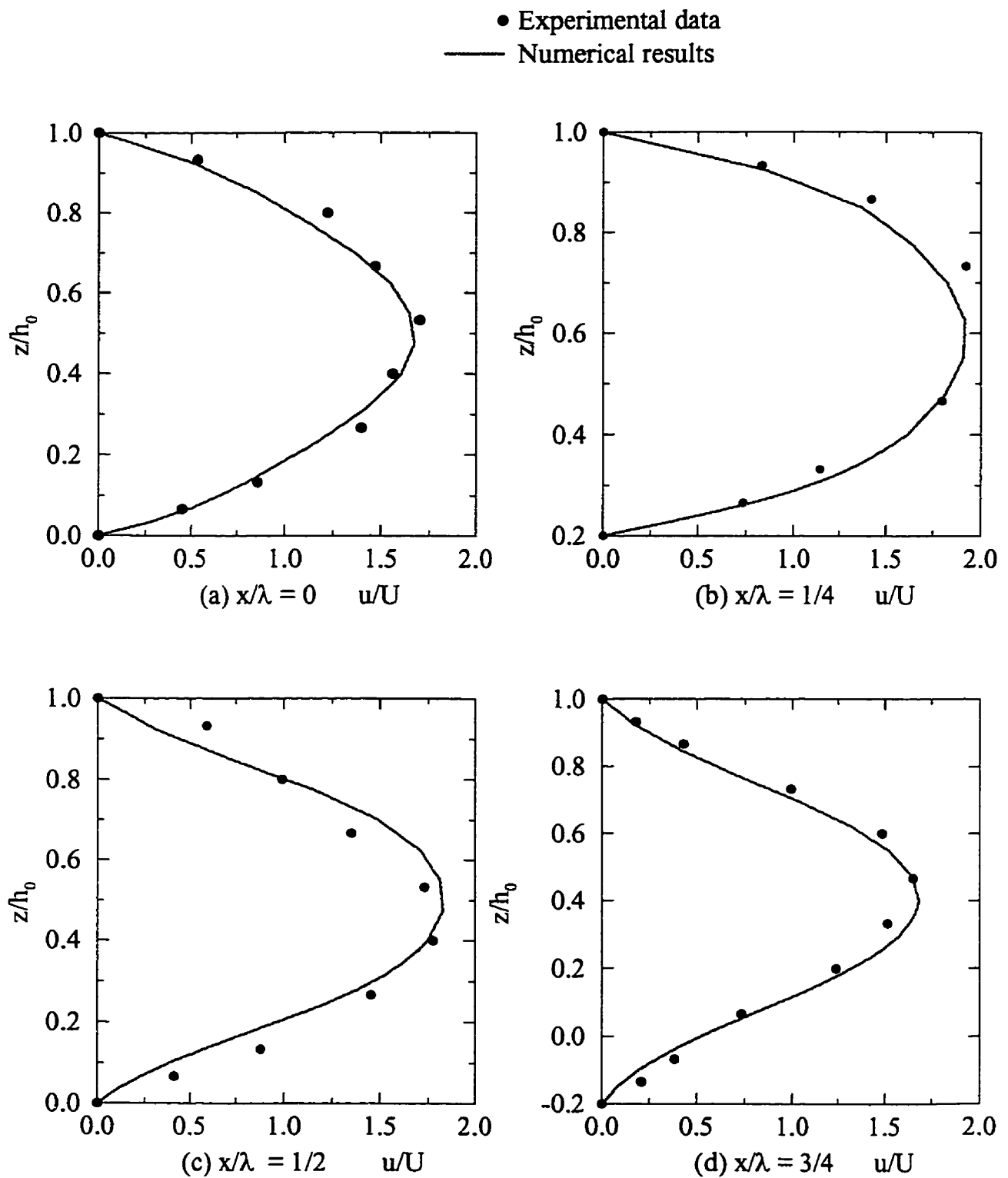


Figure 5.29: Comparison of velocity profile u/U between experimental measurement and numerical results for sinusoidally wavy wall; $Re^* = 1.00$, $\epsilon = 0.20$, $\gamma = 0.012$

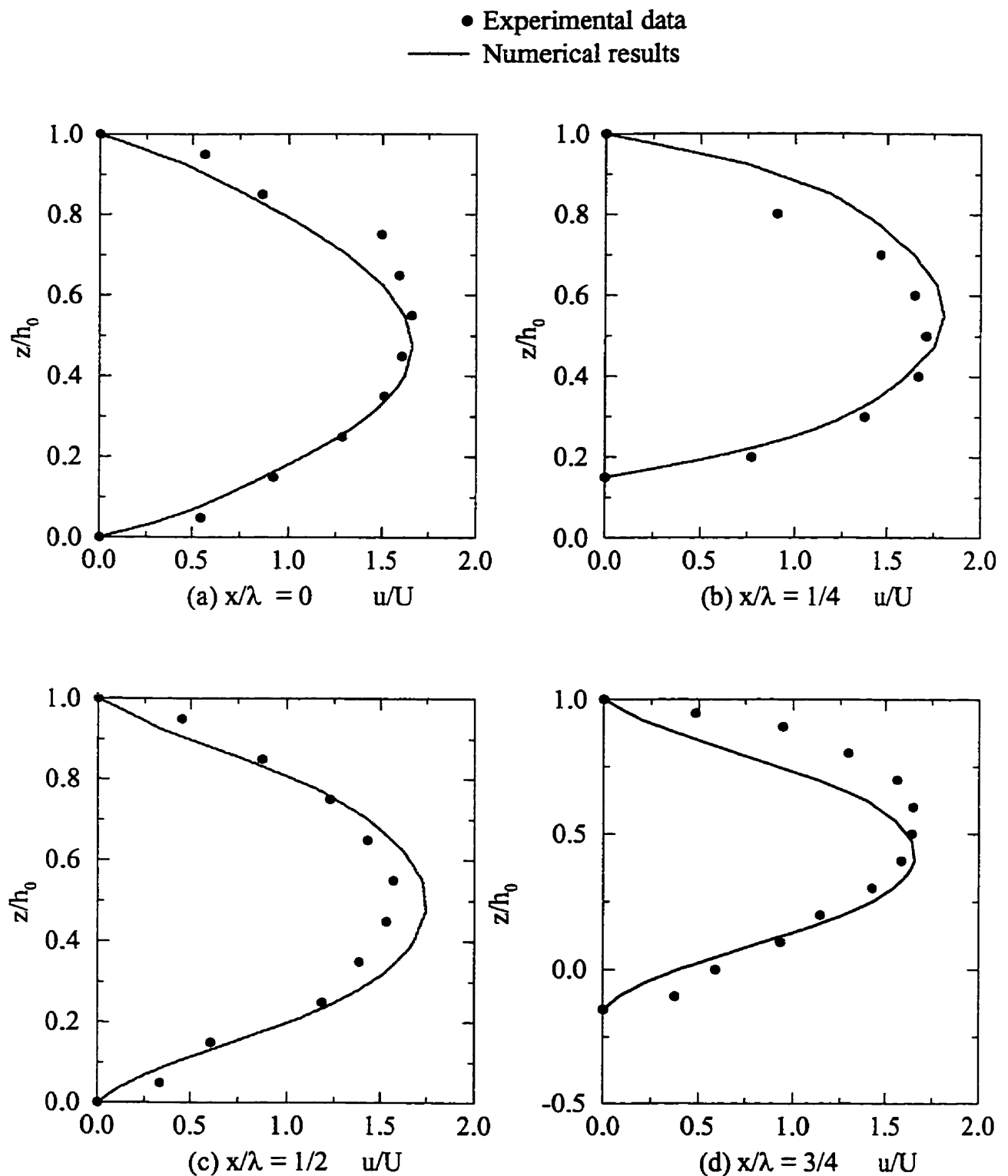


Figure 5.30: Comparison of velocity profile u/U between experimental measurement and numerical results for sinusoidally wavy wall; $Re^* = 1.00$, $\epsilon = 0.15$, $\gamma = 0.012$

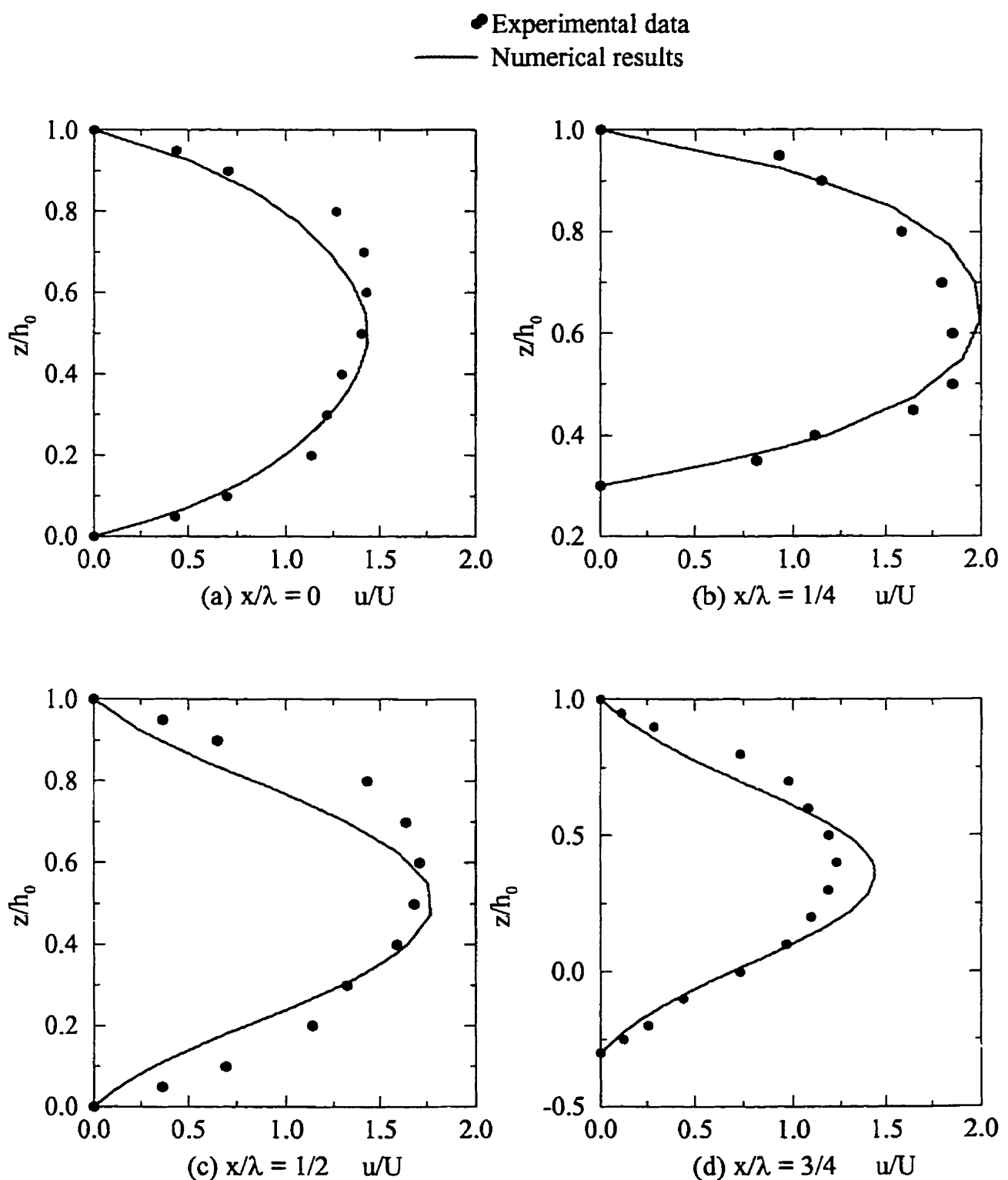
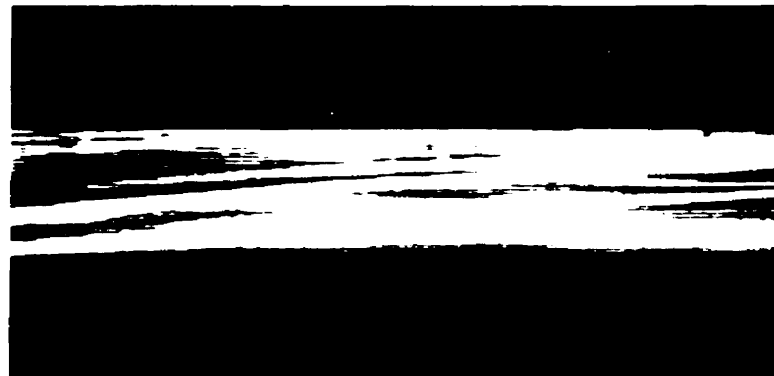
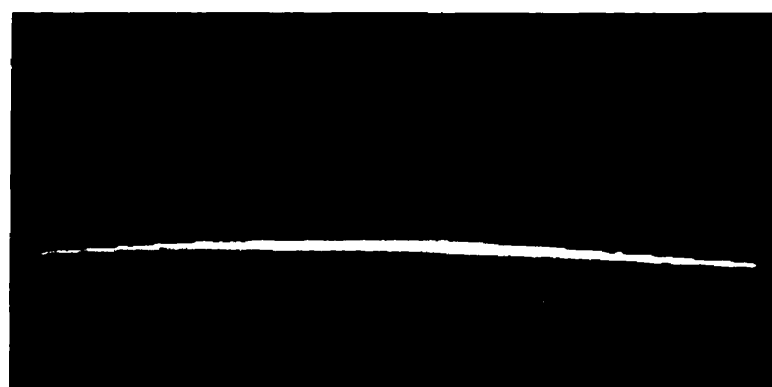


Figure 5.31: Comparison of velocity profile u/U between experimental measurement and numerical results for sinusoidally wavy wall; $Re^* = 0.90$, $\epsilon = 0.30$, $\gamma = 0.012$

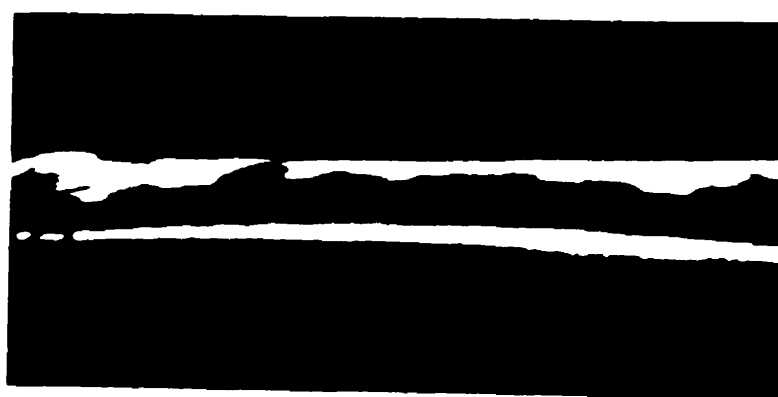
(a) $Re^* = 1.0, \epsilon = 0.15, h_0 = 20mm$ (b) $Re^* = 1.0, \epsilon = 0.2, h_0 = 15mm$ (c) $Re^* = 0.795, \epsilon = 0.3, h_0 = 10mm$ Figure 5.32: Streamlines along sinusoidal wall for varying relative roughness ϵ , $\gamma = 0.012$



(a) Converging area, $Re^* = 1.0$, $h_0 = 20$ mm



(b) Diverging area, $Re^* = 1.0$, $h_0 = 20$ mm



(c) Converging area, $Re^* = 0.429$, $h_0 = 15$ mm

Figure 5.33: Streamlines along sinusoidal wall at various positions, for $\gamma = 0.012$

Chapter 6

Results for Unilateral Randomly Rough Wall

6.1 Introductory remarks

In the absence of an analytical approach in the case of random roughness, recourse must be taken in experimentation. In particular, flow over a unilateral two-dimensional, randomly rough surface was studied by placing an appropriately prepared tile floor into the wind tunnel described in Chapter Three. As before, measurements were undertaken by employing hot-wire anemometry and the smoke-wire technology.

The surface samples tested are patterned after a $0.5\text{ mm} \times 0.5\text{ mm}$ square element of a real bearing pad (Fig. 4.5). One of its contours, represented by digitized data, was arbitrarily chosen to represent the surface. The 1000-times magnified profile is shown,

undistorted, in Fig. 6.1. The corresponding two 25 cm long surface samples are of uniform 25 cm width in spanwise direction. The physical look of the two Plaster of Paris tiles is shown in the photograph of Fig. 6.2. The two two-dimensional, randomly rough testing tiles are named, respectively, RanTes1 and RanTes2.

The testing was done as follows:

- (1). All 32 tiles of set RanTes1 were placed on the bottom of the wind tunnel.
- (2). All 32 tiles of set RanTes2 were placed on the bottom of the wind tunnel.
- (3). Alternate tiles of sets RanTes1 and RanTes2 were installed.

For each test series, various velocities (0.2 m/s to 0.8 m/s) and channel heights (10 mm to 20 mm) were employed. These combinations covered the complete parameter range of interest.

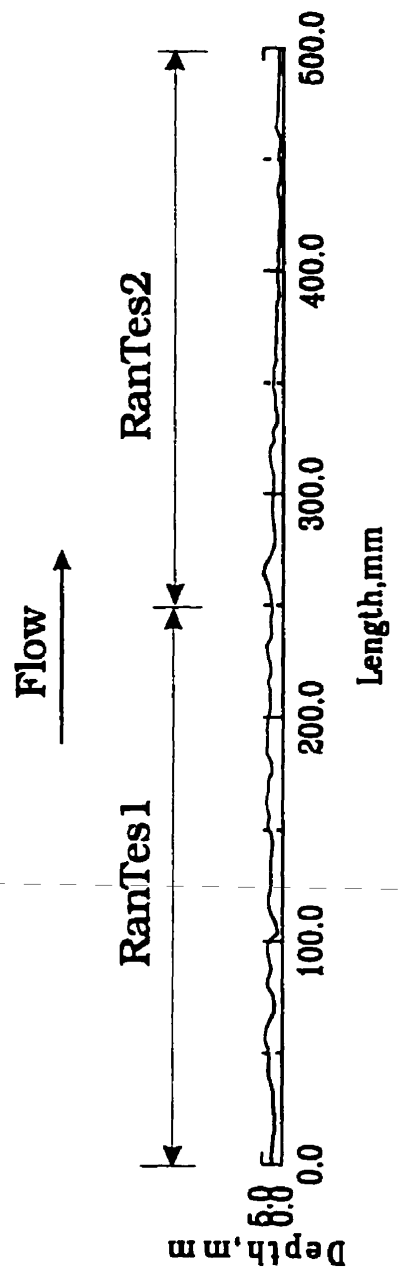


Figure 6.1: Surface profile chosen as testing sample



Figure 6.2: Photograph of the two kinds of randomly rough testing tiles

6.2 Experimental findings

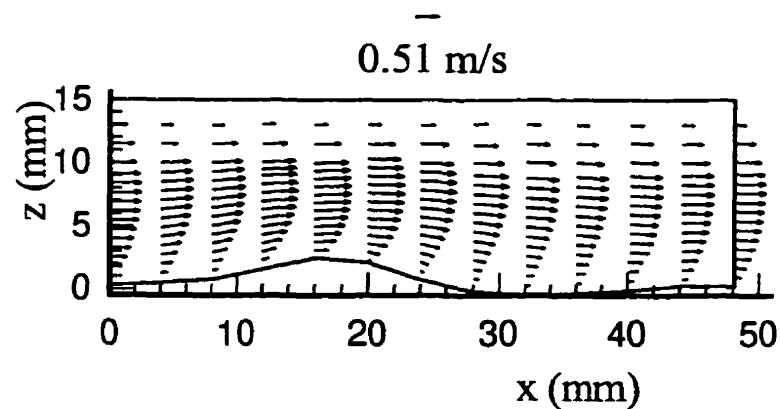
6.2.1 Velocity distribution

Fig. 6.3(a) shows velocity vector plots of a test set RanTes1 in the vicinity of a surface bump, at a reduced Reynolds number $Re^* = 0.349$, for $h_0 = 15$ mm, $\epsilon = 0.049$, and $\gamma = 0.014$. The x -coordinate starts at the leading edge of the tile shown. As described in Chapter Four, all measurements were taken 3 m downstream from the inlet of the channel.

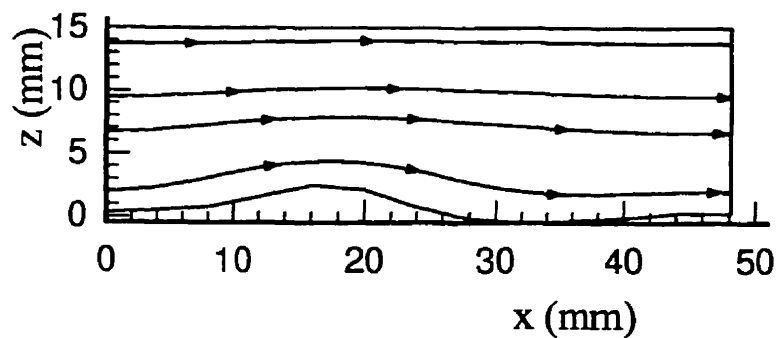
For the conditions indicated, the velocity is essentially parallel to the flat surface and becomes wavy only near the bump. This observation is underlined by the corresponding streamline pattern shown in Fig. 6.3(b). For a decreased channel height, i.e., increased relative roughness, e.g., $h_0 = 10$ mm, $\epsilon = 0.073$, but the same $Re^* = 0.349$ and $\gamma = 0.014$

(as before), the flow is shown in Fig. 6.4. The overall appearance of flow distortion in both cases, Figs. 6.3 and 6.4, is quite similar although, of course, the area percentage of disturbance is larger in the narrow channel depicted in Fig. 6.4.

Corresponding results from tests with RanTes2 show the flow past the severe peaks and cavities. Velocity vector plots and streamlines for $h_0 = 15$ mm and $h_0 = 10$ mm are depicted in Figs. 6.5 and 6.6, respectively. The experimental data, again, indicate that the effects of the surface roughness are essentially confined to the flow in the vicinity of the textured wall. In Fig. 6.5(a) and (b), at $x = 100 - 110$ mm, there is even the suggestion of flow reversal due to separation on the leeward side of a deep cavity. Special attention was paid to analyzing the recorded X-wire signals of the hot-wire probe in the region adjacent to this cavity. The direction of the w -component can be easily identified by the sign of the difference of two effective velocities. But the direction of the u -component needs proper physical judgment in interpreting the complex geometry of the geometry with relatively large slopes to avoid ambiguous or even wrong visualization of the flow, see for example Fig. 6.5(a)($x : 100-110$; $z : 5-10$).

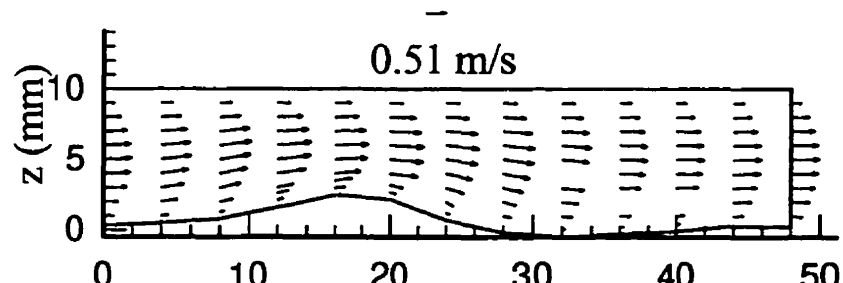


(a) Velocity vector plots

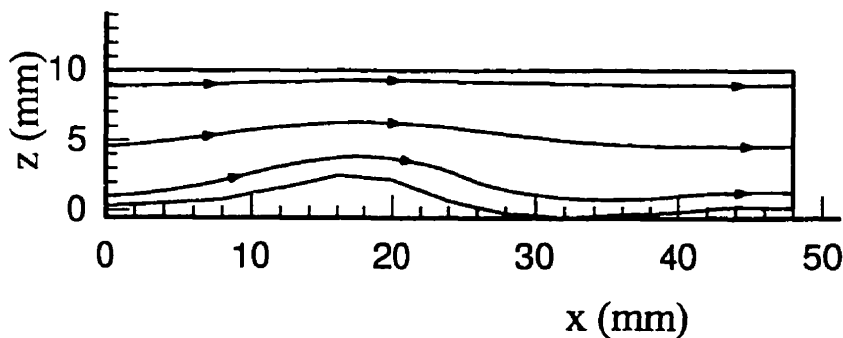


(b) Streamlines

Figure 6.3: Velocity vector plots and streamlines for part of surface RanTes1, by hot-wire anemometry, $Re^* = 0.349$, $\epsilon = 0.049$ ($h_0 = 15\text{mm}$), $\gamma = 0.014$

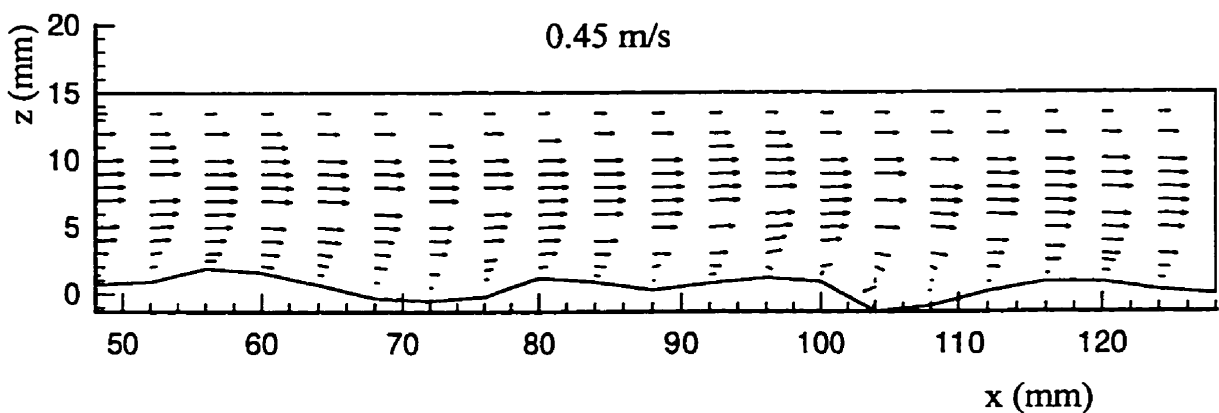


(a) Velocity vector plots

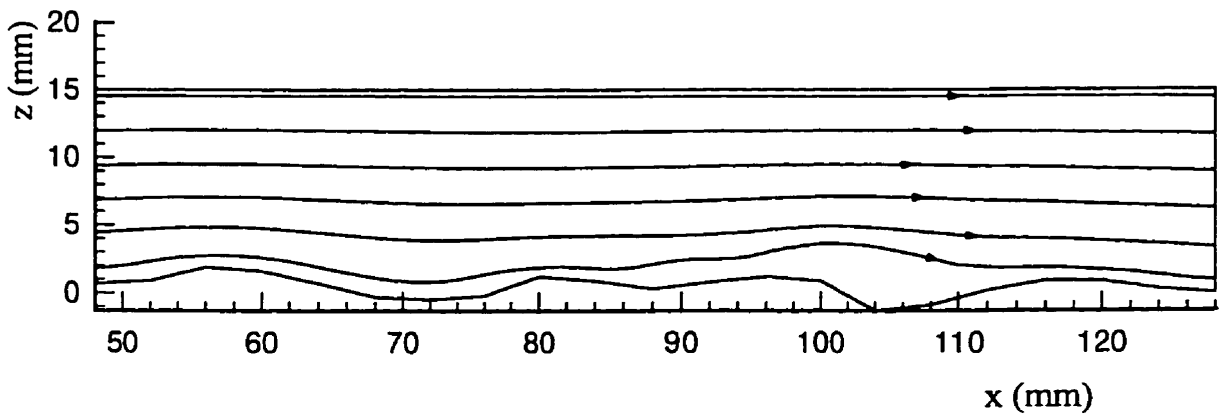


(b) Streamlines

Figure 6.4: Velocity vector plots and streamlines for part of surface RanTes1, by hot-wire anemometry, $Re^* = 0.349$, $\epsilon = 0.073$ ($h_0 = 10$ mm), $\gamma = 0.014$

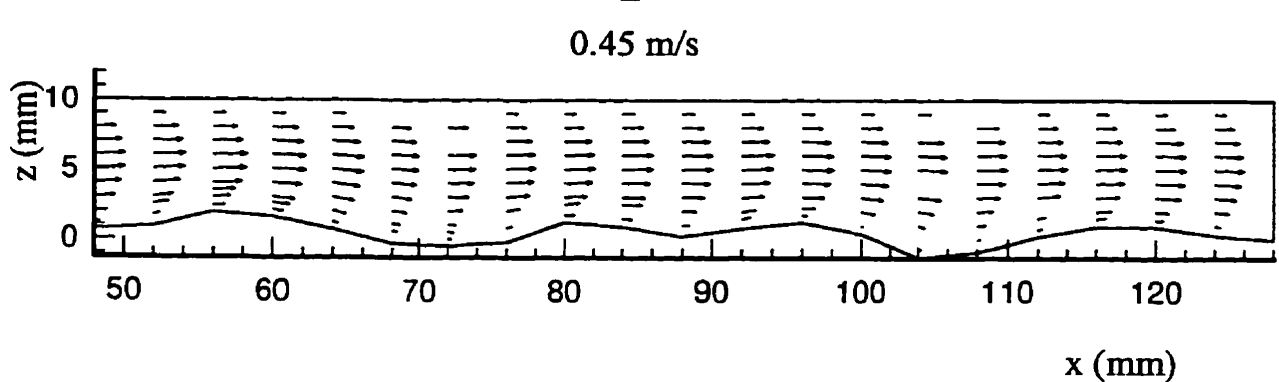


(a) Velocity vector plots

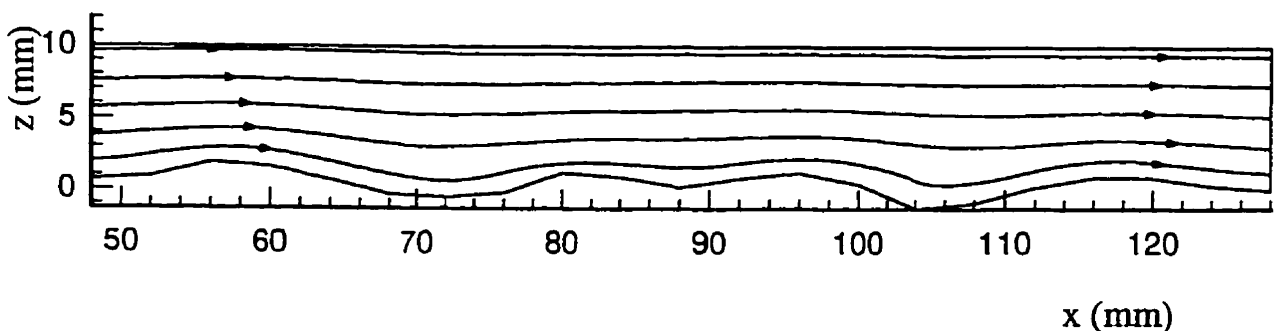


(b) Streamlines

Figure 6.5: Velocity vector plots and streamlines for part of surface RanTes2, by hot-wire anemometry, $Re^* = 0.349$, $\epsilon = 0.052$ ($h_0 = 15$ mm), $\gamma = 0.015$



(a) Velocity vector plots



(b) Streamlines

Figure 6.6: Velocity vector plots and streamlines for part of surface RanTes2, by hot-wire anemometry, $Re^* = 0.349$, $\epsilon = 0.078$ ($h_0 = 10$ mm), $\gamma = 0.015$

6.2.2 Flow visualization

Fig. 6.7 shows video images of streaklines for tile set RanTes1 at $h_0 = 20\text{mm}$ (a) and $h_0 = 15\text{ mm}$ (b).

In Fig. 6.7(a)¹, $\epsilon = 0.037$, $\gamma = 0.014$, $Re^* = 0.349$. The streamlines are basically straight except in the area close to the bump. When the flow passes the bump, the lines are first squeezed together, and then joins other streamlines passing the tip of the bump. At some point downstreams, and depending on the reduced Reynolds number, the flow may become separated.

Fig. 6.7(b) shows streamlines for the same position as in Fig. 6.7(a) but at a different channel height, i.e., $h_0 = 15\text{mm}$; $Re^* = 0.273$, $\epsilon = 0.049$, $\gamma = 0.014$. There is clearly a more vigorous response of the streamlines to the flow contour than is evident in Fig. 6.7(a). This effect may be due to the 33% increase in the value of relative roughness ϵ from 0.037 to 0.049 which overwhelms the simultaneous 22% decrease in Re^* from 0.349 to 0.273.

Streamlines for surface type RanTes2 are shown in Fig. 6.8. With increasing speed, the flow is pushed towards the uneven boundary as shown by these video images. Complementary images are shown in Fig. 6.9. They convey an idea about the velocity distribution across the channel. Thus, it is clear that the smoke remains close to the wall than away from the wall due to lower speed there and possible flow disturbance downstream of the bump.

¹note that the bottom line is the surface contour from light reflection



(a) RanTes1, $\epsilon = 0.037$ ($h_0 = 20\text{mm}$), $Re^* = 0.349$



(b) RanTes1. $\epsilon = 0.049$ ($h_0 = 15\text{mm}$), $Re^* = 0.273$

Figure 6.7: Streamlines for various values of relative roughness, $\gamma = 0.014$



(a) RanTes1, $\epsilon = 0.049$ ($h_0 = 15$ mm), $Re^* = 0.273$, $\gamma = 0.014$



(b) RanTes2, $\epsilon = 0.039$ ($h_0 = 20$ mm), $Re^* = 0.312$, $\gamma = 0.015$



(c) RanTes2, $\epsilon = 0.039$ ($h_0 = 20$ mm), $Re^* = 0.401$, $\gamma = 0.015$

Figure 6.8: Streamlines for various values of reduced Reynolds number Re^*

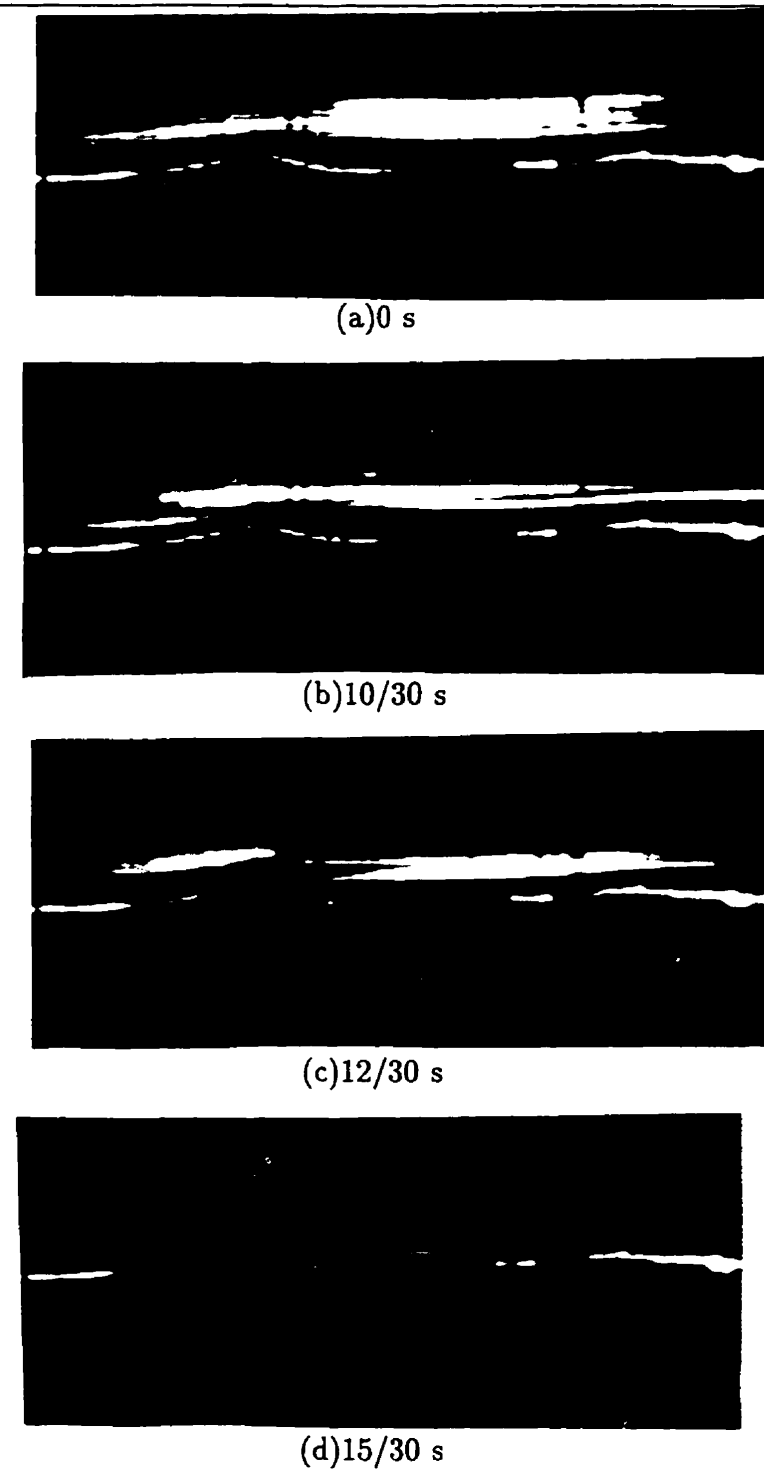


Figure 6.9: Temporal flow streaklines for RanTes1 at $Re^* = 0.273$, $\epsilon = 0.049$ ($h_0 = 15$ mm), $\gamma = 0.014$

Chapter 7

Threshold of the Smooth Boundary Condition

7.1 Unilateral sinusoidally wavy wall

Based on the findings of Chapter Five, the friction coefficient appears to be an appropriate means for sensing the influence of surface irregularities on the flow. Accordingly, it seems reasonable to exploit this concept further to determine, for instance, the threshold of applicability of the classical Reynolds equation, or, in different words, to establish the limiting conditions for the assumption of a physically smooth boundary. To this end, it is convenient to define a “sensitivity parameter”, χ , as follows,

$$\chi(\%) = \left[\frac{f^* - f}{f} \right] 100 \quad (7.1)$$

where f^* is the actual friction coefficient, f is the Darcy-Weisbach friction factor for plane Poiseuille flow, and the departure of the friction coefficient f^* from the f -base represents the degree of severity of the surface roughness effect. Figs. 7.1 and 7.2 show the variation of χ with relative roughness ϵ for different values of reduced Reynolds numbers Re^* and steepness γ . Fig. 7.3 depicts the influence of steepness γ on χ and, finally, Fig. 7.4 portrays the variation of the sensitivity parameter with reduced Reynolds number.

All of the various presentations reveal a significant response of χ to even small changes in inputs of Re^* , ϵ , or γ . This observation identifies the sensitivity parameter χ as well suited for determining threshold levels, such as the limit of applicability of the classical Reynolds equation.

Any particular value of χ defines an enveloping surface in the three-dimensional $Re^* - \epsilon - \gamma$ space. An example of such an envelope for the relevant case of a channel with a unilateral sinusoidally wavy wall, for the typical engineering value of $\chi = 10\%$, is shown in Fig. 7.5. The classical Reynolds equation may be applied to any combination of values of Re^* , ϵ , and γ enclosed by this surface. Outside of this surface, a modified form of Reynolds equation must be used which makes proper allowance for micro-inertia effects of surface roughness. This modified Reynolds equation remains, as yet, undefined although the findings of the present research ought to provide a solid first step in its eventual development.

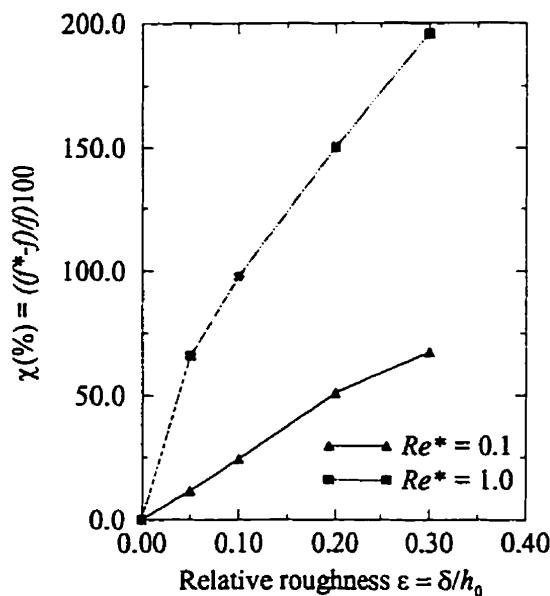


Figure 7.1: Variation of sensitivity parameter χ with relative roughness ϵ for two values of Re^* ; $\gamma = 0.1$

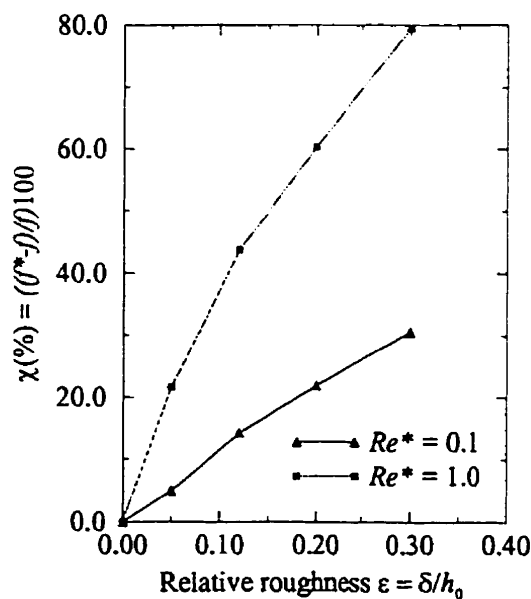


Figure 7.2: Variation of sensitivity parameter χ with relative roughness ϵ for two values of Re^* ; $\gamma = 0.012$

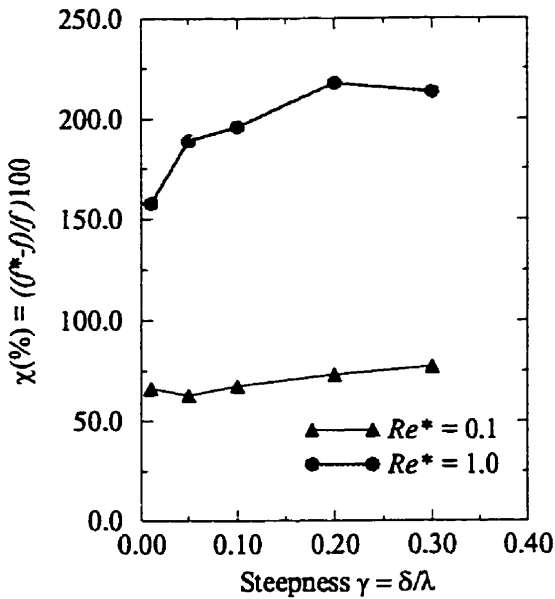


Figure 7.3: Variation of sensitivity parameter χ with steepness γ for two values of Re^* ; $\epsilon = 0.3$

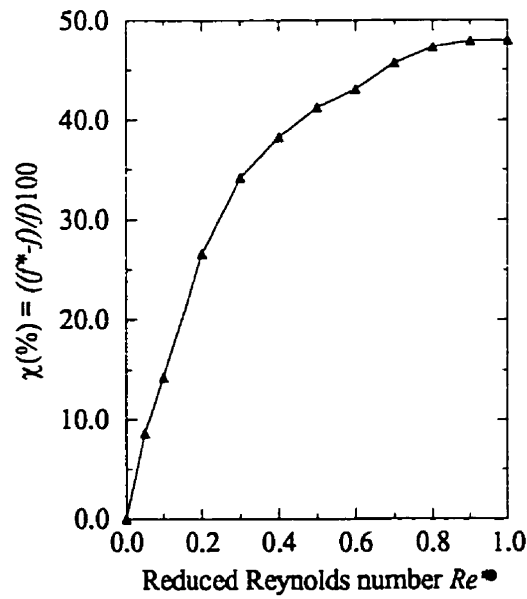


Figure 7.4: Variation of sensitivity parameter χ with reduced Reynolds number Re^* ; $\epsilon = 0.12$, $\gamma = 0.012$

7.2 Two-dimensional randomly rough wall

For two-dimensional randomly rough surfaces, the average roughness R_a and average wavelength λ_a must be obtained from surface measurements. For a given lubrication application, i.e., known values of viscosity, relative velocity, and anticipated fluid film thickness, the values of reduced Reynolds number, relative roughness, and steepness can then be calculated.

The crucial step of judging the applicability of the classical Reynolds equation is the identification of the appropriate sensitivity surface χ (Re^* , ϵ , γ). In the absence of more detailed information, an approximate analysis may be based on the two-dimensional roughness model described in Appendix C. Since the mean angular frequency ω_a is inversely proportional to the average wavelength λ_a it can be used to sense the variation of power spectrum [see Eq. (C.9)]. It is thus not unreasonable to consider a randomly rough, albeit two-dimensional surface as used in hydrodynamic lubrication to be equivalent to a sinusoidally wavy surface with $\delta = R_a$ and $\lambda = \lambda_a$ as studied in this thesis.

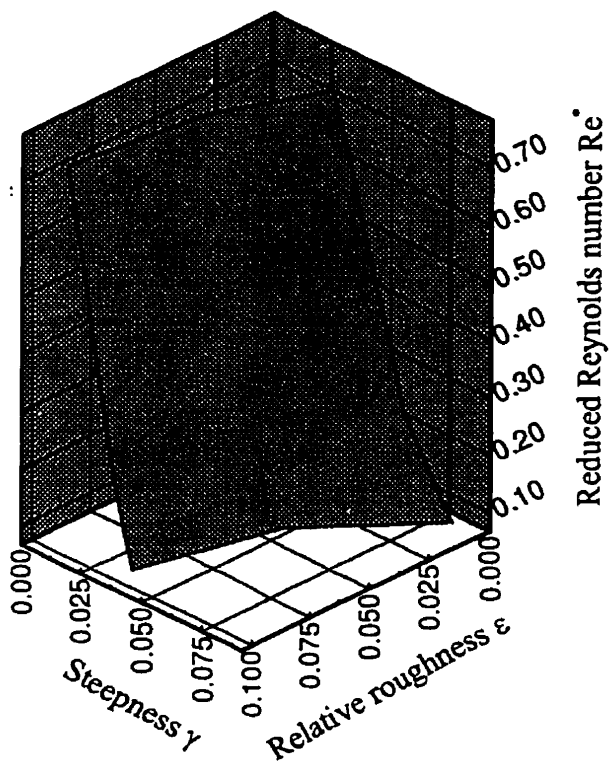


Figure 7.5: Envelope of equal sensitivity parameter $\chi = 10\%$

Chapter 8

Conclusions

A novel approach has been developed for studying the effects of surface roughness on laminar hydrodynamic lubrication. It introduces the concept of micro-inertia in consequence of convectively accelerated fluid motion about surface asperities.

The micro-inertia effects are investigated in the light of similitude principles involving a newly conceived reduced Reynolds number Re^* , and the two length parameters of surface steepness γ and relative roughness ϵ .

The work is focused on the particular case of pressure-driven laminar flow in a two-dimensional channel with one sinusoidally wavy wall. A numerical solution of the Navier-Stokes equation, obtained by means of the finite element method, is employed as the principal numerical tool. The analytical model is substantiated by matching experiments performed in a specially designed wind tunnel. In some tests, models of actual bearing surfaces, albeit enlarged at a linear scale of 1000:1, were used.

Findings indicate that micro-inertia effects are, essentially, restricted to the flow region adjacent to the rough wall. When the effects are weak, the flow follows the surface contour. When the effects grow stronger, the wall recesses turn into driven cavities. Outside these recesses the flow appears always rather undisturbed and seemingly just "streams" from one high point of the surface to the next one.

Micro-inertia effects can be quantified by a very responsive sensitivity parameter, χ . This permits to construct surfaces, or envelopes, $\chi (Re^*, \epsilon, \gamma) = \text{constant}$ from which threshold levels, such as the applicability limit of the classical Reynolds equation, may be deduced.

Experiments with randomly rough two-dimensional surfaces confirm the "streaming" of the flow past the tips of the surface irregularities. There is good reason to believe that, at least in first approximation, randomly rough two-dimensional surfaces may be considered equivalent to sinusoidally wavy ones.

Appendix A

Simplifying Assumptions Used in Hydrodynamic Lubrication

For the mathematical description of conventional hydrodynamic lubrication, (i.e., steady, laminar, incompressible), the Navier-Stokes and the continuity equations (Eqs.(2.4) –(2.6)), or more usual in engineering practice, their simplified derivative known as the Reynolds equation, are applied. Subject to the boundary conditions implied by Fig. A.1¹, for example, this equation has the form as follows:

$$\frac{\partial}{\partial x}(h^3 \frac{\partial p}{\partial x}) + \frac{\partial}{\partial y}(h^3 \frac{\partial p}{\partial y}) = 6\mu \frac{\partial h}{\partial x} . \quad (\text{A.1})$$

¹This three-dimensional case is somewhat more general than the two-dimensional one forming the subject matter of this thesis. It may be noted that Eq. (A.1) is often termed two-dimensional because integration across the film has reduced this actually three-dimensional problem by one dimension!

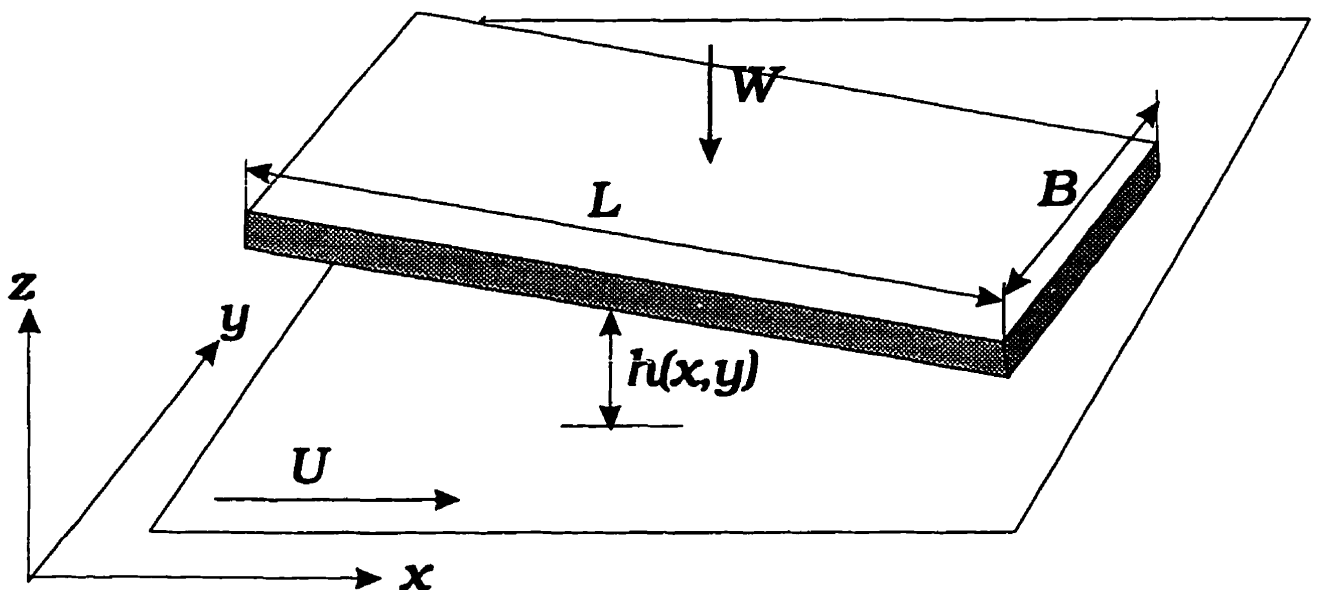


Figure A.1: Clarifying diagram

It is instructive to identify the assumptions which are involved in developing Eq. (B.6).

They are listed in Table A.1. The first four items of the table are based on fluid dynamics considerations [CRC Handbook of Lubrication (1994); Williams (1994)]. There may be some extreme working conditions, like a very large bearing operating at high speed, or a very thin film of gaseous lubricant, where the conditions of laminar flow (#1), or fluid continuum (#3) may have to be verified. Similarly, inertia due to the macro-geometry of bearings may not be neglected (#6) if the inertial term is comparable to the viscous term in the Navier-Stokes equation, i.e., if the macroscopic reduced Reynolds number Re^{**} is significant.

When the fluid film pressure is extremely high, as it happens in components such as gears and cams, deformation of the bearing surfaces and compression of the fluid become a reality (#10), and the problem may turn into one of elasto-hydrodynamic lubrication

No.	Assumptions	Basis	Comments
1	The flow is laminar	Fluid dynamics	Usually true, only violated in large and high speed bearings.
2	The body forces are negligible	Fluid dynamics	Usually true, except in magnetic-bearings.
3	There is no slip at the boundaries	Fluid dynamics	Usually true. Not for very thin gas film.
4	The density is constant	Fluid dynamics	Usually true, but not for gases.
5	The viscosity is constant	Thermo-dynamics	Not necessarily so, but facilitates analysis.
6	The fluid inertia is ignored	Observation	Usually true in steady state.
7	The effects of the boundary curvature are negligible	Observation	True, since the film thickness is small compared with the other lengths of a bearing.
8	$\frac{\partial}{\partial z} \gg \frac{\partial}{\partial x}, \frac{\partial}{\partial y}$	Observation	Generally true.
9	The pressure is constant across the film thickness	Observation	See (7) above.
10	The surfaces are rigid	Material property	Usually true, with exception of high pressure or compliant surfaces.
11	The surfaces are smooth	Observation	Generally true, except when fluid film is very thin.

Table A.1: Assumptions made in the derivation of the Reynolds equation (EHL).

The last item of Table A.1 is the one of primary interest in the present work. When the film thickness is of the same order of magnitude as the surface roughness, then the micro-inertial effects can not be neglected.

Appendix B

Overview of Lubrication Theories of Bearing Roughness

A comprehensive review of the major theoretical developments on the effects of surface roughness on hydrodynamic lubrication was given by Elrod (1978). There, various kinds of a modified Reynolds equation are discussed for the case of striated (two-dimensional) roughness, see Fig. B.1. In an updated review of the subject by Cheng (1984) are presented several theoretical methods for dealing with arbitrary (three-dimensional) roughness. The following material addresses the concepts on which the various extant theories are based.

A random character of surface roughness renders the film thickness, and, hence, the solution of the Reynolds equation, i.e., the pressure, a random variable. It is this feature that demands an ensemble-averaged lubrication equation in order to smoothen the stochastic component of the pressure. The methods adopted by previous investigators to this end

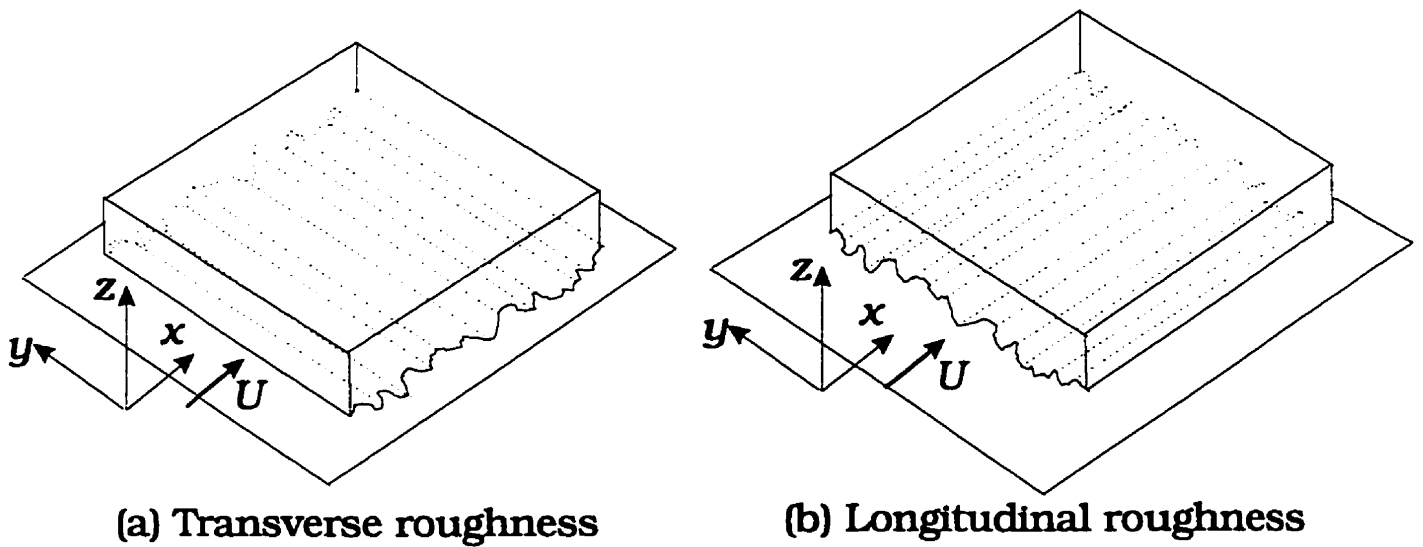


Figure B.1: Definition diagrams of two-dimensional roughness

fall into one of two categories: (I) averaging the Reynolds equation, and (II) averaging the solutions obtained for various numerically simulated forms of roughness.

Since surface roughness may be characterized by statistical properties, analytical treatment by relevant concepts appears appropriate. Tzeng and Saibel (1967) were the first to do this by a method of category (I) in their study of two-dimensional transverse bearing roughness. For the case of a slider bearing, with roughness on one of the two surfaces as shown in Fig. B.2, the local film thickness $h(x)$ in Eq. (B.1) below¹

$$\frac{\partial}{\partial x} \left(h^3 \frac{\partial p}{\partial x} \right) = 6\mu \frac{\partial h}{\partial x} . \quad (\text{B.1})$$

is replaced by h_T . This is written as

¹Eq. (B.1) is identical with Eq. (1.1)

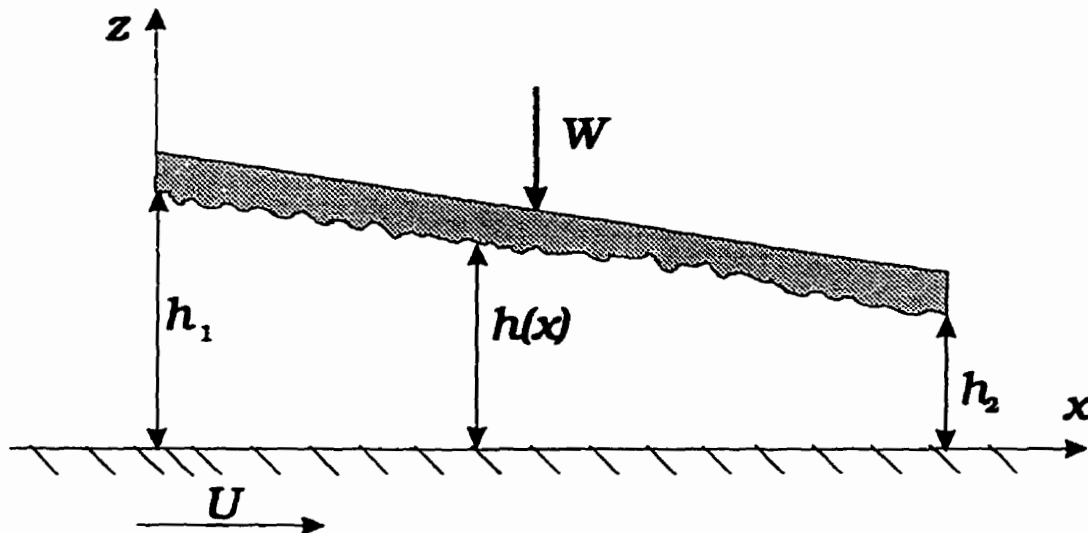


Figure B.2: Slider bearing with roughness on static surface

$$h_T = h_0 + h_\delta \quad (\text{B.2})$$

where h_0 is the nominal film thickness, and h_δ is the random roughness deviation from the mean bearing surface. With this substitution, Eq. (B.1) becomes

$$\frac{d}{dx} \left(h_T^3 \frac{dp}{dx} \right) = 6\mu U \frac{dh_T}{dx} \quad (\text{B.3})$$

or, once integrated,

$$\frac{dp}{dx} = 6\mu U \left(\frac{1}{h_T^2} - \frac{h_T^*}{h_T^3} \right) \quad (\text{B.4})$$

where $h_T^* = h_T$ when $dp/dx = 0$.

Finally, taking the expected values of Eq. (B.4) results in

$$\frac{d\bar{p}}{dx} = 6\mu U \left(E \left[\frac{1}{h_T^2} \right] - E \left[\frac{h^*}{h_T^2} \right] \right) \quad (B.5)$$

where $E[\dots]$ denotes the expectancy of the variables in square brackets, and \bar{p} is the average pressure.

A more general stochastic method was developed by Christensen (1969/70) for both longitudinal and transverse roughness. It starts with the two-dimensional Reynolds equation [Eq. (A.1)]

$$\frac{\partial}{\partial x} \left(h^3 \frac{\partial p}{\partial x} \right) + \frac{\partial}{\partial y} \left(h^3 \frac{\partial p}{\partial y} \right) = 6\mu \frac{\partial h}{\partial x}. \quad (B.6)$$

There is no integration possible as in the case of Tzeng & Saibel's (1967) method to separate the expectation terms. Instead, two postulates are made to simplify the stochastic process:

- (1) The pressure gradient in the roughness direction is independent of local film thickness h_T ; and
- (2) the flow rate per unit width in the direction perpendicular to the roughness direction, is independent of the local film thickness.

For longitudinal roughness, h_T^3 and $\frac{\partial p}{\partial x}$ in the first term of the lefthand side of Eq. (B.5) may be considered stochastically independent quantities by the first postulate; by the second postulate, the flow rate per unit width q in y direction is proportional to:

$$h_T^3 \frac{\partial p}{\partial y}. \quad (B.7)$$

After several steps of manipulation, the second term of the lefthand side of Eq. (B.5) becomes, respectively,

(a) for longitudinal roughness

$$\frac{\partial}{\partial y} E \left(h_T^3 \frac{\partial p}{\partial y} \right) = \frac{\partial}{\partial y} \left[\frac{\partial \bar{p}}{\partial y} \frac{1}{E(1/h_T^3)} \right] \quad (\text{B.8})$$

(b) for transverse roughness

$$E \left[h_T^3 \frac{dp}{dx} \right] = E[h_T^3] \frac{d\bar{p}}{dx} \quad (\text{B.9})$$

With these terms the corresponding forms of the Reynolds equation according to Christensen (1969-70) are

(a) for longitudinal roughness

$$\frac{\partial}{\partial x} \left[\frac{\partial \bar{p}}{\partial x} E(h_T^3) \right] + \frac{\partial}{\partial y} \left[\frac{\partial \bar{p}}{\partial y} \frac{1}{E(1/h_T^3)} \right] = 6\mu U \frac{\partial}{\partial x} E(h_T) \quad (\text{B.10})$$

(b) for transverse roughness

$$\frac{\partial}{\partial x} \left[\frac{\partial \bar{p}}{\partial x} \frac{1}{E(1/h_T^3)} \right] + \frac{\partial}{\partial y} \left[\frac{\partial \bar{p}}{\partial y} E(h_T^3) \right] = 6\mu U \frac{\partial}{\partial x} \frac{E(1/h_T^2)}{E(1/h_T^3)} \quad (\text{B.11})$$

Tønder (1986; 1987) included a coordinate transformation, see Fig. B.3 and Eq. (B.12), to adapt the above Reynolds equation Eqs. (B.10) and (B.11) for a more general type of striated roughness.

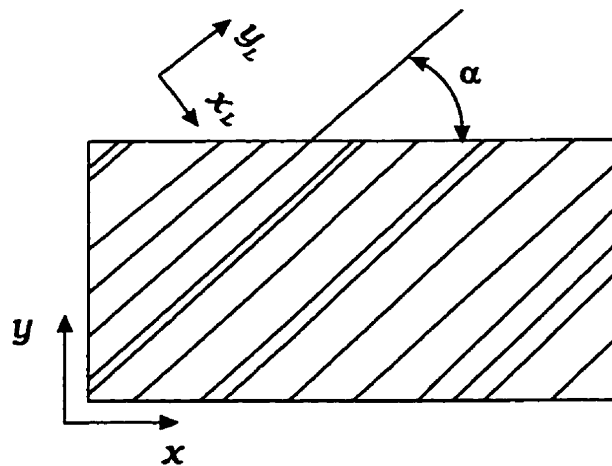


Figure B.3: Coordinate transformation for inclined striated roughness

Bearing Characteristics	Longitudinal Roughness	Transverse roughness
Load capacity W	small decrease	significant increase
Flow rate q	small decrease	significant increase
Friction force F_r	insignificant increase	significant increase
Friction coefficient F_r/W	significant increase	significant decrease

Table B.1: Comparison of the effects of surface roughness

$$x_L = y \sin \alpha + x \cos \alpha \quad (B.12)$$

$$y_L = y \cos \alpha - x \sin \alpha$$

Christensen applied Eqs. (B.10) and (B.11) to a slider bearing to evaluate the overall characteristics of a bearing. His findings are given in Table B.1.

An interesting point should be brought out here. From Table B.1 follows that transverse roughness increases both the load capacity and the friction force. Based on the computations of Christensen (1969–1970), however, the increase in frictional resistance force F_r is less than the increase in load capacity W and, hence, the friction coefficient F_r/W decreases.

If this conclusion should be substantiated by experiments, it might become a valuable tool in bearing design by using transverse roughness to improve bearing performance. In practice, bearings vary in their geometries relative to their particular application. Thus, while Christensen's finding may hold true for finitely long sliders, it may not apply to all other types of bearings.

For arbitrary, i.e., three-dimensional, roughness the derivation of a stochastic Reynolds equation similar to those discussed in the foregoing is not possible. Instead, two approximate methods of category II, were conceived by, respectively, Patir and Cheng (1978) and Elrod (1979) to deal with the problem, viz.: (i)numerical simulation of the average flow, and (ii) perturbation analysis of the surface profile.

In Patir and Cheng's "average flow" model, flow factors determined by averaging numerical simulations of lubricant flow over a microscope bearing area, account for the roughness effects. In this model, the actual flow between rough surfaces is thought to be equal to an average flow between nominally smooth ones. However, the boundary conditions of this model are unclear and have been questioned [Teale and Lebeck (1980); Tønder (1980); Tripp (1983); Hu and Zheng (1989)].

Elrod's (1979) model of "Reynolds roughness" applies only to very gentle deformations of a surface. Predictions of friction effects by this model in the case of closely spaced surfaces in relative motion are considered unreasonable.

In contrast to theoretical studies, there are very few pertinent experiments reported in the literature. Probably the first tests on friction and film thickness in a rough slider bearing

were carried out by Hata, Nakahara and Aoki (1980). More recently, Jeng (1990) developed a computer-aided pin-on-disc tribometer for measuring the friction of the tested rough surface specimen. A significant finding of flow visualization tests (Jeng, 1990) has verified the lower load carrying capacity of longitudinal roughness. However, the visualization results are inconclusive regarding the effects of transverse and isotropic roughness. All tests reported so far have failed to provide sufficient experimental data to support relevant analytical or numerical results.

There remain several unresolved issues of the subject at hand. For instance, does roughness improve or worsen the performance of hydrodynamic lubrication? If it does, what kind of roughness should be used, isotropic, striated, periodic, or randomly distributed? The major hold-up to finding an answer to these questions derives from the fact that it is extremely difficult to manufacture a surface with controlled characteristics, and to prove a proposed theory by experiments.

Appendix C

Aspects of Surface Topography

The constituent geometric components of the deviation of a solid surface from its actual shape fall into three categories: errors of form, waviness, and roughness (Fig. C.1). The most important difference between roughness and the other two deviations is the much shorter wavelength of the former. According to the British Standard (B.S. 1134:1961), roughness is the irregularity in the surface texture which results from the inherent action of the production process. The major interest of this study is in the effects of roughness on hydrodynamic lubrication.

Surface roughness, or texture, may be readily visualized through the medium of a surface profile, i.e., a contour of surface height relative to a fixed datum line. The principal source of quantitative data on surface texture is obtained from surface profilometry. The stylus profiler was invented in the 1940's (Whitehouse, 1994). It produces a signal proportional to the height of the contour relative to its datum, while the distance traveled by the sensor

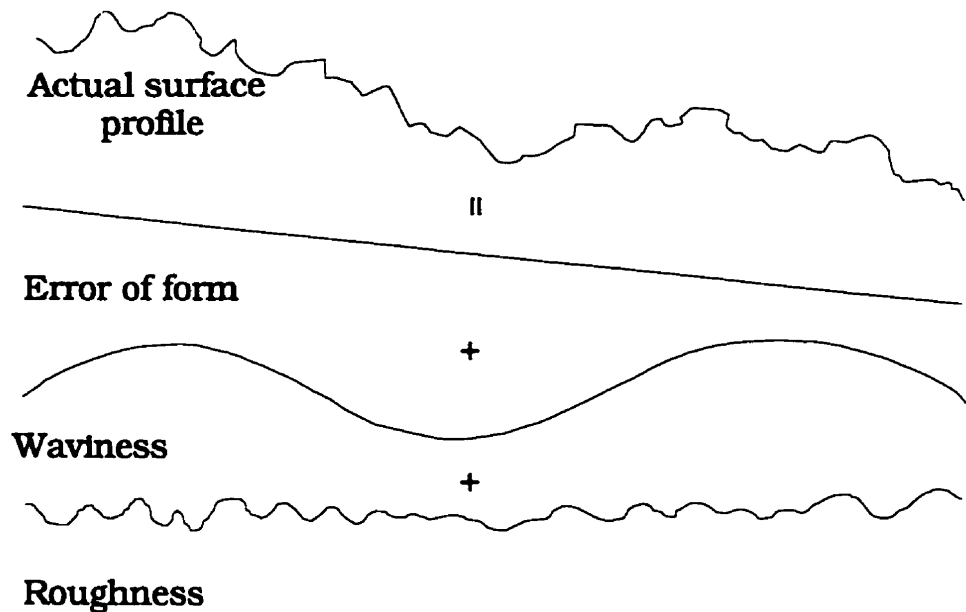


Figure C.1: Geometric components of a surface

along the surface is transformed into another analogue signal. After being amplified, these two signals are fed into a chart recorder, or to an A/D converter connected to a storage device, from which a surface profile and calculations of parameters can be implemented. An example of surface profile is given in Fig. C.2. It shows that the customary graphical representation of surface roughness may lead to significant misunderstandings due to the exaggerated magnification of the height of roughness by scale distortion. Thus, it is seen from Fig. C.2(a) that the real surface undulates with a relatively smaller slope than it appears in Fig. C.2(b) and (c).

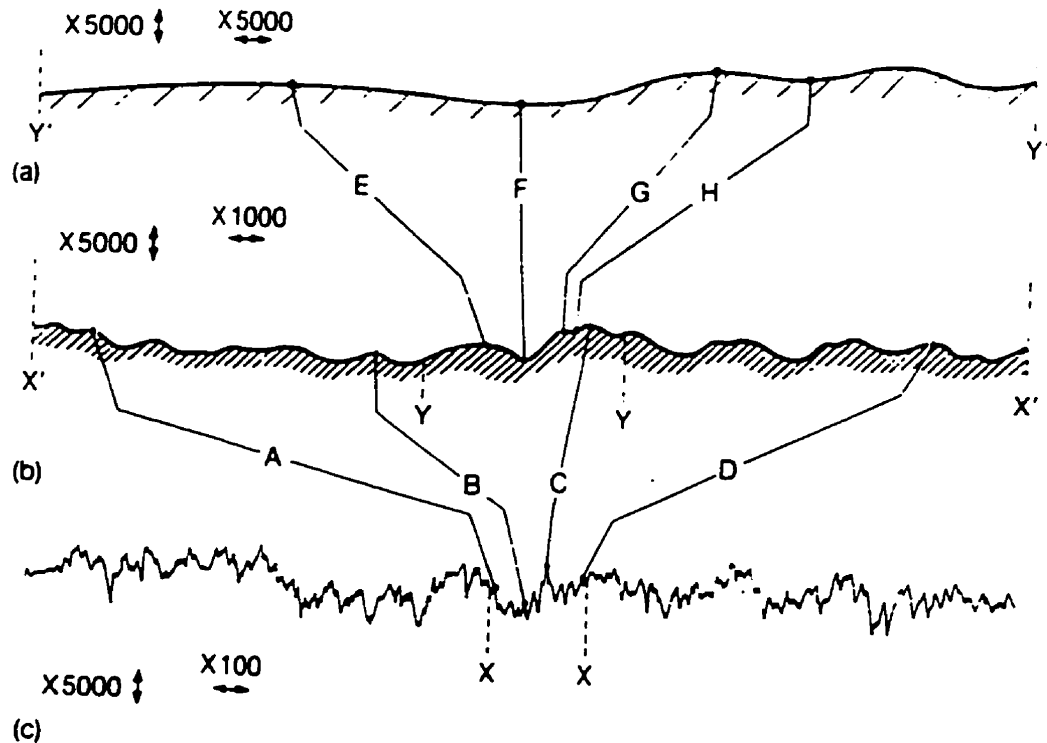


Figure C.2: Surface profile: (a)The profile of a real surface greatly magnified; (b) the profile of the surface with a 5-times larger vertical magnification than a horizontal one; (c) as (b), but with ratio of 50:1 (From Dabhall, 1980)

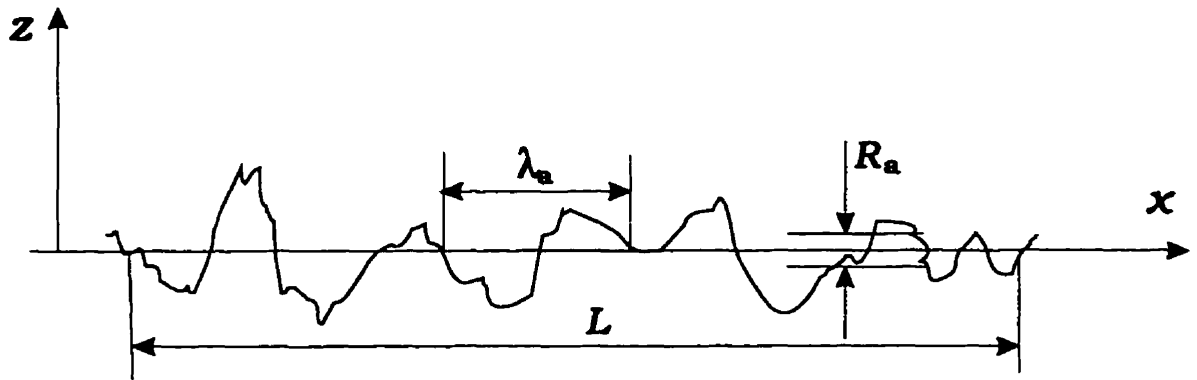


Figure C.3: Geometrical representation of R_a and λ_a of a surface profile

There are a variety of topographical parameters which may be derived from a surface profile by statistical functions commonly used for the description of random data in engineering applications, see, e.g., Peklinik (1967/68), Nayak (1971), Thomas and King (1977) and Sherrinton (1987).

For different engineering problems, different parameters, or combination thereof may be found useful. In the case of hydrodynamic lubrication, it is the height characteristics and the areal distribution of the surface roughness which are relevant, in general. In this thesis, however, attention is restricted to two-dimensional flow situations. Accordingly, and with reference to Fig. C.3, surface roughness is described herein by a single-line-average height

$$R_a = \frac{1}{L} \int_0^L |z| dx \quad (C.1)$$

or its root-mean-square value

$$R_q = \sqrt{\frac{1}{L} \int_0^L z^2 dx} \quad (C.2)$$

and the corresponding length parameter, introduced by Spragg and Whitehouse (1970/71) and termed *average wavelength*,

$$\lambda_a = 2\pi \frac{R_a}{\Delta_a} \quad (C.3)$$

where Δ_a is the mean slope of the roughness profile

$$\Delta_a = \frac{1}{L} \int_0^L \left| \frac{dz(x)}{dx} \right| dx. \quad (C.4)$$

It can be shown that a two-dimensional, randomly rough surface is composed of various wavelengths of sinusoids (Mulvaney and Newland, 1986). The representation of surface texture confined within a band of surface wavelengths can be obtained by Fourier transform. Further study has indicated that 99.5 per cent of the power in profiles recorded from machined, i.e., shaped, turned, and ground specimens is contained in, respectively, 12, 20, and 50 of the most significant terms of the Fourier series (Sherrington and Smith, 1987, 1988). The flow over these rough surfaces may thus be determined by a few deterministic wavelengths of sinusoids for periodically wavy surface.

However, the approach to obtain a fairly accurate reconstruction of a surface with a relatively small number of Fourier coefficients has no capability of interpreting the flow

passing a randomly rough surface. An alternative way from the power spectrum analysis would lead to a reasonably proximate equivalence between randomly rough surface and sinusoidally wavy surface.

As mentioned, the average wavelength can be obtained from the profile by dividing R_a by mean slope Δ_a (Eqs. (C.3) and (C.4)). This frequency conscious parameter can also be determined by the power spectrum.

If the distance along a surface is x and the vertical displacement of the surface is a function of distance $z(x)$, the autocorrelation function $A(\beta_l)$ is then the expected value of $z(x)$ multiplied by $z(x + \beta_l)$ (see Spragg and Whitehouse, 1970/71), where β_l is shift parameter, viz.

$$\begin{aligned} A(\beta_l) &= E[z(x)z(x + \beta_l)] \\ &= \lim_{\Delta L \rightarrow \infty} \frac{1}{\Delta L} \int_{-\Delta L/2}^{\Delta L/2} z(x)z(x + \beta_l)dx \\ &= \frac{1}{2\pi} \int_{-\infty}^{\infty} P(\omega) \cos \omega \beta_l d\omega \end{aligned} \quad (\text{C.5})$$

where $P(\omega)$ is the power density spectral density, $\omega = 2\pi/\lambda$.

Differentiating the autocorrelation function twice with respects to β_l gives

$$A''(\beta_l) = -E[z'(x)z'(x + \beta_l)] = -\frac{1}{2\pi} \int_{-\infty}^{\infty} \omega^2 P(\omega) \cos \omega \beta_l d\omega. \quad (\text{C.6})$$

In particular, for $\beta_l = 0$, from Eqs. (C.6) and (C.6) there exist

$$A(0) = E[z(x)^2] = z(x)_{r.m.s.}^2 \quad (C.7)$$

and

$$A''(0) = -E[z'(x)^2] = -z'(x)_{r.m.s.}^2 \quad (C.8)$$

Thus, the mean square angular frequency $\omega_{r.m.s.}^2$ is given by

$$\omega_{r.m.s.}^2 = \frac{\frac{1}{2\pi} \int_{-\infty}^{\infty} \omega^2 P(\omega) \cos \omega \beta_l d\omega}{\frac{1}{2\pi} \int_{-\infty}^{\infty} P(\omega) \cos \omega \beta_l d\omega} \quad (C.9)$$

From the relation of $\omega_{r.m.s.} = 2\pi/\lambda_{r.m.s.}$, Eq. (C.9) becomes

$$\lambda_{r.m.s.} = 2\pi \frac{1}{\omega_{r.m.s.}} = 2\pi \frac{z(x)_{r.m.s.}}{z'(x)_{r.m.s.}} \quad (C.10)$$

For practical purpose average values, R_a and λ_a , rather than r.m.s. may be used since the differences of results are small.

From Eq. (C.9), a clear physical interpretation of the average wavelength is obtained from the ratio of second moment of power spectrum of the profile to the profile itself. Therefore, the average wavelength measures the spatial undulating of the surface.

The average wavelength gives a quantitative basis for specifying the sharpness of the surface texture with respect to average height. For instance, for a surface during a running-in operation, the changing of the surface is not obvious from the measurement of surface

¹r.m.s. = root mean square

average roughness. But this changing can be noticeably identified from the change in average wavelength.

For the profile shown in Fig. 6.1, calculations by discrete values from the measurement give a measure of surface roughness of the bearing pad, via average slope $\Delta_a = 5.58^\circ$, average roughness $R_a = 0.73 \mu\text{m}$ (not magnified), root-mean-square roughness $R_q = 0.912 \mu\text{m}$, average wavelength $\lambda_a = 52.2 \mu\text{m}$, steepness $\gamma = R_a/\lambda_a = 0.73/52.2 = 0.014$. For comparison, from the reference (Spragg and Whitehouse, 1970/71), the average wavelength of sheet steel of auto-body is about $200 - 350 \mu\text{m}$, while its average roughness is around $2 \mu\text{m}$. This would give a quantitative range of R_a , λ_a for engineering finishing surfaces.

Appendix D

Coefficients of Matrices in FEM

This appendix lists all coefficients included in the FEM formulation in Chapter 3, Numerical Solution for a Sinusoidally Wavy Wall. The expressions given are derived by the writer for an arbitrarily shaped element of the mesh.

[A] is a short form of the right hand side of Eq. (D.1).

[D] is the pressure mass matrix; [L] is the pressure related matrix, [S] comes from the viscous term, and [N] comes from the convective term.

$$[\hat{A}] = [\hat{S}] + \frac{1}{\beta} [L_{11}]^T [D_{11}]^{-1} [L_{11}] \quad (\text{D.1})$$

$$[D_{11}] = \int_{-1}^1 \int_{-1}^1 |J| d\xi d\eta \quad (\text{D.2})$$

$$[D_{12}] = [D_{21}] = [D_{22}] = 0$$

$$\begin{aligned} [L_{11}(\psi_1)]_{,x} &= - \int_{\Omega_e} \frac{\partial \phi_i}{\partial x} \psi_1 d\Omega \\ &= - \int_{-1}^1 \int_{-1}^1 |J| \psi_1 \left[\frac{\partial \phi_i}{\partial \xi} \frac{\partial \xi}{\partial x} + \frac{\partial \phi_i}{\partial \eta} \frac{\partial \eta}{\partial x} \right] d\xi d\eta \end{aligned} \quad (\text{D.3})$$

$$\begin{aligned}
 [L_{11}(\psi_1)]_{,z} &= - \int_{\Omega_e} \frac{\partial \phi_i}{\partial z} \psi_1 d\Omega \\
 &= - \int_{-1}^1 \int_{-1}^1 |J| \psi_1 \left[\frac{\partial \phi_i}{\partial \xi} \frac{\partial \xi}{\partial z} + \frac{\partial \phi_i}{\partial \eta} \frac{\partial \eta}{\partial z} \right] d\xi d\eta
 \end{aligned} \tag{D.4}$$

$$\begin{aligned}
 [L_{21}(\psi_2)]_{,x} &= - \int_{\Omega_e} \frac{\partial \phi_i}{\partial x} \psi_2 d\Omega \\
 &= - \int_{-1}^1 \int_{-1}^1 |J| \psi_2 \left[\frac{\partial \phi_i}{\partial \xi} \frac{\partial \xi}{\partial x} + \frac{\partial \phi_i}{\partial \eta} \frac{\partial \eta}{\partial x} \right] d\xi d\eta
 \end{aligned} \tag{D.5}$$

$$\begin{aligned}
 [L_{21}(\psi_2)]_{,z} &= - \int_{\Omega_e} \frac{\partial \phi_i}{\partial z} \psi_2 d\Omega \\
 &= - \int_{-1}^1 \int_{-1}^1 |J| \psi_2 \left[\frac{\partial \phi_i}{\partial \xi} \frac{\partial \xi}{\partial z} + \frac{\partial \phi_i}{\partial \eta} \frac{\partial \eta}{\partial z} \right] d\xi d\eta
 \end{aligned} \tag{D.6}$$

$$\begin{aligned}
 [L_{21}(\psi_3)]_{,x} &= - \int_{\Omega_e} \frac{\partial \phi_i}{\partial x} \psi_3 d\Omega \\
 &= - \int_{-1}^1 \int_{-1}^1 |J| \psi_3 \left[\frac{\partial \phi_i}{\partial \xi} \frac{\partial \xi}{\partial x} + \frac{\partial \phi_i}{\partial \eta} \frac{\partial \eta}{\partial x} \right] d\xi d\eta
 \end{aligned} \tag{D.7}$$

$$\begin{aligned}
 [L_{21}(\psi_3)]_{,z} &= - \int_{\Omega_e} \frac{\partial \phi_i}{\partial z} \psi_3 d\Omega \\
 &= - \int_{-1}^1 \int_{-1}^1 |J| \psi_3 \left[\frac{\partial \phi_i}{\partial \xi} \frac{\partial \xi}{\partial z} + \frac{\partial \phi_i}{\partial \eta} \frac{\partial \eta}{\partial z} \right] d\xi d\eta
 \end{aligned} \tag{D.8}$$

$$[L_{22}(1,1)] = - \int_{\Omega_e} \frac{\partial \phi_9}{\partial x} \psi_2 d\Omega = \int_{\Omega_e} \phi_9 d\Omega = \int_{-1}^1 \int_{-1}^1 |J| \phi_9(\xi, \eta) d\xi d\eta \tag{D.9}$$

$$[L_{22}(2,2)] = [L_{22}(1,1)] \tag{D.10}$$

$$[L_{22}(1,2)] = [L_{22}(2,1)] = 0 \tag{D.11}$$

$$[N_{uu,n,n}] = \sum_{k=1}^N u_k \int_{\Omega} \phi_m \phi_n \frac{\partial \phi_k}{\partial x} d\Omega \tag{D.12}$$

$$= \sum_{k=1}^N u_k \int_{-1}^1 \int_{-1}^1 |J| \phi_m \phi_n \left(\frac{\partial \phi_k}{\partial \xi} \frac{\partial \xi}{\partial x} + \frac{\partial \phi_k}{\partial \eta} \frac{\partial \eta}{\partial x} \right) d\xi d\eta$$

$$[N_{uw,n,n}] = \sum_{k=1}^N u_k \int_{\Omega} \phi_m \phi_n \frac{\partial \phi_k}{\partial z} d\Omega \tag{D.13}$$

$$= \sum_{k=1}^N u_k \int_{-1}^1 \int_{-1}^1 |J| \phi_m \phi_n \left(\frac{\partial \phi_k}{\partial \xi} \frac{\partial \xi}{\partial z} + \frac{\partial \phi_k}{\partial \eta} \frac{\partial \eta}{\partial z} \right) d\xi d\eta$$

$$[N_{wu,n,n}] = \sum_{k=1}^N w_k \int_{\Omega} \phi_m \phi_n \frac{\partial \phi_k}{\partial x} d\Omega \tag{D.14}$$

$$\begin{aligned}
&= \sum_{k=1}^N w_k \int_{-1}^1 \int_{-1}^1 |J| \phi_m \phi_n \left(\frac{\partial \phi_k}{\partial \xi} \frac{\partial \xi}{\partial x} + \frac{\partial \phi_k}{\partial \eta} \frac{\partial \eta}{\partial x} \right) d\xi d\eta \\
[N_{ww,n,n}] &= \sum_{k=1}^N w_k \int_{\Omega} \phi_m \phi_n \frac{\partial \phi_k}{\partial z} d\Omega \\
&= \sum_{k=1}^N w_k \int_{-1}^1 \int_{-1}^1 |J| \phi_m \phi_n \left(\frac{\partial \phi_k}{\partial \xi} \frac{\partial \xi}{\partial z} + \frac{\partial \phi_k}{\partial \eta} \frac{\partial \eta}{\partial z} \right) d\xi d\eta
\end{aligned} \tag{D.15}$$

$$[N_{uu,m,n}] = \sum_q (N_u)_{mnq} u_q \tag{D.16}$$

$$[N'] = \{(N_u)_{mnp} u_n + (N_w)_{mnp} w_n\} \begin{bmatrix} 1 & 0 \\ 0 & 1 \end{bmatrix} \tag{D.17}$$

$$\begin{aligned}
[S_{uu,m,n}] &= \int_{\Omega_e} \nabla \phi_m \nabla \phi_n d\Omega \\
&= \int_{\Omega_e} \left(\frac{\partial \phi_m}{\partial x} \frac{\partial \phi_n}{\partial x} + \frac{\partial \phi_m}{\partial z} \frac{\partial \phi_n}{\partial z} \right) d\Omega \\
&= \int_{-1}^1 \int_{-1}^1 |J| \left[\left(\frac{\partial \phi_m}{\partial \xi} \frac{\partial \xi}{\partial x} + \frac{\partial \phi_m}{\partial \eta} \frac{\partial \eta}{\partial x} \right) \left(\frac{\partial \phi_n}{\partial \xi} \frac{\partial \xi}{\partial x} + \frac{\partial \phi_n}{\partial \eta} \frac{\partial \eta}{\partial x} \right) \right. \\
&\quad \left. + \left(\frac{\partial \phi_m}{\partial \xi} \frac{\partial \xi}{\partial z} + \frac{\partial \phi_m}{\partial \eta} \frac{\partial \eta}{\partial z} \right) \left(\frac{\partial \phi_n}{\partial \xi} \frac{\partial \xi}{\partial z} + \frac{\partial \phi_n}{\partial \eta} \frac{\partial \eta}{\partial z} \right) \right] d\xi d\eta
\end{aligned} \tag{D.18}$$

$$[S_{vv,m,n}] = [S_{uu,m,n}] \tag{D.19}$$

where, m = 1, ..., M; M = total number of weight functions, n = 1, ..., N; N = total number of velocity component number.

Jacobian Matrix

$$\begin{Bmatrix} \frac{\partial \phi_i}{\partial \xi} \\ \frac{\partial \phi_i}{\partial \eta} \end{Bmatrix} = \begin{bmatrix} \frac{\partial x}{\partial \xi} & \frac{\partial z}{\partial \xi} \\ \frac{\partial x}{\partial \eta} & \frac{\partial z}{\partial \eta} \end{bmatrix} = \begin{Bmatrix} \frac{\partial \phi_i}{\partial x} \\ \frac{\partial \phi_i}{\partial z} \end{Bmatrix} = [J] \begin{Bmatrix} \frac{\partial \phi_i}{\partial x} \\ \frac{\partial \phi_i}{\partial z} \end{Bmatrix} \tag{D.20}$$

where, for a 9-node quadrilateral element,

$$x = \sum_{j=1}^9 x_j \phi_j(\xi, \eta) \quad z = \sum_{j=1}^9 z_j \phi_j(\xi, \eta) \quad (\text{D.21})$$

$$\frac{\partial x}{\partial \xi} = \sum_{j=1}^9 x_j \frac{\partial \phi_j}{\partial \xi} \quad \frac{\partial z}{\partial \xi} = \sum_{j=1}^9 z_j \frac{\partial \phi_j}{\partial \xi} \quad (\text{D.22})$$

$$\frac{\partial x}{\partial \eta} = \sum_{j=1}^9 x_j \frac{\partial \phi_j}{\partial \eta} \quad \frac{\partial z}{\partial \eta} = \sum_{j=1}^9 z_j \frac{\partial \phi_j}{\partial \eta} \quad (\text{D.23})$$

The shape functions for velocity (ϕ_1 through ϕ_9) are listed as follows for reference only:

$$\phi_1 = \frac{(1-\eta)\eta(1-\xi)\xi}{4} \quad (\text{D.24})$$

$$\phi_2 = -\frac{(1-\eta)\eta(1-\xi)(\xi+1)}{2}$$

$$\phi_3 = -\frac{(1-\eta)\eta\xi(\xi+1)}{4}$$

$$\phi_4 = \frac{(1-\eta)(\eta+1)\xi(\xi+1)}{2}$$

$$\phi_5 = \frac{\eta(\eta+1)\xi(\xi+1)}{4}$$

$$\phi_6 = \frac{\eta(\eta+1)(1-\xi)(\xi+1)}{2}$$

$$\phi_7 = -\frac{\eta(\eta+1)(1-\xi)\xi}{4}$$

$$\phi_8 = -\frac{(1-\eta)(\eta+1)(1-\xi)\xi}{2}$$

$$\phi_9 = (1-\eta)(\eta+1)(1-\xi)(\xi+1)$$

The shape functions for pressure (ψ_1 through ψ_3) in terms of x/z-coordinates can be transferred to η/ξ -coordinates with the substitutions:

$$\psi_1 = 1 \quad (D.25)$$

$$\psi_2 = 1 - x_9$$

$$\psi_3 = 1 - z_9$$

Appendix E

Mesh Consideration

The accuracy of a FEM solution is determined not only by the model and the choice of interpolation function, but also by the fineness of the mesh used. In order to obtain solutions for the present problem which are relatively insensitive to grid size, an effort was made to find the optimum arrangement amongst three different meshes with 288, 480, and 720 elements termed, respectively, A, B, and C.

A comparison is given at Table E.1¹ for the situation $\epsilon = 0.3$, $\gamma = 0.3$, and $Re^* = 1.0$. This case involves maximum values of these three parameters in the numerical calculation and hence turns out to be a typical example.

For meshes A to C, the mesh size in the x -direction remains unchanged, while the mesh size in the z -direction continuously decreases. At the deepest station of one wavelength, the grid points for mesh A, B, C are, respectively, 3, 7, 12. Comparison of velocity profiles

¹The time cited in the table is referred to SUN SPARC Server 10 Model 512.

Mesh	Number of elements	Number of nodes	Number of unknowns	Grid points in x	Grid points in z	Time (s) per iteration
A	288 (6×48)	1261	1946	33	13	42
B	480 (10×48)	2037	3114	33	21	103
C	720 (15×48)	3007	4574	33	31	208

Table E.1: Mesh consideration

among three meshes shows that there is less than 0.9% difference of the largest value of velocity between mesh A, and mesh C and 0.3% between mesh B and mesh C. If the results from the finest mesh C are assumed to represent the accurate solution, then the resulting average shear stress deduced from the coarse mesh A would be under-estimated the values on the wavy wall, and be over-estimated on the flat wall. However, the differences of the average shear stress on both walls is 1.6% between mesh B and mesh C, while it is 6.6% between mesh A and mesh C.

Based on the above considerations, mesh B was chosen for all calculations of the study since it offers the acceptable accuracy at reasonable computing time.

Appendix F

ASME Paper No. 96-Trib-15

141

Jin Hu

Hans J. Leutheusser

Department of Mechanical and Industrial
Engineering,
University of Toronto,
Toronto, Ontario, M5S 3G8, Canada

Micro-Inertia Effects in Laminar Thin-Film Flow Past a Sinusoidal Boundary

Micro-inertia effects of surface roughness on hydrodynamic lubrication are analyzed in the light of similitude principles, viz. a newly conceived reduced Reynolds number and the classical parameter of relative roughness. In particular, the dynamic properties of laminar sheet flow in a two-dimensional channel between a sinusoidal wall and a flat wall are studied. FEM solutions of the Navier-Stokes equation are compared with corresponding experimental findings. The latter are gathered in an especially designed laminar-flow wind tunnel. Conclusions are drawn concerning the roughness sensitivity of laminar thin-film flows.

1 Introduction

The analysis of bearing performance is traditionally based on the solution of the Reynolds equation of hydrodynamic lubrication, which assumes the bearing surfaces to be physically smooth. However, the current trend toward increasing bearing loads causes the lubricating fluid films to become thinner, the film thickness may become comparable to the size of the surface asperities.

In moving about the surface irregularities, streamlines lose their straight alignment. The resulting tortuous flow is subjected to convective accelerations on a microscopic level which are distinctly different from the macroscopic phenomena entailed by changes in the global flow geometry. The micro-convective inertia effects of surface roughness thus violate several of the underlying assumptions of the classical Reynolds equation and may even render it invalid.

It is beginning to be recognized that the tribological performance of bearings under thin fluid film conditions is dependent to some degree upon their surface topography. It is, hence, of a considerable economic importance to establish guidelines for selecting a suitable surface texture and the extent of a required machining process since unnecessary surface finishing operations are a major cause of excessive manufacturing cost.

In order to describe the effects of roughness on thin-film lubrication, tribologists have so far developed three theoretical approaches for obtaining a suitably modified Reynolds equation, or a solution thereof. Christensen (1969) developed a general stochastic model; Patir and Cheng (1978) introduced an average flow model; and Elrod (1979) solved the classical Reynolds equation for rough surfaces by a perturbation method. Cheng (1984) provided an update review of work on this topic. In contrast to a large number of theoretical papers, there are only few pertinent experiments reported in the literature available. Friction coefficient variations for different rough surfaces were measured using a test pad on a glass disc apparatus by Hata et al. (1980). Jeng (1990) developed a computer-aided pin-on-disc tribometer measuring the friction of the testing samples of rough surfaces and also showed some observations of flow visualization. The optical interferometry technique was extended to examine the effects of surface roughness on EHL by Tønder and Jakobsen (1992) and Kaneta et al. (1993), respectively. However, for the above experimental studies, there

is no sufficient experimental data to directly support the existing theoretical models.

Clearly, the problem of laminar flow between rough surfaces has not yet been satisfactorily solved. The present, currently ongoing research introduces a new view of the roughness phenomenon by focusing attention on the micro-inertia effects of surface texture. To this end, a unilaterally rough plane-Poiseuille flow is considered, and wall roughness is varied from, initially, a regular pattern to, eventually, a completely arbitrary arrangement as typically encountered in industry. This paper reports on work relating to a case of two-dimensional sinusoidal surface roughness, and compares numerical results obtained from a solution of the Navier-Stokes equation with corresponding experimental findings.

2 Governing Equations and Dimensionless Parameters

A thin-film (two-dimensional) channel flow between two smooth surfaces is schematically depicted in Fig. 1(a) where U is the average velocity in streamwise direction. The film thickness, h , is significantly smaller than the longitudinal dimension, ΔL , say $O(10^{-3})$. Under bearing conditions, i.e., with the two surfaces forming a load-sustaining fluid wedge, this feature permits to drop the (macroscopic) inertia terms in the Navier-Stokes equation and, hence, leads to the establishment of the classical Reynolds equation.

However, with decreasing film thickness, the magnitude of any surface roughness becomes closer to that of the film thickness, and the assumption of a physically smooth surface does not hold true any longer. Therefore, the real flow situation may be represented more closely by Fig. 1(b) where some arbitrary, albeit two-dimensional roughness is described by the parameters of average height R_s and average wavelength λ_r . The corresponding length parameters for the global flow are now h_0 , the nominal film thickness, and ΔL , a characteristic length in streamwise direction.

The governing equations for steady, laminar, incompressible Newtonian flow in the x/z -plane are

$$\frac{\partial u}{\partial x} + \frac{\partial w}{\partial z} = 0 \quad (1)$$

$$u \frac{\partial u}{\partial x} + w \frac{\partial u}{\partial z} = - \frac{1}{\rho} \frac{\partial p}{\partial x} + \nu \frac{\partial^2 u}{\partial x^2} + \nu \frac{\partial^2 u}{\partial z^2} \quad (2)$$

$$u \frac{\partial w}{\partial x} + w \frac{\partial w}{\partial z} = - \frac{1}{\rho} \frac{\partial p}{\partial z} + \nu \frac{\partial^2 w}{\partial x^2} + \nu \frac{\partial^2 w}{\partial z^2} \quad (3)$$

Contributed by the Tribology Division of THE AMERICAN SOCIETY OF MECHANICAL ENGINEERS and presented at the ASME/STLE Joint Tribology Conference, San Francisco, Calif., October 13–17, 1996. Manuscript received by the Tribology Division February 18, 1996; revised manuscript received June 14, 1996. Paper No. 96-Trib-15. Associate Technical Editor: K. Tønder.

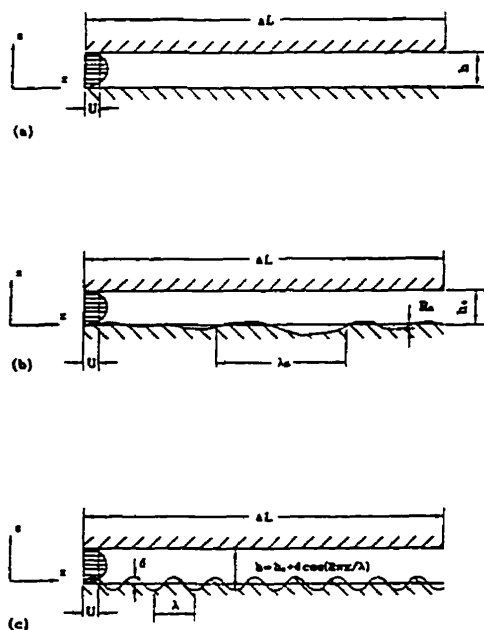


Fig. 1 Definition diagrams. (a) Thin-film channel flow between smooth walls; (b) thin-film channel flow with an arbitrarily rough wall; (c) thin-film channel flow with a sinusoidally wavy wall.

where, $\nu = \mu/\rho$ = kinematic viscosity of lubricant, ρ = density of lubricant, and u and w = velocity components in x and z directions, respectively.

For the situation depicted in Fig. 1(b) there are two significant length scales, i.e., the average wavelength of the roughness, λ_a , in streamwise direction, and the average height of the roughness, R_a , in transverse direction (with R_a generally much smaller than λ_a). The corresponding velocity scales in x and z directions are U and $R_a/\lambda_a U$, respectively.

In terms of nondimensional variables, viz. x/λ_a , z/R_a , u/U , $w/(UR_a/\lambda_a)$, $p/\rho U^2$, Eqs. (2) and (3), become:

$$Re^* \left(u \frac{\partial u}{\partial x} + w \frac{\partial u}{\partial z} + \frac{\partial p}{\partial x} \right) = \frac{R_a^2 \partial^2 u}{\lambda_a^2 \partial x^2} + \frac{\partial^2 u}{\partial z^2} \quad (4)$$

$$Re^* \left(u \frac{\partial w}{\partial x} + w \frac{\partial w}{\partial z} + \frac{\lambda_a^2 \partial p}{R_a^2 \partial z} \right) = \frac{R_a^2 \partial^2 w}{\lambda_a^2 \partial x^2} + \frac{\partial^2 w}{\partial z^2} \quad (5)$$

where all terms are now understood to be nondimensional. The parameter

$$Re^* = UR_a^2/(\nu \lambda_a) \quad (6)$$

in these equations may be called the reduced (micro-inertial)

Reynolds number. It represents the ratio of micro-inertial forces due to roughness to viscous forces, and is the appropriate scaling parameter for assuring dynamic similarity between comparable physical situations.

If, in lieu of R_a , the nominal film thickness were chosen as the transverse scaling unit (ΔL should then be used for the streamwise direction) the conventional reduced (macroscopic) Reynolds number would be

$$Re^{**} = Uh_0/(\nu \Delta L). \quad (7)$$

The two reduced Reynolds numbers, viz. Eqs. (6) and (7), measure inertia forces in different regions of the flow. The conventional definition, i.e., Re^{**} , corresponds to the whole macroscopic flow field, while Re^* refers to the micro-inertial effects of the asperities. The latter is the principal concern of the present research.

In addition, of course, there can always be defined an overall, or bulk Reynolds number

$$Re = \frac{2Uh_0}{\nu} \quad (8)$$

which determines the state, i.e., laminar or turbulent, of the flow. In Eq. (8), $2h_0$ is the equivalent diameter of a wide rectangular channel, and the flow is laminar (i.e., plane-Poiseuille flow) when Re is less than about 2000.

It is the objective of the present investigation to determine when and how micro-inertia affects thin laminar film flow. To this end, flow situations are analyzed over ranges of bulk Reynolds number Re , reduced Reynolds number Re^* , and a geometric similarity parameter relating the size of the roughness to the size of the flow, viz. the relative roughness

$$\epsilon = \frac{R_a}{h_0}. \quad (9)$$

Differences are sensed in terms of characteristics, such as the Darcy-Weisbach friction coefficient

$$f = 8 \frac{\tau_w}{\rho U^2} = 4 \frac{h_0}{\Delta L} \frac{\Delta p}{\rho U^2} \quad (10)$$

where τ_w = wall shear stress, and Δp = pressure drop over ΔL . Typical findings for one particular roughness pattern, viz. unilateral sinusoidal corrugations, are presented in the following.

3 Experimental Setup

The experiments are performed in an especially designed, essentially two-dimensional air duct, or wind tunnel, of adjustable depth, 50 cm width, and 4 meter length (Hu and Leutheusser, 1994). Flow is produced by a variable-speed cross-flow air blower discharging into a large stilling chamber and thence, by way of a honeycomb composed of tightly packed drinking straws, into the duct proper. The top wall of the duct is arranged in such a way that the depth of the flow cross-section can be

Nomenclature

f = Darcy-Weisbach friction coefficient	Re^* = reduced (micro-inertial) Reynolds number, $UR_a^2/(\nu \lambda_a)$ or $U\delta^2/(\nu \lambda)$	x, z = length coordinates, see in Fig. 1
$h(x)$ = film thickness	Re^{**} = conventional reduced (macroscopic) Reynolds number, $Uh_0/(\nu \Delta L)$	δ = amplitude of sinusoidal wave
h_0 = nominal film thickness	u, w = velocity components in x and z directions, respectively	ϵ = relative roughness, R_a/h_0 or δ/h_0
ΔL = length of channel element	U = average velocity over flow cross-section	λ = wavelength of sinusoidal wave
p = pressure		λ_a = average wavelength of arbitrary roughness
Δp = pressure drop		μ = dynamic viscosity
R_a = average height of roughness		ν = kinematic viscosity
Re = bulk Reynolds number, $2Uh_0/\nu$		ρ = fluid density
		τ_w = wall shear stress

readily changed from zero to about 5 cm. The plywood bottom of the duct carries the surface texture to be investigated in the form of square tiles measuring 25 cm by 25 cm. Each set of tiles, made of plaster of Paris, is cast from a precisely machined master mould. For the relevant case of a sinusoidally wavy wall a total of $2 \times 16 = 32$ tiles, each modeling a two-dimensional wave of 3 mm amplitude and 250 mm length, are arranged in two parallel rows to form a uniformly corrugated surface with striations normal to the direction of flow.

During the tests the Reynolds number Re is monitored by a hot-film probe near the outlet from the honeycomb. The bulk of the studies is performed near the exit from the wind tunnel proper to ensure existence of fully developed flow. Because of the low velocities encountered in laminar air flow, all rate measurements are carried by hot-wire anemometry using both single and x-wire probes. Probe calibration is performed on a rotating table equipped with computer control and data acquisition system.

Flow visualization is realized by the smoke-wire technique employing a high energy pulse generator to heat an oil-covered nickel-chromium wire. The latter is placed vertically in the centre plane of the wind tunnel one meter upstream from the outlet, and observations of the pulsed smoke plume are recorded by both still photography and video cinematography.

4 Finite Element Solutions for Sinusoidal Wall

A general solution of the governing equations can, of course, not be obtained for randomly rough surfaces. However, if it is postulated that an arbitrary two-dimensional surface is, in first, crude approximation composed of a multitude of sinusoidal wave-forms, each of different amplitude and wave length, then some useful information may be extracted from the mathematically tractable solution of a single wave train with amplitude $\delta = R_s$ and wave length $\lambda = \lambda_s$, cf. Fig. 1(c).

To this end, Eqs. (4), (5), and (1) were solved using the Newton-Raphson method and employing the Crouzeix-Raviart element (Cavelier and Steenhoven, 1986), which works very well since it complies with the penalty function. To achieve automatic generation of the mesh system, the whole domain area of one wavelength was divided along the z -axis into two parts: the first part extended between sinusoidal wall and one third of the channel height, with the mesh size increasing in geometrical progression; the balance of the area was discretized into rectangles. A typical 9-node Crouzeix-Raviart element was applied. In the present calculations, various mesh systems were used. The coarsest one had 96 (16×6 , numbers of divisions in x and z directions, respectively) elements, and the finest had 400 (20×20) for one wavelength. Since a curved boundary was involved, the nonrectangular elements were mapped into rectangular ones in terms of local coordinates using Jacobian matrices.

The applicable boundary conditions were the Neumann condition on both walls, parabolic distribution of the streamwise (u) velocity at the inlet, and fully developed periodicity at the exit from the thin-film flow channel. The first attempt of numerical calculation was carried out for only one single wavelength. This proved to be unsatisfactory for the periodical boundary condition and, hence, all subsequent numerical results were based on a flow field containing three wavelengths.

5 Results and Discussion

5.1 Numerical Findings. As a test example, plane-Poiseuille flow between smooth walls was solved using the program and mesh described in the foregoing. Various ratios of entrance length to height of channel were tried until the velocity distribution was found to be parabolic. With 400 (20×20) elements, a ratio of entrance length to height of channel of equal to 10.



(a)



(b)



(c)

Fig. 2 Video images of smoke-wire streaklines for sinusoidal wall, at $x = \lambda$, for $Re^* = 2.15$, $\epsilon = 0.15$, ($Re = 1,195$). The time difference between exposures is $\frac{1}{30}$ of a second.

and $Re = 100$, the maximum absolute error of velocity between exact and numerical results was found to be less than 10^{-5} . Also, the Darcy-Weisbach friction coefficient agreed with the theoretical plane-Poiseuille value of $f = 96/Re$ with an error smaller than 10^{-4} .

For the flow between a flat wall and a sinusoidal wavy ones, the above numerical procedure always converged to a normalized residue sum for all flow variables of below 10^{-4} when the Newton-Raphson iteration was repeated several times. In cases where this was not so the Stokes solution and the Picard iteration were used in order to obtain closer initial values.

Calculations were carried out over the following ranges of the governing parameters, viz., bulk Reynolds number $Re = 10$ to 1500; reduced micro-inertial Reynolds number $Re^* = 0.01$ to 3.00; and relative roughness $\epsilon = 0.01$ to 0.3.

5.2 Experimental Verification of Numerical Solutions. Figure 2 shows typical streakline profiles, made visible by the smoke-wire technique, for flow past a sinusoidally wavy wall. The time difference between the three exposures is $\frac{1}{30}$ of a second. The corresponding velocity profile follows from the distance traveled by the smoke particles between two exposures and the intervening time period.

Video images of smoke-wire streaklines at different streamwise positions are displayed in Fig. 3. These profiles were recorded at a setting of $h_0 = 15$ mm and $U = 0.45$ m/s, equivalent

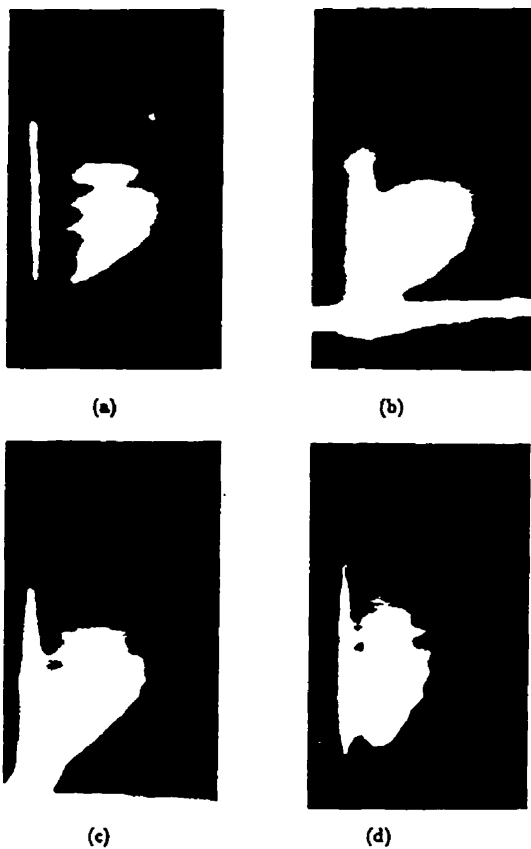


Fig. 3 Video images of smoke-wire streaklines for sinusoidal wall at various streamwise positions, viz. (a) $x = 0$, (b) $x = \frac{1}{2}\lambda$, (c) $x = \frac{1}{3}\lambda$, (d) $x = \frac{3}{2}\lambda$, for $Re^* = 2.15$ and $\epsilon = 0.2$ ($Re = 894$).

to $Re^* = 2.15$, $Re = 894$, and $\epsilon = 0.2$. The corresponding velocity vector plot, obtained from hot-wire anemometer measurements, is shown in Fig. 4. There is overall agreement although heat convection effects may be noticed in Figs. 3(b) and 3(c) due to the relative small velocity at the bottom of these two positions.

Figure 5 presents a comparison of velocity profiles at $x = \lambda/2$ obtained by both numerical and experimental methods, for $Re = 1.218$, $Re^* = 2.19$, $\epsilon = 0.15$, and $h_0 = 15$ mm. Agreement between the numerical solution and the hot-wire anemometer readings is very good, confirming in effect the former, but the profile predicted with the aid of the smoke-wire technique is more qualitatively than quantitatively acceptable. Nevertheless, the smoke-wire technique is certainly useful by providing a visible flow pattern.

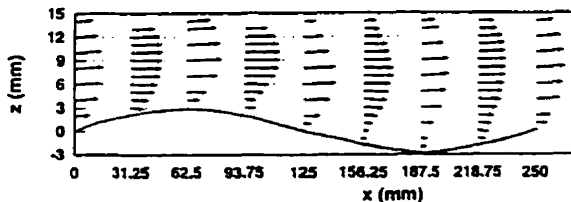


Fig. 4 Velocity vector plot obtained by hot-wire anemometer for $Re^* = 2.15$ and $\epsilon = 0.2$ ($Re = 894$)

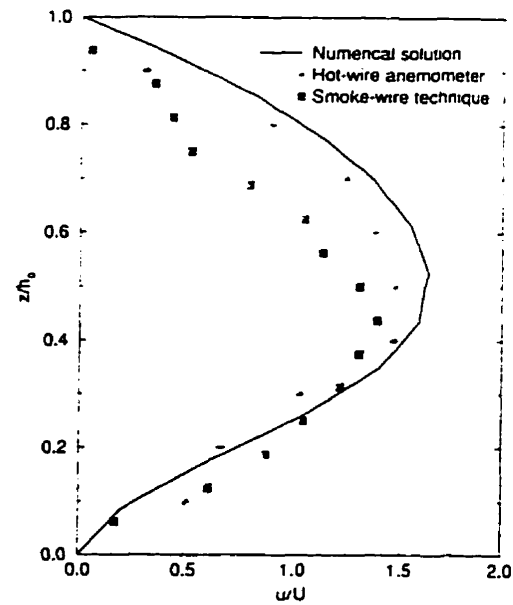


Fig. 5 Comparison of velocity profiles obtained by different methods at $x = \frac{1}{2}\lambda$, for $Re^* = 2.19$ and $\epsilon = 0.15$ ($Re = 1,218$)

5.3 Effects of Micro-Inertia. Figure 6 shows typical plots of the calculated velocity vector at $Re^* = 0.15$, 0.50, and 1.50, for $Re = 100$ and $\epsilon = 0.3$. With increasing Re^* , the flow becomes more tortuous, accordingly the velocity vectors in the proximity of the curved boundary depart more and move from the horizontal.

Figures 7 and 8 display the distributions of the velocity components u and w at minimum and maximum sections of the

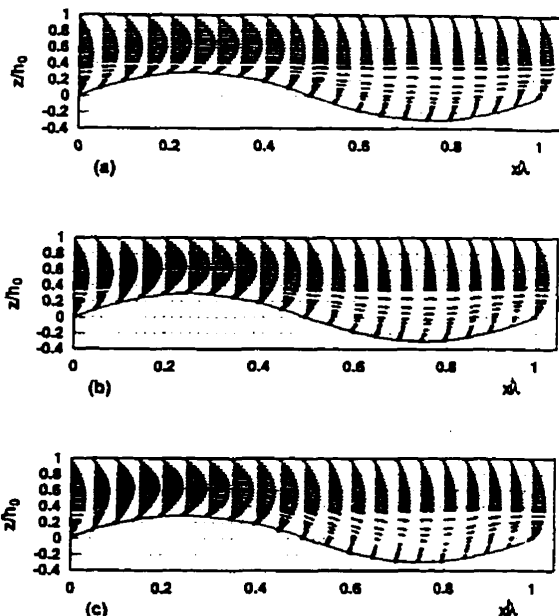


Fig. 6 Velocity profiles at various reduced micro-inertial Reynolds numbers viz. (a) $Re^* = 0.15$, (b) $Re^* = 0.50$, (c) $Re^* = 1.5$; for $Re = 100$ and $\epsilon = 0.3$.

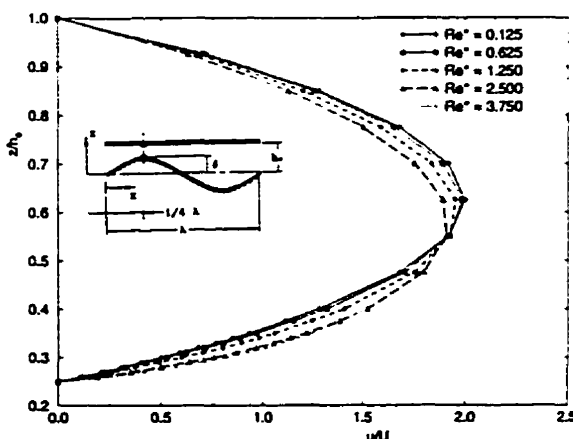


Fig. 7(a)

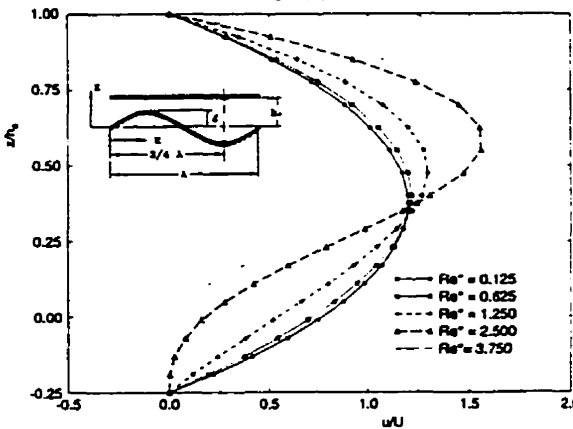


Fig. 7(b)

Fig. 7 Distribution of streamwise (u) velocity at various reduced micro-inertial Reynolds numbers Re^* , for $Re = 100$ and $\epsilon = 0.25$: (a) $x = \frac{1}{4}\lambda$; (b) $x = \frac{3}{4}\lambda$.

channel, i.e., at $x/\lambda = \frac{1}{4}$ and $x/\lambda = \frac{3}{4}$. As can be seen from Fig. 7(b), beyond some critical value of Re^* flow separation may occur at $x/\lambda = \frac{3}{4}$. On the other hand, at $x/\lambda = \frac{1}{4}$, see Fig. 7(a), micro-inertia tends to steepen the profile near the curved wall. Similar effects may also be seen in Figs. 8(a) and 8(b) which relate to the transverse (w) velocity. At low values of Re^* , the w -velocity has a small magnitude everywhere except in the immediate vicinity of the curved wall. And, of course, w is uniformly zero in the case of plane-Poiseuille flow.

5.4 Effects of Relative Roughness. In the engineering fluid mechanics of turbulent boundary shear flows the ratio of roughness height to, say, channel depth, called relative roughness, is known to be important. For the problem of thin-film laminar flow studied herein, this parameter, $\epsilon = \delta/h_0$, has a similarly significant effect on the flow properties. This is in distinct contrast to the conventional case of laminar flow in boundary layers and conduits. For a given texture, ϵ increases when the film thickness decreases although Re^* remains constant (for unchanging U). Figures 9(a), and 9(b) show streamwise distributions of the non-dimensional shear stress over a wavelength for a range of ϵ -values along the wavy wall (a) and along the flat wall (b). From these curves, for $Re = 50$, the marked influence of relative roughness on the magnitude of

the local shear stress can be clearly seen. The latter is defined by Eq. (11), viz.

$$\tau_w = \frac{\mu}{\cos(2\pi x/\lambda)} \frac{du}{dz} \quad (11)$$

where the velocity gradient occurs at the wall. There are noticeable differences between the wavy and the flat walls, and between the first and second half-cycles. These differences decrease with decreasing relative roughness and, for $\epsilon \rightarrow 0$, the shear stress tends toward the plane-Poiseuille value of

$$\tau_w = \frac{12}{Re} \frac{\nu}{U^2}. \quad (12)$$

6 Implications for Lubrication

6.1 Ranges for Re^* , Re , and ϵ Pertaining to Lubrication. The values for parameters Re^* , Re , and ϵ in Section 5 were mainly chosen within reasonable ranges of practical lubrication. For example, a 26.7 cm (10.5 in.) diameter thrust bearing operates at mean surface speed $U = 94.25$ m/s using light turbine oil (ISO VG 32) of kinematic viscosity $\nu = 31.8 \times 10^{-6}$

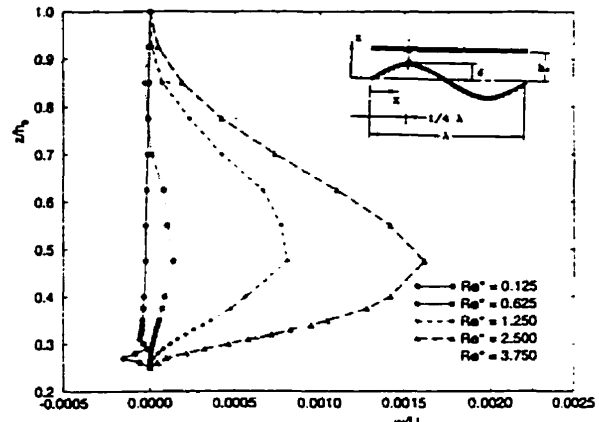


Fig. 8(a)

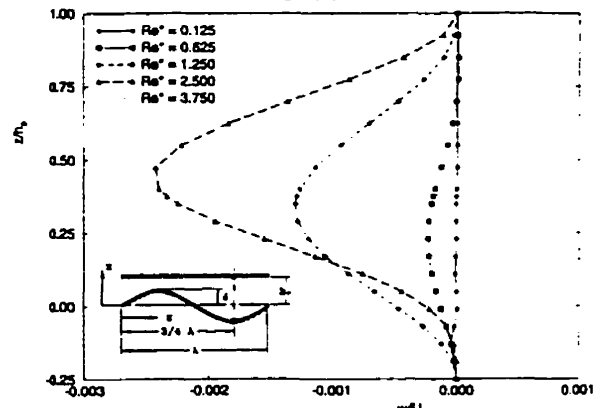


Fig. 8(b)

Fig. 8 Distribution of transverse (w) velocity at various reduced micro-inertial Reynolds numbers Re^* , for $Re = 100$ and $\epsilon = 0.3$: (a) $x = \frac{1}{4}\lambda$; (b) $x = \frac{3}{4}\lambda$.

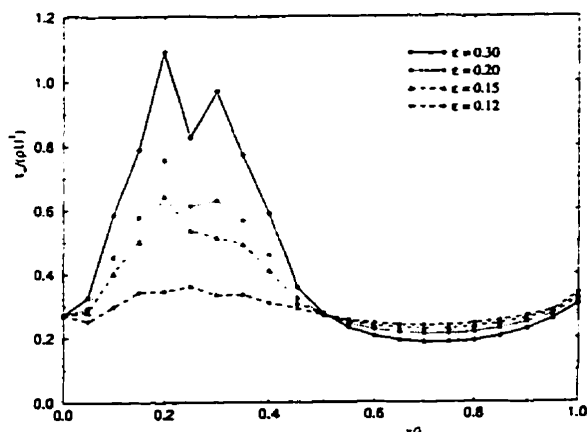


Fig. 9(a)

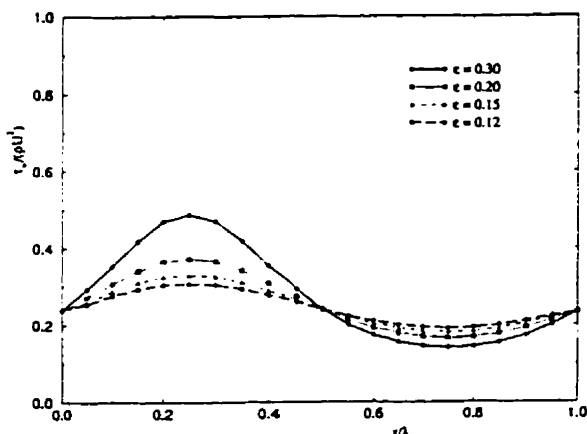


Fig. 9(b)

Fig. 9 Local shear stress over one wavelength at various values of relative roughness ϵ , for $Re = 50$: (a) along wavy wall; (b) along flat wall

m^2/s at $37.8^\circ C$ ($100^\circ F$), and $\nu = 5.5 \times 10^{-6} m^2/s$ at $98.9^\circ C$ ($210^\circ F$). For $\lambda_o = 50 \mu m$, $R_o = 1 \mu m$, and assuming $h_0 = 30 \mu m$, the flow is laminar ($Re = 178$ and 1030 , respectively); the reduced Reynolds number $Re^* = 0.059$ and 0.342 accordingly; $\epsilon = 0.033$. The lubricant working temperature is usually higher than $50^\circ C$ and the nominal film thickness decreases with increasing temperature. Therefore, the values of above parameters realistically pertain to practical lubrication.

6.2 Lubrication of Rough Surfaces. Analytical considerations sketched in the foregoing, and, guidance by experimental evidence, will make it possible to eventually identify the limiting conditions of applicability of the classical Reynolds equation, and to formulate a suitably modified version thereof. It is the objective of ongoing research work to extend the current approach to randomly rough surfaces and to develop suitable correction coefficients, from the measured velocity field over rough surface, for the Reynolds equation of lubrication.

7 Conclusions

The concept of micro-inertia in tortuous laminar flow about surface asperities in hydrodynamically lubricated bearings has been solidly linked to the principles of dynamic and geometric similitudes. The relevant parameters are, respectively, reduced (micro-inertial) Reynolds number Re^* and relative roughness ϵ . These two parameters are shown, both analytically and experimentally, to be significant for the case of a unilaterally wavy laminar thin-film flow. The present results encourage generalization of the concept of micro-inertia to other types of surface roughness.

Acknowledgment

The work described herein is supported by the Natural Sciences and Engineering Research Council of Canada.

References

- Cheng, H. S., 1984, "The Lubrication of Rough Surface," *Proc. the 11th Leeds-Lyon Symposium*, Dowson, D., Taylor, C. M., Godet, M., and Berthe, D., eds., Butterworths, pp. 11-20.
- Christensen, H., 1969-70, "Stochastic Models for Hydrodynamic Lubrication on Rough Surfaces," *Proc. Instn. Mech. Engrs.*, Vol. 184, Part I, No. 55, pp. 1013-1022.
- Cuvelier, S., and van Steenhoven, A. A., 1986, *Finite Element Methods and Navier-Stokes Equations*, D. Reidel, Hingham, MA.
- Eliod, H., 1979, "A General Theory for Laminar Lubrication with Reynolds Roughness," *ASME JOURNAL OF LUBRICATION TECHNOLOGY*, Vol. 101, pp. 8-14.
- Hara, H., Nakahara, T., and Aoki, H., 1980, "Measurement of Friction in Slightly Loaded Hydrodynamic Sliders with Striated Roughness," *Surface Roughness Effects in Hydrodynamic and Mixed Lubrication*, Rohde, S. M., and Cheng, H. S., eds., New York, pp. 75-92.
- Fu, J., and Leutheusser, H. J., 1994, "Fluid Film Lubrication Between Rough Surfaces," *Proceedings, 4th International Tribology Conference*, Stachowiak, G. W., ed., Perth, Western Australia, Vol. 2, pp. 637-639.
- Jeng, Y. R., 1990, "Experimental Study of the Effects of Surface Roughness on Friction," *STLE Tribology Transactions*, Vol. 33, pp. 403-410.
- Kaneta, M., Sakai, T., and Nishikawa, H., 1993, "Effects of Surface Roughness on Point Contact EHL," *STLE Tribology Transactions*, Vol. 36, pp. 605-612.
- Patir, N., and Cheng, H. S., 1978, "An Average Flow Model for Determining Effects of Three-Dimensional Roughness of Partial Hydrodynamic Lubrication," *ASME JOURNAL OF LUBRICATION TECHNOLOGY*, Vol. 100, No. 1, pp. 12-17.
- Serbetci, I., and Tichy, J. A., 1991, "Inertial Effects in Thin Film Flow With a Corrugated Boundary," *ASME Journal of Applied Mechanics*, Vol. 58, pp. 272-277.
- Tender, K., and Jakobsen, J., 1992, "Interferometric Studies of Effects of Striated Roughness on Lubricant Film Thickness Under Elastohydrodynamic Conditions," *ASME JOURNAL OF TRIBOLOGY*, Vol. 114, pp. 52-56.

Bibliography

- ARMALY, B.F., DURST, F., PEREIRA, J.C.F. & SCHÖNUNG, B., 1983, "Experimental and theoretical investigation of backward-facing step flow", *Journal of Fluid Mechanics*, **127**, pp. 473–496.
- AZZAM, M.I.S., AND DULLIEN, F.A.L., 1977, "Flow in Tubes with periodic step changes in diameter: a numerical solution", *Chem. Eng. Sci.*, **32**, pp. 1445–1455.
- AYDIN, E.M. AND LEUTHEUSSER, H.J., 1991, "Plane-Couette flow between smooth and rough walls", *Experiments in Fluids*, **11**, pp. 302–312.
- BEST, G.L., DECKERT, K.L.; MILLMAN, S.E. & SINGH G.P., 1988, "Effect of disk roughness on slider dynamics", *IEEE Transaction on Magnetics*, **24**, pp. 2748–2750.
- BRUUN, H.H., 1995, *Hot-Wire Anemometry, Principles and Signal Analysis*, Oxford University Press.
- CHENG, H.S., 1984, "The lubrication of rough surfaces", In: *Proc. of 11th Leeds-Lyon Symposium*, DOWSON, D; TAYLOR, C.M.; GODET, M. & BERTHE, D. (eds.), Butterworths, pp. 11–20.
- CHRISTENSEN, H., 1969/70, "Stochastic models for hydrodynamic lubrication on rough surfaces", *Proc. Instn. Mech. Engrs.*, **184** (Pt. 1, No. 55), pp. 1013–1022.
- CORKE, T.; KOGA, D.; DRUBKA, R. & NAGIB, H., 1977, "A new technique for in-

- troducing controlled sheets of smoke streaklines in wind tunnels”, IEEE Publication 77CH1251-8, pp. 74–79.
- CRC Handbook of Lubrication (Theory and Practice of Tribology)*, 1984, BOOSER, E.R., CRC Press Inc., Boca Raton, Florida.
- CRONE, R.M.; JHON, M.S.; BHUSHAN, B. & KARIS, T.E., 1991, “Modeling the flying characteristics of a rough magnetic head over a rough rigid-disk surface”, *Trans. ASME, Journal of Tribology*, **113**, pp. 739–749.
- CUVELIER, C.; SEGAL, A. & VAN STEENHOVEN, A.A., 1986, *Finite Element Methods and Navier-Stokes Equations*, D. Reidel Publishing Company, Dordrecht, Holland.
- DABNALL, H., 1980, *Exploring Surface Texture*, Rank Taylor Hobson, England.
- DE SILVA, G.M.S., LEATHER, J.A. & SAYLES, R.S, 1985, “The influence of surface topography on lubricant film thickness in an elastohydrodynamic (EHL) point contact”, In: *Proc. of 12th Leeds-Lyon Symposium*, DOWSON, D.; TAYLOR, C.M.; GODET, M. & BERTHE, D. (Eds.), Butterworths, pp. 258–272.
- DEIBER, J.A. & SCHOWALTER, W.R., 1979, “Flow Through Tubes with Sinusoidal Axial Variations in Diameter”, *AICHE Journal*, **25**, No. 4, pp. 638–645.
- DHATT, G. & TOUZOT, G., 1984, *The Finite Element Methods Displayed*, Chichester[West Sussex], New York:Wiley, pp. 284–286.
- DOWSON, D., 1979, *History of Tribology*, Longman, London and New York.
- DZIEDZIC, M., 1994, *An Experimental Study of Viscous Vortex Rings*. Ph.D. Thesis, Uni-

- versity of Toronto, Toronto, Canada.
- ETHIER, C.R., 1994, *Computational Fluid Mechanics and Heat Transfer*(MEC1210), Graduate Course Notes, Mechanical Engineering Department, University of Toronto, Toronto, Canada.
- ELROD, H.G., 1978, "A review of theories for the fluid dynamic effects of roughness on laminar lubricating films", In: *Proc. of 4th Leeds-Lyon Symposium of Tribology*, DOWSON, D.; TAYLOR, C.M.; GODET, M. & BERTHE, D. (eds.), Mechanical Engineering Publications Ltd., England, pp. 11-26.
- ELROD, H., 1979, "A general theory for laminar lubrication with Reynolds roughness", Trans. ASME, *Journal of Lubrication Technology*, **101**, pp. 8-14.
- GARTLING, D.K., NICKELL, R.E. & TANNER, R.I., 1977, "A finite element convergence study for accelerating flow problems", *International Journal for Numerical Methods in Engineering*, **11**, pp. 1155-1174.
- GARTLING, D.K., 1990, "A test problem for outflow boundary conditions - Flow over a backward-facing step", *International Journal for Numerical Methods in Fluids*, **11**, pp. 953-967.
- GERHART, P.M. & GROSS, R. J., 1985, *Fundamentals of Fluid Mechanics*, Addison-Wesley Publishing Company, Reading, Massachusetts.
- GREGORY, R.S., 1975, "Operating characteristics of a fluid-film thrust bearings subjected to high shaft speeds", *Proc. of 2nd Leeds-Lyon Symposium on Tribology*, Lyon, France,

- pp. 154–162.
- GROSS, W.A., MATSCH, L.A., CASTELLI, V., ESHEL, A., VOHR, J.H. & WEILDMANN, M., 1980, *Fluid Film Lubrication*, John Wiley & Sons, Inc..
- HATA, H.; NAKAHARA, T. & AOKI, H., 1980, "Measurement of friction in slightly loaded hydrodynamic sliders with striated roughness", In: *Surface Roughness Effects in Hydrodynamic and Mixed Lubrication*, ROHDE, S.M. & CHENG, H.S. (eds.), New York, pp. 75–92.
- HU, J.; LEUTHEUSSER, H.J. & ZHANG, Z., 1994, "Fluid film lubrication between rough surfaces", In: *Proc. of 4th International Tribology Conference*, (Austrib '94) STACHOWIAK, G.W. (ed.), Perth, Western Australia, pp. 637–639.
- HU, J. & LEUTHEUSSER, H.J., 1995, "Experiments on roughness effects in hydrodynamic lubrication", In: *Proc. of 15th Canadian Congress of Applied Mechanics*, TABARROK, B. & DOST, S. (eds.), Victoria, British Columbia, Canada, pp. 967–968.
- HU, J. & LEUTHEUSSER, H.J., 1997a, "Microinertial effects on hydrodynamic lubrication", *Zeitschrift für angewandte Mathematik und Mechanik(ZAMM)*, **77**, No. SI, pp. S129–S130.
- HU, J. & LEUTHEUSSER, H.J., 1997b, "Micro-inertia effects in laminar thin-film flow over a sinusoidal wall", *Trans. ASME, Journal of Tribology*, **119**, No.1, pp. 221–216.
- HU, Y. & ZHENG, L., 1989, "Some aspects of determining the flow factors", *Trans. ASME, Journal of Tribology*, **111**, pp. 525–531.

- INNES, G.E., 1989, *Laminar-to-Turbulent Transition in Tilting-Pad Bearings*, M.A. Sc. Thesis, University of Toronto.
- INNES, G.E. & LEUTHEUSSER, H.J., 1991, "An investigation into laminar-to-turbulent transition in tilting-pad bearings", *Trans. ASME, Journal of Tribology*, **113**, pp. 303-307.
- JENG, Y.R., 1990, "Experimental study of the effects of surface roughness on friction", *STLE Tribology Transactions*, **33**, pp. 403-410.
- LEBECK, A.O., 1991, *Principles and Design of Mechanical Face Seals*, John Wiley & Sons, Inc., New York.
- MERZKIRCH, WOLFGANG, 1987, *Flow Visualization*, Second Edition, Academic Press, Inc., Orlando, pp. 29-35.
- McCOOL, J.I., 1982, "Finite difference spectral moment estimation for profiles: the effect of sample spacing and quantisation errors", *Precision Engineering*, **4**, pp. 181-184.
- MULVANEY, D.J., NEWLAND, D.E., AND GILL, K.F., 1986, "A characterization of surface texture profiles", *Proc. Instn. Mech. Engrs.*, **200**, No. C3., pp. 167-178.
- MOALIC, H., FITZPATRICK, J.A. & TORRANCE, A.A., 1989, "A spectral approach to the analysis of rough surfaces", *Trans. ASME, Journal of Tribology*, **111**, pp. 359-363.
- NAYAK, P. RANGANATH, 1971, "Random process model of rough surfaces", *Trans. ASME, Journal of Lubrication Technology*, **93**, pp. 398-407.
- PATEL, V.C.; CHON, J. T. & YOON, J.Y., 1991, "Laminar flow over wavy walls", *Trans.*

- ASME, *Journal of Fluids Engineering*, **113**, pp. 574–578.
- PATIR, N. & CHENG, H.S., 1978, “An average flow model for determining effects of three-dimensional roughness of partial hydrodynamic lubrication”, *Trans. ASME, Journal of Lubrication Technology*, **100**, pp. 12–17.
- PEKLINKIK, J., 1967/68, “New developments in surface characterization and measurements by means of random process analysis”, *Proc Instn Mech Engrs*, **182**(Pt. 3K), pp. 108–126.
- PEYRET, R. & TAYLOR, T.D., 1983, *Computational Methods for Fluid Flow*, Springer-Verlag, New York Inc..
- PINKUS, O., 1987, “The Reynolds centennial: A brief history of the theory of hydrodynamic lubrication”, *Trans. ASME, Journal of Tribology*, **109**, pp. 2–15.
- REDDY, J.J. & GARTLING, D.K., 1994, *The Finite Element Methods in Heat Transfer and Fluid Dynamics*, CRC Press, Inc., Boca Raton, Florida.
- RALPH, M.E., 1987, “Steady flow structures and pressure drops in wavy-walled tubes”, *Trans. ASME, Journal of Fluids Engineering*, **109**, pp. 255–261.
- RUSS, G. & BEER, H., 1997a, “Heat tranfer and flow field in a pipe with sinusoidal wavy surface – I. Numerical investigation”, *Int. J. Heat Mass Transfer*, **40**, No. 5 pp. 1061–1070.
- RUSS, G. & BEER, H., 1997b, “Heat tranfer and flow field in a pipe with sinusoidal wavy surface – II. Experimental investigation”, *Int. J. Heat Mass Transfer*, **40**, No. 5

pp. 1071-1081.

SCHLICHTING, H., 1968, *Boundary-Layer Theory*, 6th edition, McGraw-Hill Book Company, New York.

SERBETCI, I. & TICHY, J. A., 1991, "Inertial effects in thin film flow with a corrugated boundary", *Trans. ASME, Journal of Applied Mechanics*, **58**, pp. 272-277.

SHERRINGTON, I. & SMITH, E.H., 1987, "Parameters for characterizing the surface topography of engineering components", *Proc. Instn. Mech. Engrs.*, **201**, pp. 297-306.

SHERRINGTON, I. & SMITH, E.H., 1988, "Fourier models of the surface topography of engineering components", *Surface Topography*, **1**, pp. 167-181.

SPRAGG, R.C. & WHITEHOUSE, D.J., 1970/71, "A new unified approach to surface metrology", *Proc. Instn. Mech. Engrs.*, **185**, pp. 697-707.

SZERI, A.Z., 1980, *Tribology : Friction, Lubrication, and Wear*, Hemisphere Publishing Corporation, Washington.

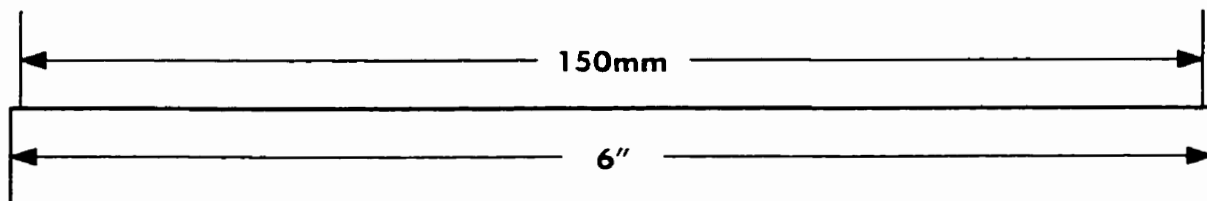
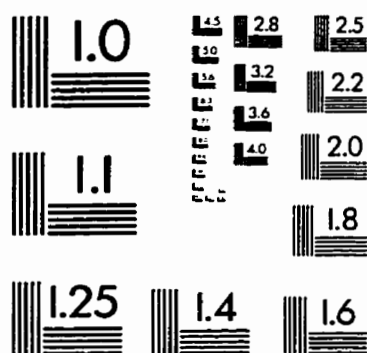
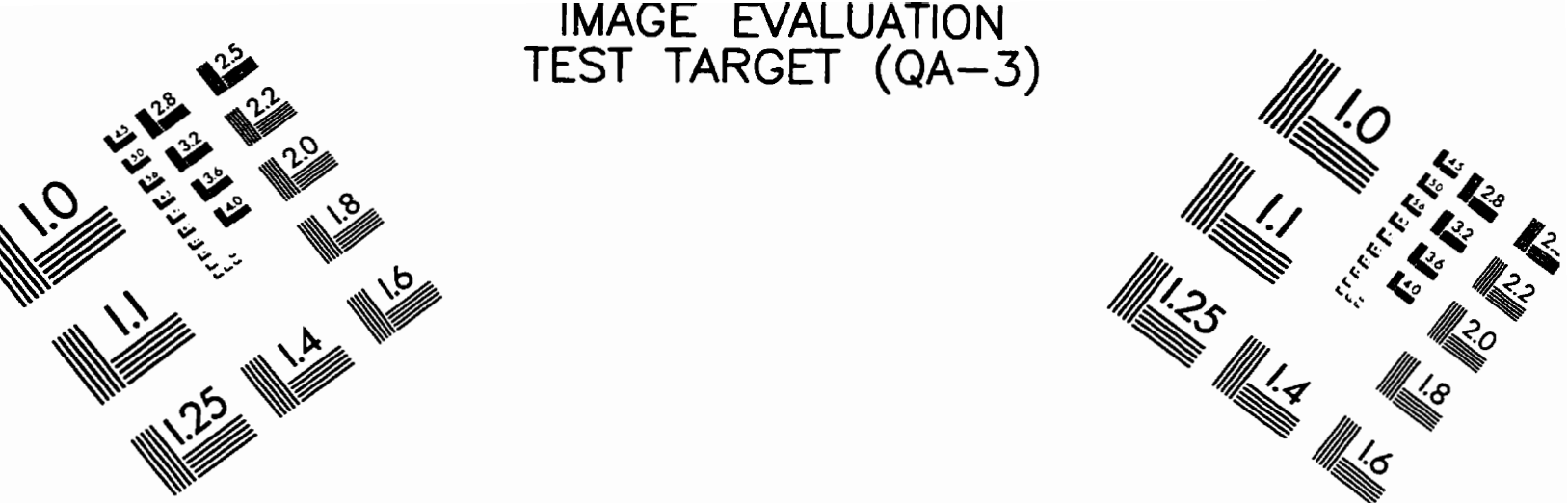
TEALE, J.L. & LEBECK, A.O., 1980, "An evaluation of the average flow model for surface roughness effects in lubrication", *Trans. ASME, Journal of Lubrication Technology*, **102**, pp. 360-367.

THOMAS, T.R. & KING, M., 1977, *Surface Topography in Engineering: A State of the Art Review and Bibliography*, BHRA Fluid Engineering, Cranfield, Bedford, England.

TØNDER, K., 1986, "The lubrication of unidirectional striated roughness: consequences for some general roughness theories", *Trans. ASME, Journal of Tribology*, **108**, pp. 167-

- 170.
- TØNDER, K., 1987, "Effects of skew unidirectional striated roughness on hydrodynamic lubrication, Part 2 - moving roughness", *Trans. ASME, Journal of Tribology*, **109**, pp. 671-678.
- TORII, K., 1979, "Flow visualization by smoke-wire technique", *Proc. of International Symposium on Flow Visualization*, ASANUMA, T. (ed.), Tokyo, pp. 251-256.
- TRIPP, J.H., 1983, "Surface roughness effects in hydrodynamic lubrication", *Trans. ASME, Journal of Lubrication Technology*, **105**, pp. 458-465.
- TSANIS, I.K., 1986, *Characteristics of shear-induced countercurrent flow*, Ph.D. Thesis, University of Toronto, Toronto, Canada.
- TSANIS, I.K. & LEUTHEUSSER, H.J., 1988, "The structure of turbulent shear-induced countercurrent flow", *Journal of Fluid Mechanics*, **189**, pp. 531-552.
- TZENG, S.T. & SAIBEL, E., 1967, "On the effects of surface roughness in the hydrodynamic lubrication theory of a short journal bearing", *Wear*, **10**, pp. 179-184.
- WHITE, J.W., RAAD, P.E., TABRIZI, A. H., KETKAR S. H. AND PRABHU, P. P., 1986, "A Numerical Study of Surface Roughness Effects on Ultra-thin Gas Films", *Trans. ASME, Journal of Tribology*, **108**, pp. 171-177.
- WHITEHOUSE, D.J., 1994, *Handbook of Surface Metrology*, Institute of Physics Publishing, Bristol and Philadelphia.
- WILLIAMS, J.A., 1994, *Engineering Tribology*, Oxford Science Publication, New York.

IMAGE EVALUATION TEST TARGET (QA-3)



APPLIED IMAGE, Inc.
1653 East Main Street
Rochester, NY 14609 USA
Phone: 716/482-0300
Fax: 716/288-5989

© 1993, Applied Image, Inc., All Rights Reserved

